196 Bull. Chem. Soc. Jpn. Vol. 79, No. 2, 196–227 (2006)

Award Accounts

The Chemical Society of Japan Award for Creative Work for 2003

Theoretical Investigations of the Electronic and Nuclear Dynamics of Molecules in Intense Laser Fields: Quantum Mechanical Wave Packet Approaches

Hirohiko Kono,* Yukio Sato, Manabu Kanno, Katsunori Nakai, and Tsuyoshi Kato

Department of Chemistry, Graduate School of Science, Tohoku University,
6-3 Aoba, Aramaki, Aoba-ku, Sendai 980-8578

Received July 15, 2005; E-mail: hirohiko-kono@mail.tains.tohoku.ac.jp

We have developed a method for describing the reaction dynamics of a polyatomic molecule in intense laser fields. First, the dynamical behavior of H_2^+ and H_2 in near-infrared, intense laser fields ($I > 10^{13}$ W cm^{-2} and $\lambda > 700$ nm) was examined; accurate evaluation of the electronic and nuclear wave packet was achieved by the dual transformation method that we developed. Using "field-following" time-dependent adiabatic states defined as eigenfunctions of the "instantaneous" electronic Hamiltonian, we have clarified the dynamics of bound electrons, ionization processes, Coulomb explosion processes, and molecular vibrations of H_2^+ and H_2. The analyses indicate that the multielectron dynamics and nuclear dynamics of *polyatomic* molecules in intense fields can be described by using the potential surfaces of time-dependent adiabatic states and the nonadiabatic coupling elements between those states. To obtain time-dependent adiabatic states of a molecule, one can diagonalize the electronic Hamiltonian including the interaction with the instantaneous laser electric field by ab initio molecular orbital (MO) methods. The time-dependent adiabatic potentials obtained are used to evaluate the multichannel nuclear dynamics until the next ionization process. We have applied the time-dependent adiabatic state approach to reveal the characteristic features of the dynamics of structural deformations of CO_2 and its cations in a near-infrared intense laser field. The experimentally observed stretched and bent structure of CO_2^{3+} just before Coulomb explosions originates from the structural deformation of CO_2^{2+}. We also revealed the mechanism of the experimentally observed bond dissociation of C_2H_5OH; we found that the relative probability of C–O bond cleavage to that of C–C bond cleavage becomes smaller with decreases in the pulse length. This example clearly shows that field-induced nonadiabatic transitions play a decisive role in the reaction dynamics of molecules in an intense laser field.

1. Introduction

The frontier of atomic and molecular studies on light-matter interaction has been expanded into new areas by the development of high-power lasers.[1–3] Nowadays, the intensity of focused light generated by Ti:Sapphire laser systems can easily exceed $I = 10^{16}$ W cm^{-2}. A laser field of light intensity of 3.5×10^{16} W cm^{-2}, which corresponds to 5.1×10^{9} V cm^{-1}, exerts on an electron a force that is as strong as the electron–nucleus interaction in a hydrogen atom. Novel phenomena induced by nonperturbative electronic dynamics in intense laser fields, such as tunnel ionization[4] and higher-order harmonic generation of emission (HHG),[5] have been discovered. An epoch is marked by the advent of attosecond light pulses generated by using HHG in a soft-X-ray regime.[6]

The introduction of handy high-powered laser systems into the field of chemistry is innovative but inevitable. Compared to atoms in intense fields, molecules exhibit complex phenomena arising from their additional (vibrational and rotational) degrees of freedom, such as charge-symmetric and -asymmetric dissociation,[7–9] alignment with an external field,[10] creation of electronically excited fragments,[11,12] and ionization rates that depend on the internuclear distance.[9,13,14] In intense laser fields ($I > 10^{13}$ W cm^{-2}), the Coulombic potentials in which the electrons are placed are greatly distorted:[15–18] A large part of the electron density is transferred among nuclei within a half optical cycle (≈1.3 fs for $\lambda = 800$ nm light).[19–21] Intramolecular electron transfer induced by such an intense field triggers structural deformation or nuclear motion of molecules. It should be emphasized that the interaction of an intense field with molecules is not restricted to resonant electronic or vibrational transitions. Near-infrared, intense-field pulses (centered around ≈800 nm) can induce chemical reactions[22,23] or structural deformations such as bond stretching and bond angle bending.[24]

The resultant structural deformations in turn change the electronic response to the field, e.g., the efficiency of intramolecular electron transfer and the probability of a tunnel type of ionization. As the field becomes stronger and its optical period ($=2\pi/\omega$, where ω is the frequency of light) becomes longer,

Published on the web February 10, 2006; DOI 10.1246/bcsj.79.196

the tunnel type of ionization[15–18,25] becomes dominant; an electron penetrates (or goes beyond) the distorted "quasi-static" barrier(s)[26] for ionization before the sign of the laser electric field changes. One characteristic of ionization of a molecule in an intense laser field is enhanced ionization; ionization is greatly enhanced at a critical internuclear distance, R_c, which is much longer than the equilibrium internuclear distance, R_e (known as enhanced ionization).[9,13,14,27–30] Enhanced ionization has been experimentally observed for various molecules,[27–30] such as CO_2[23] and benzene molecules.[31] The correlation between ionization and structural deformation plays a key role in fragmentation or reaction processes.[32–34] In other words, the competition between ionization and fragmentation governs the fate of the molecule in an intense field. One interesting example is C_{60}. It is known that C_{60} in a laser field decomposes into fragments, e.g., through the loss of C_2 units.[35,36] On the other hand, for the case of intense ultrashort 70 fs-laser pulses of near-infrared long wavelength $\lambda \approx 1600$ nm, a spectacular observation has been recently reported; highly charged C_{60} ions up to $C_{60}{}^{12+}$ are produced without any fragmentation.[37] This is just one example to indicate that the development of laser systems generating intense femtosecond pulses has made a new tool for manipulating the dynamics of molecules on an ultrashort time scale available to chemists.

In fact, a more sophisticated way of controlling reaction dynamics by using intense laser pulses had already been widely used. Gerber et al. used near-infrared, intense femtosecond laser pulses tailored by a genetic algorithm-controlled pulse shaper to optimize the branching ratios of different organometallic photodissociation channels.[22] Levis et al. reported selective bond dissociation and rearrangement of polyatomic molecules, such as acetophenone, by optically tailored, intense-field pulses ($\approx 10^{14}$ W cm^{-2}).[23] Many excited states that are dynamically Stark-shifted by such intense pulses can open various channels for reactions, and reaction selectivity is achieved by optimizing the phases and amplitudes of the optical component frequencies with a liquid crystal light modulator in the pulse shaper. However, it is a very difficult task to experimentally determine in which stage the structural deformations or chemical reactions occur, e.g., while the molecule is neutral or while it is a monocation. Furthermore, to enhance reaction selectivity, one must elucidate the mechanisms and characteristic features of molecular (electronic and nuclear) dynamics in intense fields. To the best of our knowledge, there were no practicable, systematic theoretical treatments to explain nuclear (reaction) dynamics of *polyatomic* molecules in intense laser fields.

Our research on the dynamical behavior of molecules in intense fields started from an investigation of the dynamics of a very basic example, namely, $H_2{}^+$. To quantitatively understand the ultrafast electronic dynamics in intense fields, one must solve the time-dependent Schrödinger equation for the electronic degrees of freedom of a molecule. We developed an efficient grid point method, the dual transformation method,[38] for accurate propagation of an electronic wave packet. In this method, both the wave function and the Hamiltonian are transformed consistently to overcome the numerical difficulties arising from the divergence of the Coulomb potentials involved. We have applied this method to $H_2{}^+$[19] and H_2.[20,39] The vibrational degree of freedom is incorporated in the calculation of $H_2{}^+$ without resorting to the Born–Oppenheimer (B–O) approximation.[19] The calculated whole dynamics of the electronic and nuclear degrees of freedom is analyzed by using "field-following" time-dependent adiabatic electronic states $\{|n\rangle\}$ defined as eigenfunctions of the "instantaneous" electronic Hamiltonian $H_{el}(t)$ including the interaction with a laser electric field $\mathcal{E}(t)$.[19,39–45] Only field-free adiabatic states, i.e., bound state components, are used to diagonalize $H_{el}(t)$. In a high-intensity regime, "field-following" time-dependent eigenvalues interpreted as time-dependent adiabatic potential surfaces can cross each other in energy so that nonadiabatic transitions between adiabatic states occur.[19,39–45] We have demonstrated how "doorway states" to ionization or to structural deformation of $H_2{}^+$ and H_2 can be identified by population analysis of time-dependent adiabatic states. The analysis has shown that the nuclear dynamics in a near-infrared field can be described in terms of wave packet propagation on time-dependent adiabatic potentials and nonadiabatic transitions due to temporal changes in $\mathcal{E}(t)$. It also turns out that tunnel ionization to Volkov states[18,46] (quantum states of a free electron in a laser field) proceeds substantially in an adiabatic state or adiabatic states.

The above description of dynamics in terms of time-dependent adiabatic states constructed from bound electronic states, i.e., the time-dependent adiabatic state approach, is applicable to *polyatomic* molecules in intense laser fields. While the intramolecular *multielectron* dynamics of a polyatomic molecule in intense laser fields can be described by time-dependent adiabatic electronic states, the resultant nuclear dynamics is described by multichannel wave packet propagation on time-dependent adiabatic potentials. The charge distributions on individual atomic sites of doorway states to ionization can be used to judge whether ionization occurs or not at a given intensity. This approach has an advantage that the properties of the adiabatic states of polyatomic molecules can be evaluated by ab initio molecular orbital (MO) methods intended to calculate bound electronic states.[47,48]

The structure of this paper is as follows. Section **2** is used to explain basic concepts such as tunnel ionization. In Section **3** and Section **4**, we review the results of our theoretical investigations of electronic and nuclear dynamics of $H_2{}^+$ and H_2 in near-infrared intense fields. Population analysis in terms of time-dependent adiabatic states is presented. We next outline the proposed time-dependent adiabatic state approach (Section **5**) and review the results of its application to CO_2 (Section **6**). Reliable experimental data of structural deformation of CO_2 in a near-infrared, intense laser field is now available.[24] From the results of calculation of the nuclear wave packet dynamics of CO_2 and its cations, we have extracted the characteristic features of the dynamics of CO_2 in intense fields that are responsible for the observed structural deformation. In Section **7**, we present the results for field-induced dissociation of ethanol that we theoretically investigated on the basis of the time-dependent adiabatic state approach. The dissociative ionization of ethanol has been experimentally investigated by Itakura et al.[49] We discuss the mechanisms of preferential dissociation of the C–C and C–O bonds of ethanol in intense laser fields to assess the importance of field-induced avoided crossings in reaction dynamics. Concluding remarks are given in Section **8** with a summary of the present study.

2. Multiphoton Ionization and Tunnel Ionization

"Tunnel ionization" is a ubiquitous term in the research field of phenomena induced by intense laser light. It is used to describe nonperturbative ionization processes that are different from multiphoton ionization (MPI)[50] in a nonlinear but perturbative regime. In this section, we outline the differences between MPI and tunnel ionization, although it is difficult to draw perfect distinction between the two types of ionization. At intensities lower than 10^{12} W cm^{-2}, the ionization process is interpreted as "normal" MPI; the minimum number of photons necessary for exceeding the ionization threshold are absorbed. As the laser intensity approaches 10^{13} W cm^{-2}, "normal" MPI is taken over by above-threshold ionization (ATI),[51–54] where more photons than the minimum number of photons required to escape the binding potential are absorbed. As a result, in photoelectron energy spectra, discrete peaks appear at intervals of one photon energy. At intensities lower than 10^{13} W cm^{-2}, the ATI peaks can be assigned to higher order terms in a perturbation expansion of light-matter interaction; in this domain, ATI is interpreted as a multiphoton processes.

Laser fields of the higher intensities ($I > 10^{13}$ W cm^{-2}) induce nonperturbative phenomena. Such a laser electric field significantly distorts the Coulombic potential that the electrons are placed in; the distorted potential forms a "quasi-static" barrier (or barriers) through which an electron or electrons can tunnel.[15–18] Tunnel ionization occurs if the electron has enough time to penetrate the barrier(s) before the sign of the field changes. The tunnel ionization regime can be distinguished by using the Keldysh parameter $\gamma = \omega\sqrt{2I_\mathrm{p}}/f(t)$,[15] where I_P is the ionization potential of the system, ω is the laser frequency, and $f(t)$ is the pulse envelope at time t. An interpretation of Keldysh parameter is as follows.[55] The length of the barrier in a distorted Coulombic potential is estimated as $I_\mathrm{p}/f(t)$ (for a zero-range potential), and the average velocity of the tunneling electron is $\sqrt{2I_\mathrm{p}}/2$. The time required to escape the binding potential through tunneling is then $\tau_\mathrm{tun} = \sqrt{2I_\mathrm{p}}/f(t)$. The Keldysh parameter is the ratio of τ_tun to the optical period $1/\omega$.

Favorable to tunnel ionization are the conditions that the electric field is stronger and that its period is longer. The quasi-static tunneling condition is given by the inequality $\gamma < 1$. In the high-intensity and low-frequency regime (intensity $I > 10^{13}$ W cm^{-2} and wavelength $\lambda > 700$ nm), the rate of ionization can be estimated by "quasi-static" tunnel theories.[15–18,56] Among various versions of tunnel theory applicable to the adiabatic limit of $\gamma \ll 1$, the Ammosov–Delone–Krainov (ADK) theory[17] has been most widely used. In the tunneling regime, the ionization probability depends on frequency only weakly. When the electron ejected through tunneling circles back to the vicinity of the nucleus (rescattering), higher-order harmonics (HHG)[5] are generated. Corkum[26] has well explained the mechanism of HHG by assuming that the velocity of the electron just after quasi-static tunneling is zero and the evolution of the ejected electron is described by quiver motion in classical mechanics or equivalently Volkov states in quantum mechanics. HHG is a rich information source about the highest occupied molecular orbital (HOMO) from which a single-active electron is ejected.[57] For example, Corkum et al.[57b] have demonstrated that the full three-dimensional structure of a single orbital can be imaged by a seemingly unlikely technique, using high harmonics generated from intense femtosecond laser pulses focused on aligned molecules. Applying this approach to a temporal sequence of molecular alignments caused by a nonadiabatic interaction with a short pulse, they constructed a tomographic view of the HOMO of N_2.

The domain for MPI is given by the opposite case of $\gamma > 1$. The probability of "normal" MPI or ATI is very sensitive to the existence of real intermediate states in resonance with the photon energy. Resonance structures also appear in ATI spectra.[53] For a short pulse of which the width is less than 1 ps (but not as short as a few-cycle pulse), an individual ATI peak break up into narrow fine structures apparently due to resonance with intermediate Stark-shifted Rydberg states (which can be roughly estimated by the ponderomotive shift induced by the quiver motion of an electron in an intense laser field).[58] For longer pulses, the fine structures disappear because all the electrons leave the interaction volume with *some* extra ponderomotive energy before the applied field is turned off.[59] In the tunneling regime, an electron is ejected from the remaining ion core essentially within a half optical cycle. All structures associated with resonances are washed out. Resonances with intermediate states are less important. As the response of the system to the field is approaching the tunneling regime, ATI peaks broaden and eventually overlap with each other.[60]

In the case of molecules, in addition to electronic motion, nuclear motion must be considered. In the MPI regime ($\gamma > 1$) up to 10^{10} W cm^{-2}, as the intensity becomes higher and the pulse duration becomes longer, the ionization process changes from soft ionization (where only parent ions appear) to hard fragmentation (small fragments are produced).[50,61–63] The ladder switching from photon absorption by the neutral to that by the parent ion takes place.[61,62] The second ladder switching from the parent ion to fragment ions is typical for most polyatomic molecules. When dissociation in an intermediate state is faster than photon absorption, the absorption ladder switches to a fragment. Fragment patterns can be described by statistical models where redistribution of energy among all degrees of freedom is assumed.[64] All of ions are produced with very *little* excess energy as a consequence of the ladder-switching mechanism for MPI and dissociation. As a result, fragments have small kinetic energies of $\approx$0.2 eV.

In the intense field regime for which $\gamma < 1$ is satisfied, ionization occurs faster than dissociation. As shown in Sections **3** and **4**, the dependence of the calculated ionization probabilities of $H_2{}^+$ or H_2 on the internuclear distance is in accordance with the experimentally observed tendency of enhanced ionization: That ionization of a molecule in a near-infrared laser field is greatly enhanced at critical internuclear distances which are much larger than the equilibrium internuclear distance. Although the ionization potential of $H_2{}^+$ simply decreases as the internuclear distance increases, the ionization rate has a peak or peaks at intermediate internuclear distances. The analysis of the entire electronic wave packet indicates that acceleration or suppression of field-induced intramolecular electron transfer leads to enhanced ionization. Enhanced ionization is a universal phenomenon irrespective of whether the molecule is diatomic or polyatomic. For multielectron molecules, enhanced ionization creates multiply charged molecular ions, which immediately undergo Coulomb explosions due to nuclear repulsion.[65] It is shown that field-induced intramolecular electronic dynamics also causes chemical reactions (fragmentations)[48,66] other than Coulomb explosions. Intramolecular electronic dynamics, which triggers both enhanced ionization and reaction dynamics, is therefore regarded as the key process to control the competition between the ionization and the reaction of molecules.

3. Electronic and Nuclear Dynamics of H_2^+ in Intense Laser Fields

In this section, we show how the electronic and nuclear wave packet of H_2^+ in an intense laser field evolves temporally and spatially and we present the results of time-dependent adiabatic state analysis of the wave packet dynamics of H_2^+. We introduce the important concept of "doorway state to tunnel ionization" by using a time-dependent adiabatic state basis set.

3.1 Numerical Solution of the Time-Dependent Schrödinger Equation for a 3D H_2^+ Hamiltonian: The Dual Transformation Technique. We first derive a three-dimensional (3D) Hamiltonian for the electronic and nuclear degrees of freedom of H_2^+ in a laser electric field. In the present treatment, molecular vibration is allowed, but the molecular axis is assumed to be fixed to a direction in space. In addition to the internuclear distance R, we must in general consider three electronic coordinates; e.g., three cylindrical coordinates z, ρ, and φ ($x = \rho\cos\varphi, y = \rho\sin\varphi, z = z$), where ρ is the coordinate perpendicular to z. In intense laser fields, electrons move with a large amplitude oscillation in the case where the molecular axis is parallel to the polarization direction of the laser electric field $\mathcal{E}(t)$; on the other hand, at the perpendicular configuration of the molecular axis and the field, the distortion of the electron cloud is relatively small. This is related to the anisotropy of polarization: The axis component of the polarizability of a diatomic molecule is larger than the perpendicular component at intermediate internuclear distances.[67,68] As a result, the rate of tunnel ionization has a maximum near the geometry where the molecular axis is parallel to the polarization direction,[69–71] i.e., where the angle between the molecular axis and the polarization direction, θ_{ML}, is 0° (although it has been experimentally shown that the ionization rate of O_2 in an intense near-infrared field has a maximum around $\theta_{\mathrm{ML}} \approx 45°$.[72] See, for related theoretical work, Refs. 73–76). Besides, it is known that a diatomic molecule of anisotropic polarization is aligned by a laser electric field so that the molecular axis is parallel to the polarization direction.[10] This parallel case should be studied as the main spatial configuration. Then, the molecular axis component of the electronic angular momentum, $\hbar m$, is conserved (the magnetic quantum number m is conserved). In this case, it is convenient to set the coordinate z parallel to the molecular axis; after separation of the center-of-mass of a molecule, the total wave function can be written as a product form of $\Phi(z,\rho,R)e^{im\varphi}/\sqrt{2\pi}$. The wave function $\Phi(z,\rho,R)$ is normalized as

$$\int_0^{\infty} \mathrm{d}R \int_0^{\infty} \mathrm{d}\rho \int_{-\infty}^{\infty} \mathrm{d}z \rho |\Phi(z,\rho,R)|^2 = 1. \tag{1}$$

Choosing the midpoint between the two protons as the origin of the electronic coordinates, we then reduce the time-dependent Schrödinger equation for the four degrees of freedom (z, ρ, R, and φ) to that for $\Phi(z,\rho,R)$ as (throughout this paper atomic units are used unless otherwise noted, i.e., $m_{\mathrm{e}} = a_0 = e = E_{\mathrm{h}} = \hbar = 1$, where m_{e}, a_0, e, and E_{h} are the electron mass, Bohr radius, elementary electric charge, and hartree, respectively)

$$\iota \frac{\partial}{\partial t}\Phi(z,\rho,R) = \left[-\frac{1}{m_{\mathrm{p}}}\frac{\partial^2}{\partial R^2} + H_{\mathrm{el}}(t)\right]\Phi(z,\rho,R), \tag{2}$$

where m_{p} is the proton mass and the instantaneous electronic Hamiltonian $H_{\mathrm{el}}(t)$ is the sum of the Born–Oppenheimer (B–O) electronic Hamiltonian at zero field strength, H_{el}^0, and the dipole interaction with light, $V_{\mathcal{E}}(z,t)$:

$$H_{\mathrm{el}}(t) = H_{\mathrm{el}}^0 + V_{\mathcal{E}}(z,t). \tag{3}$$

The explicit form of $H_{\mathrm{el}}(t)$ is given by[77]

$$H_{\mathrm{el}}^0 = -\frac{1}{2\mu_{\mathrm{e}}}\left(\frac{\partial^2}{\partial\rho^2} + \frac{1}{\rho}\frac{\partial}{\partial\rho} + \frac{\partial^2}{\partial z^2}\right) + \frac{m^2}{2\rho^2} + V(z,\rho,R) + \frac{1}{R}, \tag{4}$$

where $\mu_{\mathrm{e}} = 2m_{\mathrm{p}}m_{\mathrm{e}}/(2m_{\mathrm{p}} + m_{\mathrm{e}}) \approx m_{\mathrm{e}}$ and $V(z,\rho,R)$ is the Coulomb attractive potential exerted on the electron

$$V(z,\rho,R) = -\frac{1}{\sqrt{\rho^2 + (z - R/2)^2}} - \frac{1}{\sqrt{\rho^2 + (z + R/2)^2}}. \tag{5}$$

The nuclear repulsion energy $1/R$ is included in Eq. 4. The dipole interaction between the molecule and the electric field $\mathcal{E}(t)$ is expressed as

$$V_{\mathcal{E}}(z,t) = [1 + m_{\mathrm{e}}/(2m_{\mathrm{p}} + m_{\mathrm{e}})]z\mathcal{E}(t) \approx z\mathcal{E}(t). \tag{6}$$

Equation 2, which contains both electronic and vibrational degrees of freedom, can be solved "exactly" by an efficient grid method for accurate propagation of an electronic wave packet of a Coulombic system[19,38a] without resorting to the Born–Oppenheimer approximation. In this method, called "dual transformation," the following three requirements are introduced to treat the attractive Coulomb potential which is characterized by its long range and its singularity at the nucleus. The first one is as follows: (i) The wave function is transformed so that it is zero at the Coulomb singular points (which ensures that the numerical difficulties concerning singularity are avoided). The choice of new scaled coordinates is also crucial: (ii) Near the nuclei, the equally spaced intervals in the new (scaled) coordinates must generate small grid intervals in the linear scaled (cylindrical) coordinates (to cope with the extremely high momentum components near the nuclei); in the weak interaction region where the distance from the nuclei is larger, the corresponding intervals in the linear scaled (cylindrical) coordinates are chosen to be relatively large and nearly constant. With the help of finite difference formulas, we then spatially discretize the transformed Schrödinger equation which the transformed wave function obeys. To that end, the transformed wave function must be analytic around the nuclei:

(iii) The differential operators contained in the transformed Hamiltonian can be evaluated well by the finite difference method even near the Coulomb singular points.

We have applied the method to H_2^+ (including molecular vibration)[19] and H_2,[29,39] where the unscaled cylindrical coordinate ρ is transformed to $\rho = g_1(\xi)$ so that the function g_1 is chosen to satisfy the three requirements (i)–(iii) given above. In the case of an unscaled cylindrical coordinate system (i.e., for $\rho = \xi$), the finite difference method does not provide sufficient accuracy for evaluating the differential operators contained in the Hamiltonian. Scaling can be extended to the unscaled z coordinate as $z = g_2(\zeta)$.

In addition to the variable transformation in the total Hamiltonian $-(1/m_\mathrm{p})(\partial^2/\partial R^2) + H_\mathrm{el}(t)$, we have to transform the wave function to avoid the numerical difficulties concerning Coulomb singularities. The original wave function $\Phi(z, \rho, R)$ which is in general finite at the nuclei must be transformed to a function $\Phi^\mathrm{DT}(\zeta, \xi, R)$ that is zero at the nuclei. This demand on the transformed wave function, i.e., requirement (i), must be satisfied under a normalization condition for the transformed wave function $\Phi^\mathrm{DT}(\zeta, \xi, R)$. In the case where finite difference formulas are employed, it can be difficult to conserve the norm of the wave function. For instance, the finite difference representation of $(1/\rho)\partial/\partial\rho$ in Eq. 4 is asymmetric, i.e., it is no longer Hermitian. In order to make a time evolution scheme based on the finite difference method stable and accurate, one should impose the following normalization condition on $\Phi^\mathrm{DT}(\zeta, \xi, R)$ used in the actual numerical calculation[38]

$$\int_0^\infty \mathrm{d}R \int_0^\infty \mathrm{d}\xi \int_{-\infty}^\infty \mathrm{d}\zeta |\Phi^\mathrm{DT}(\zeta, \xi, R)|^2 = 1. \tag{7}$$

Note that the Jacobian or the scale factor for each coordinate is formally unity, unlike in the normalization condition for $\Phi(z, \rho, R)$.

The transformed wave function that satisfies the normalization condition, Eq. 7, is uniquely determined as

$$\Phi^\mathrm{DT}(\zeta, \xi, R) = \sqrt{g_1(\xi) g_1'(\xi) g_2'(\zeta)}\, \Phi(z, \rho, R), \tag{8}$$

where a prime denotes the derivative with respect to the argument of the function. Inserting Eq. 8 into Eq. 2, we obtain the following transformed Schrödinger equation

$$\imath \frac{\partial}{\partial t} \Phi^\mathrm{DT}(\zeta, \xi, R) = \left[-\frac{1}{m_\mathrm{p}} \frac{\partial^2}{\partial R^2} + H_\mathrm{el}^\mathrm{DT}(t) \right] \Phi^\mathrm{DT}(\zeta, \xi, R), \tag{9}$$

where the transformed Hamiltonian $H_\mathrm{el}^\mathrm{DT}(t)$ is expressed as

$$H_\mathrm{el}^\mathrm{DT}(t) = \sqrt{g_1(\xi) g_1'(\xi) g_2'(\zeta)}\, H_\mathrm{el}(t) \frac{1}{\sqrt{g_1(\xi) g_1'(\xi) g_2'(\zeta)}}. \tag{10}$$

The explicit form of Eq. 10 is given in Ref. 38a, together with g_1 and g_2 functions of scaled coordinates ξ and ζ that fulfill the three requirements (i)–(iii). The introduction of these transformations drastically reduces the required numbers of grid points.[38] Equation 9 is integrated in time by a 3D version of the alternating-direction implicit method (ADI) called the D'yakonov scheme.[78] The ADI provides short time propagators of which the quality is characterized by the second-order accuracy of a short time step Δt and by the numerical stability for various potentials.

3.2 Field-Following Adiabatic States and Field-Induced Nonadiabatic Coupling. We show in the next subsection that the intramolecular electronic motion in H_2^+ which triggers tunnel ionization and nuclear motion can be understood in terms of field-following time-dependent adiabatic states. We have fully analyzed the H_2^+ dynamics for the first time by using time-dependent adiabatic states. The time-dependent adiabatic states defined here are obtained by diagonalizing the instantaneous electronic Hamiltonian $H_\mathrm{el}(t)$ in terms of bound states of H_el^0: $|\psi_1\rangle, |\psi_2\rangle, \ldots, |\psi_n\rangle$. The matrix elements of $H_\mathrm{el}(t)$ are functions of adiabatic parameters R and t. Diagonalization of $H_\mathrm{el}(t)$ yields the time-dependent adiabatic states $\{|j(t)\rangle\}$ and energies $\{E_j(t)\}$, where j runs from 1 to n in ascending order with respect to energy. To diagonalize $H_\mathrm{el}(t)$, we here use the lowest two bound electronic states $1\mathrm{s}\sigma_g$ and $1\mathrm{s}\sigma_u$ for $H_\mathrm{el}^0(t)$ (abbreviated as $|g\rangle$ and $|u\rangle$, respectively), which are radiatively coupled with each other by the transition dipole moment $\langle g|z|u\rangle \simeq R/2$. This large transition moment is characteristic of a charge resonance transition between a bonding and a corresponding antibonding molecular orbital, which was originally pointed out by Mulliken.[79] The eigenvalues of H_el^0 for $1\mathrm{s}\sigma_g$ and $1\mathrm{s}\sigma_u$ are denoted by $E_g(R)$ and $E_u(R)$, respectively.

In this two-state model, the time-dependent eigenfunctions, $|1\rangle$ and $|2\rangle$, which are adiabatically connected with $1\mathrm{s}\sigma_g$ and $1\mathrm{s}\sigma_u$ at $\mathcal{E}(t) = 0$, are given analytically as[19,80]

$$|1\rangle = \cos\Theta|g\rangle - \sin\Theta|u\rangle, \tag{11a}$$

$$|2\rangle = \cos\Theta|u\rangle + \sin\Theta|g\rangle, \tag{11b}$$

where Θ is a function of t and R:

$$\Theta = \frac{1}{2} \arctan\left[\frac{2\langle g|z|u\rangle \mathcal{E}(t)}{\Delta E_{ug}(R)}\right], \tag{12}$$

with the B–O energy separation $\Delta E_{ug}(R) = E_u(R) - E_g(R)$. The corresponding eigenvalues (potential surfaces) are

$$\begin{aligned} E_{2,1}(R,t) &= \frac{1}{2}\left[E_g(R) + E_u(R) \pm \sqrt{\Delta E_{ug}^2 + 4|\langle g|z|u\rangle \mathcal{E}(t)|^2}\right] \\ &\simeq \frac{1}{2}[E_g(R) + E_u(R) \pm R|\mathcal{E}(t)|] \quad \text{for large } R. \end{aligned} \tag{13}$$

The adiabatic energies $E_{1,2}(R,t)$ at $\mathcal{E}(t) = 0.053 E_\mathrm{h}/ea_0$ are shown in Fig. 1 along with E_g and E_u. If $\mathcal{E}_a(t)$ is a value of the field strength in atomic units (i.e., in units of E_h/ea_0), the corresponding field strength in SI units, $\mathcal{E}(t)$, is given by the relation $\mathcal{E}(t) = 5.14 \times 10^{11} \mathcal{E}_a(t)\,\mathrm{V\,m^{-1}}$. The light intensity I in SI units is given by $I = 3.5 \times 10^{16} \mathcal{E}_a(t)^2\,\mathrm{W\,cm^{-2}}$, where the value of $\mathcal{E}(t)$ is assumed to be equal to the field envelope (field amplitude).

The instantaneous electrostatic potential for the electron, $V(z, \rho, R) + V_\mathcal{E}(z, t)$, has two wells around the nuclei, i.e., $z = \pm R/2$. The dipole interaction energy for an electron is $\mathcal{E}(t)R/2$ at the right nucleus and $-\mathcal{E}(t)R/2$ at the left nucleus. As $\mathcal{E}(t)$ increases from zero to a positive value, the potential well formed around the right nucleus ascends and the well formed around the left nucleus descends, and vice versa when $\mathcal{E}(t) < 0$. Therefore, at large $R|\mathcal{E}(t)|$, E_2 and E_1 change according to the energy shifts of the ascending and descending wells, respectively; the electron densities of $|2\rangle$ and $|1\rangle$ are localized near the ascending and descending wells, respectively (irrespective of the sign of the electric field).

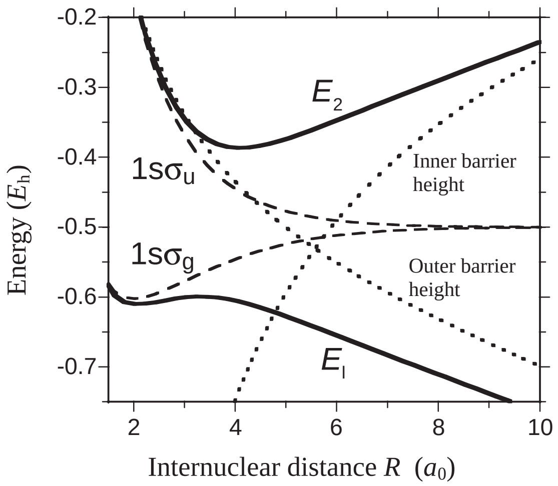

Fig. 1. Potential energies $E_1(R,t)$ and $E_2(R,t)$ of the lowest two field-following adiabatic states $|1\rangle$ and $|2\rangle$ of $H_2{}^+$ (denoted by solid lines) at $\mathcal{E}(t) = 0.053E_h/ea_0$, i.e., at $I = 10^{14}\,\mathrm{W\,cm^{-2}}$ as a function of internuclear distance R. The broken lines denote the Born–Oppenheimer potential surfaces of $1s\sigma_g$ and $1s\sigma_u$. The dotted lines denote the heights of the inner and outer barriers for tunnel ionization. The internuclear repulsion $1/R$ is included in the energy.

To investigate the nuclear dynamics and ionization dynamics of $H_2{}^+$, we project the "exact" electronic and nuclear wave packet $\Phi(z,\rho,R;t)$ onto $|1\rangle$ and $|2\rangle$. The two projected components $\chi_1(R,t) = \langle 1|\Phi(t)\rangle$ and $\chi_2(R,t) = \langle 2|\Phi(t)\rangle$ (integrated over ρ and z) are used for analyses of the mechanism of ionization and the field-induced nuclear dynamics. We also use this expansion formula for the total wave function $|\Phi\rangle$:

$$|\Psi(z,\rho,R;t)\rangle = \chi_1'(R,t)|1\rangle + \chi_2'(R,t)|2\rangle, \tag{14}$$

where $|\Psi\rangle$ is an approximate wave function for $|\Phi\rangle$. It will be shown that the key processes of intramolecular electronic motion and nuclear motion can be described by this expansion while ionization is not directly taken into account. The following approach using the two time-dependent adiabatic states can be straightforwardly extended to cases where the number of time-dependent adiabatic states are more than two. The results for a six-state model are summarized in Section **3.3**.

Inserting Eq. 14 into Eq. 2, we derive the coupled equations within the framework of the two-state model as[19,43,45]

$$\frac{\partial}{\partial t}\chi_1'(R) = -i\left[-\frac{1}{m_p}\frac{\partial^2}{\partial R^2} + E_1(R,t) + \frac{1}{m_p}\left(\frac{\partial\Theta}{\partial R}\right)^2\right] \times \chi_1'(R) - \Lambda(R,t)\chi_2'(R), \tag{15a}$$

$$\frac{\partial}{\partial t}\chi_2'(R) = -i\left[-\frac{1}{m_p}\frac{\partial^2}{\partial R^2} + E_2(R,t) + \frac{1}{m_p}\left(\frac{\partial\Theta}{\partial R}\right)^2\right] \times \chi_2'(R) + \Lambda(R,t)\chi_1'(R), \tag{15b}$$

where the total coupling $\Lambda(R,t)$ that induces nonadiabatic transitions between the two-time-dependent adiabatic states is

$$\Lambda(R,t) = \left\langle 1\left|\frac{\partial}{\partial t}\right|2\right\rangle - \frac{2i}{m_p}\frac{\partial\Theta}{\partial R}\frac{\partial}{\partial R} - \frac{i}{m_p}\frac{\partial^2\Theta}{\partial R^2} + \dots. \tag{16}$$

Here, the small terms $\langle g|\partial^2/\partial R^2|g\rangle/m_p$ and $\langle u|\partial^2/\partial R^2|u\rangle/m_p$ are not explicitly written in the diagonal elements in Eq. 15 and the off-diagonal element Eq. 16. The term $\langle 1|\partial/\partial t|2\rangle = \partial\Theta/\partial t$ is the nonadiabatic coupling due to temporal change in the electric field $\mathcal{E}(t)$[80] and the other coupling terms in Eq. 16 are due to the joint effect of the electric field and the nuclear motion.

Thachuk et al. have developed a semiclassical formalism for treating time-dependent Hamiltonians and applied it to the dissociation of diatomic ions.[80] The internuclear distance R is treated parametrically as some time-dependent function describing the motion of the nuclei. They have derived the nonadiabatic couplings $\partial\Theta/\partial t$ and $v\partial\Theta/\partial R$ for the two-state model from the semiclassical formalism, where v is the relative nuclear velocity. These two terms correspond to the first and second terms in Eq. 16. When typical values of the nuclear velocities are assumed, the effect of $\partial\Theta/\partial t$ is much larger than that of $v\partial\Theta/\partial R$ for homonuclear diatomic ions (in a near-infrared field). In the case of heteronuclear diatomic ions, the dominant coupling term which causes hopping between time-dependent surfaces is also $\partial\Theta/\partial t$. The term $v\partial\Theta/\partial R$ causes significant hopping at small internuclear distances only when the field-induced Stark shift is, in the domain of small R, comparable to the energy gap between the field-free states.

It is expected from Eqs. 15 and 16 that field-induced nonadiabatic transitions occur if the main coupling term $\partial\Theta/\partial t$ is large in comparison with the gap between the two adiabatic potential surfaces, $E_2 - E_1$. The term $\partial\Theta/\partial t$ is expressed as

$$\partial\Theta/\partial t = \frac{\langle g|z|u\rangle}{\Delta E_{ug}(R)}\frac{\partial\mathcal{E}(t)}{\partial t}(\cos 2\Theta)^2. \tag{17}$$

Since $\mathcal{E}(t)$ is a sinusoidal function of time, $|\partial\mathcal{E}(t)/\partial t|$ and $(\cos 2\Theta)^2$ becomes largest when $\mathcal{E}(t) = 0$, i.e., $t_n = n\pi/\omega$ (n is an integer) for

$$\mathcal{E}(t) = f(t)\sin(\omega t), \tag{18}$$

where ω is the light frequency and $f(t)$ is the envelope of the pulse shape (field amplitude). The gap $E_2 - E_1$ becomes ΔE_{ug}, i.e., smallest when the two adiabatic potential surfaces come closest to each other, i.e., again, when the field $\mathcal{E}(t)$ changes its sign. Thus, a nonadiabatic transition between the two adiabatic states is expected to occur within a very short period τ_{tr} before and after the field $\mathcal{E}(t)$ changes its sign.[45,81] It should be noted that $\langle g|z|u\rangle/\Delta E_{ug}(R)$ increases as R increases [$\langle g|z|u\rangle$ is an increasing function of R and $\Delta E_{ug}(R)$ is a decreasing function of R]. Larger internuclear distances are thus favorable for nonadiabatic transition. A nonadiabatic transition between $|1\rangle$ and $|2\rangle$ corresponds to suppression of electron transfer between the two wells, i.e., two nuclei.

If the nuclear motion is slow in comparison with the time scale of τ_{tr}, the nonadiabatic transition probability *per level crossing* at R, P_{nonad}, can be defined; it is given by the Landau–Zener form[82]

$$P_{\mathrm{nonad}} = \exp(-2\pi\delta), \tag{19}$$

where

$$\delta = \Delta E_{ug}(R)^2/8\langle g|z|u\rangle f(t)\omega. \tag{20}$$

For $\delta \gg 1$, the electronic state remains in the same adiabatic state such as $|1\rangle$ or $|2\rangle$. For $\delta \ll 1$, the main route is the non-

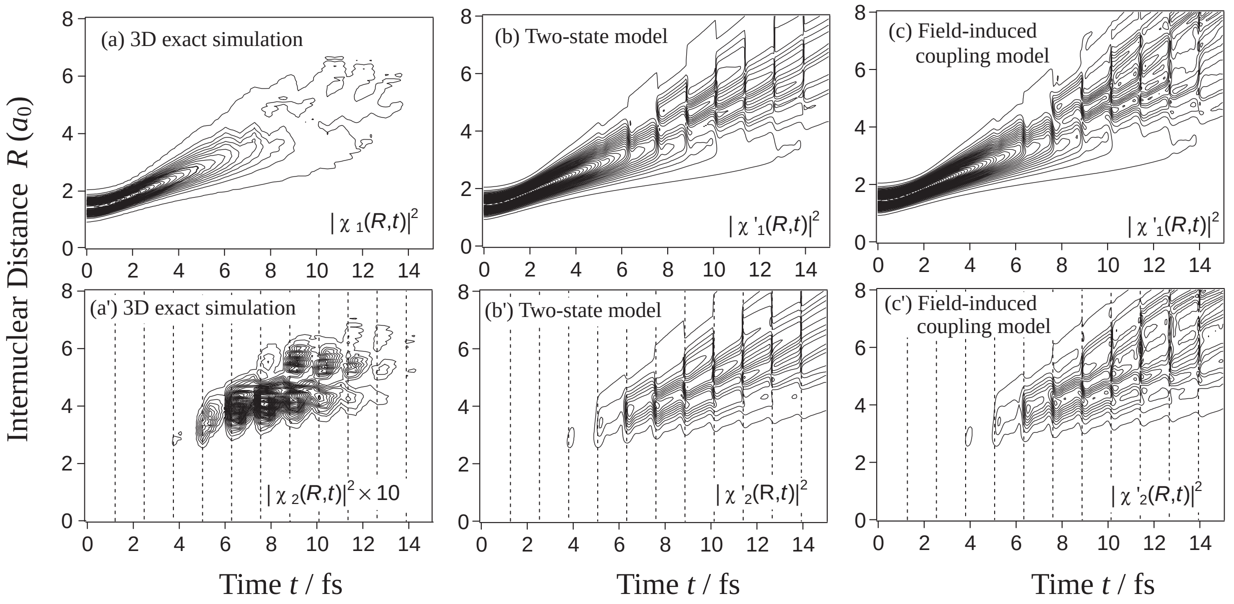

Fig. 2. Dynamics of nuclear wave packets of $H_2{}^+$ in an intense 760 nm-laser field ($\omega = 0.06E_h/\hbar$ and the envelope $f(t)$ is linearly ramped with t so that after two optical cycles $f(t)$ attains its peak value $f_0 = 0.12E_h/ea_0$). The nuclear packets $|\chi_1(R,t)|^2 = |\langle 1|\Phi\rangle|^2$ and $|\chi_2(R,t)|^2 = |\langle 2|\Phi\rangle|^2$ obtained from the full 3D wave packet $\Phi(z,\rho,R;t)$ are denoted by solid contour lines in (a) and (a′), respectively. Panels (b) and (b′) show $|\chi'_1(R,t)|^2$ and $|\chi'_2(R,t)|^2$ in the two-state model defined by Eq. 15, respectively; panels (c) and (c′) show $|\chi'_1(R,t)|^2$ and $|\chi'_2(R,t)|^2$ in the field-induced coupling model, where the nonadiabatic coupling $\Lambda(R,t)$ in Eq. 16 of the two-state model is replaced by the dominant term $\langle 1|\partial/\partial t|2\rangle$. Level crossing moments at which the two adiabatic energies are closest to each other (i.e., the electric field $\mathcal{E}(t)$ is zero), are indicated in the lower panels by vertical dotted lines.

adiabatic channel. The probability P_{nonad} can be increased as the intensity, frequency, and R are increased. We have obtained conditions for isolated transition (where $\tau_{tr} \ll 2\pi/\omega$);[45] $\omega < \Delta E_{ug}(R)/2 < 2\langle g|z|u\rangle f(t)$ in the adiabatic case and $\max[\omega, \Delta E_{ug}(R)/2] < 2\langle g|z|u\rangle f(t)$ in the diabatic case. In the following section, we show how the nonadiabatic transition between the adiabatic states is correlated to dissociation and ionization processes.

3.3 Electronic and Nuclear Dynamics of $H_2{}^+$ in a Long-Wavelength, Intense Field. We show that, in a long-wavelength, intense field regime, tunnel ionization proceeds in the region $R \geq 2R_e$ through the $|2\rangle$ state populated from $|1\rangle$, where R_e is the equilibrium internuclear distance. The two adiabatic states $|1\rangle$ and $|2\rangle$ (or $1s\sigma_g$ and $1s\sigma_u$) are essential states for describing the electronic dynamics prior to tunnel ionization and nuclear dynamics. To demonstrate these points, we project the "exact" electronic and nuclear wave packet $\Phi(z,\rho,R;t)$ onto $|1\rangle$ and $|2\rangle$. The projected components $\chi_1(R,t) = \langle 1|\Phi\rangle$ and $\chi_2(R,t) = \langle 2|\Phi\rangle$ are regarded as nuclear wave functions associated with $|1\rangle$ and $|2\rangle$. We will show that the solution of the coupled Eq. 15 for the two-state model is qualitatively consistent with the nuclear motion obtained from the exact mapping of $\Phi(z,\rho,R;t)$ onto $|1\rangle$ and $|2\rangle$.

In a long-wavelength, intense field, after one-electron tunnel ionization from H_2, $|1\rangle$ of $H_2{}^+$ is prepared. Since the creation of an ionizing electronic wave packet through tunnelling begins and ends within a very short period, i.e., a half-optical cycle (characteristic of tunnel ionization), the lowest vibrational state $\chi_{\mathrm{vib}=0}(R)$ of H_2 in the ground electronic state $X^1\Sigma_g^+$ is vertically excited to $|1\rangle$ of $H_2{}^+$.[83] We thus employ the following form as the total wave function at $t = 0$ for the 3D simulation: $\Phi(z,\rho,R;t) = \chi_{\mathrm{vib}=0}(R)|1\rangle$ [A more precise form can be given by the product of $\chi_{\mathrm{vib}=0}(R)$ and the ionization probability as a function of R. See Ref. 84]. Here, we simply replace $|1\rangle$ at $t = 0$ with the $1s\sigma_g$ B–O electronic wave function of $H_2{}^+$ (which is a function of R). This replacement does not affect the following conclusions. The "exact" $1s\sigma_g$ B–O electronic wave function is obtained by operating a spectral filter on an approximate initial state.[85,86]

We assume that $H_2{}^+$ interacts with the following laser pulse: $\omega = 0.06E_h/\hbar$ ($\lambda = 760$ nm). The envelope $f(t)$ is linearly ramped with t so that after two optical cycles $f(t)$ attains its peak value $f_0 = 0.12E_h/ea_0$ ($I = 5.0 \times 10^{14}$ W cm^{-2}). The corresponding light intensity I is given by $I = 3.5 \times 10^{16} f_a(t)^2$ W cm^{-2}, where $f_a(t)$ is the value in atomic units of $f(t)$ (i.e., in units of E_h/ea_0). For the numerical calculation, the grid ends in z used were $\pm 30a_0$ and the grid ends in ρ were 0 and $30a_0$. The grid space for R ranges from $\approx 0.01a_0$ to $15a_0$. To eliminate the outgoing ionizing flux and to evaluate the ionization probability, we set absorbing boundaries for the electronic coordinates ρ and z.

The projected vibrational components $\chi_1(R,t) = \langle 1|\Phi\rangle$ and $\chi_2(R,t) = \langle 2|\Phi\rangle$ are shown in Fig. 2a and 2a′, respectively. The atomic unit of time is $\hbar/E_h = 0.024$ fs. The $H_2{}^+$ wave packet starts from the equilibrium internuclear distance $R_e \approx 1.5a_0$ of H_2. Since R_e is longer for $H_2{}^+$ than for H_2, the nuclear wave packet $\chi_1(R,t)$, which is initially $\chi_{\mathrm{vib}=0}(R)$, moves toward larger internuclear distances. Without an external field, the main component of the packet reflects at the outer turning point in E_g at $R \approx 3a_0$, coming back toward the inner turning point. On the other hand, under the condition of an intense pulse, dissociation takes place as well as ionization. When

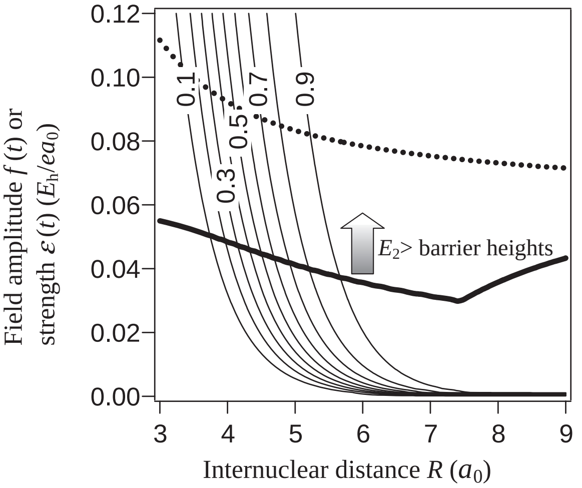

Fig. 3. Landau–Zener type of field-induced nonadiabatic transition probability, P_{nonad}, of $H_2{}^+$ plotted as a function of R and the field amplitude $f(t)$ (solid line). The frequency of the field is $\omega = 0.06E_h/\hbar$. The number attached to a contour line indicates the nonadiabatic transition probability. At field strengths $\mathcal{E}(t)$ above the bold solid line, E_2 is higher than the heights of the inner and outer barriers for tunnel ionization; on the other hand, above the bold dotted line, E_1 is higher than the outer barrier height. The barrier heights defined as those of $V(z,\rho,R) + z\mathcal{E}(t)$ evaluated along the molecular axis are functions of R and $\mathcal{E}(t)$.

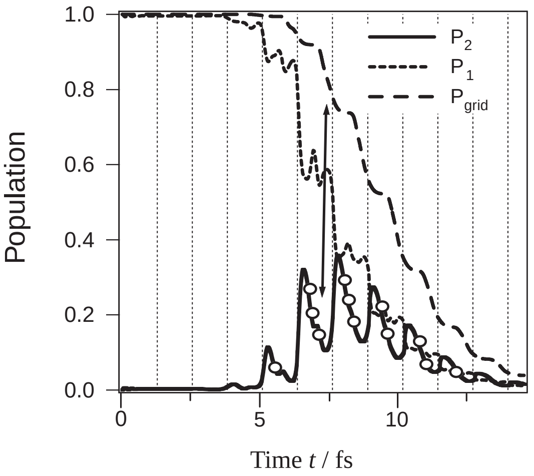

Fig. 4. Overall populations $P_1(t)$ and $P_2(t)$ on the lowest two adiabatic states, $|1\rangle$ and $|2\rangle$, of $H_2{}^+$ in an intense 760 nm-laser field. The populations $P_1(t)$ and $P_2(t)$ integrated over R are denoted by a dotted line and a solid line, respectively. To eliminate the outgoing ionizing flux, we set absorbing boundaries for the electronic coordinates ρ and z. Ionization corresponds to the reduction of the norm of the wave function remaining in the grid space. The total norm in the grid space enclosed with the absorbing boundaries, $P_{\text{grid}}(t)$, is denoted by a broken line. Level crossing points for $H_2{}^+$, where $\mathcal{E}(t) = 0$, are indicated by vertical dotted lines. Around $t = 5.1$ fs ($=4\pi/\omega$), the wave packet approaches $R \approx 3.5a_0$; then, nonadiabatic transitions between $|1\rangle$ and $|2\rangle$ begin. Nonadiabatic transitions occur around level crossing points $t = n\pi/\omega$ for $n \geq 4$ (See Eq. 18). The reduction in $P_2(t)$ denoted by open circles is due to ionization. The upper adiabatic state $|2\rangle$ is regarded as the main doorway state to tunnel ionization. A reduction in $P_2(t)$ corresponds to the subsequent reduction in $P_{\text{grid}}(t)$ (delayed by a time that the ionizing currents need to hit the absorbing boundaries) as indicated by the line with arrows at both ends.

the instantaneous field strength $R|E(t)|$ is large, the potentials $E_1(R,t)$ and $E_2(R,t)$ given by Eq. 13 are distorted, as shown in Fig. 1. The nuclear wave packet is moved toward larger internuclear distances by the field-induced barrier suppression in $E_1(R,t)$ (bond softening due to a laser field).

In the early stage, in which the internuclear distance is small ($R < 3a_0$), the response to the field is adiabatic: The main component of the wave packet is still in $|1\rangle$. At larger R ($>3a_0$), nonadiabatic transitions occur between $|1\rangle$ and $|2\rangle$ when the field $\mathcal{E}(t)$ changes its sign, i.e., when the two adiabatic potential surfaces come closest to each other. As the packet reaches internuclear distances around $R \approx 3.5a_0$, δ becomes as small as 0.23 for $f(t) = 0.12E_h/ea_0$; $P_{\text{nonad}} = 0.24$. In Fig. 3, the nonadiabatic transition probability P_{nonad} is plotted as a function of R and the field amplitude $f(t)$ ($\omega = 0.06E_h/\hbar$). Around $t = 5.1$ fs ($=4\pi/\omega$), as shown in Fig. 2a′, a part of the population in $|1\rangle$ is transferred to $|2\rangle$. The temporally periodic structure in Fig. 2a′ clearly demonstrates that nonadiabatic transitions from $|1\rangle$ to $|2\rangle$ occur at every crossing around $t = j\pi/\omega$ ($j \geq 4$), where $\delta < 1$. The probability $|\chi_2(R,t)|^2$ has a gap around $R = 5a_0$. Owing to high probabilities of nonadiabatic transition between $|1\rangle$ and $|2\rangle$ for $R > 3.5a_0$, the initial nuclear wave packet in $|1\rangle$ bifurcates into two wave packet $\chi_1(R,t)$ and $\chi_2(R,t)$ around $R = 3.5a_0$ for the first time. Because the two wave packet experience a crossing twice in the subsequent one optical cycle, $\chi_1(R,t)$ and $\chi_2(R,t)$ that reach a region around $R = 5a_0$ destructively interfere with each other: $|\chi_2(R,t)|^2$ at $R \approx 5a_0$ becomes almost zero.

Thachuk et al. also examined how classical trajectories are hopped between time-dependent surfaces.[80] The conservation principle to apply during a hop depends upon its physical origin. The nonadiabatic coupling $\partial\Theta/\partial t$ mainly induces energy exchange between the electron and the field. When $\partial\Theta/\partial t$ is dominant as in the case of $H_2{}^+$, nuclear momentum is therefore conserved upon hopping. On the other hand, when $v\partial\Theta/\partial R$ is dominant, energy exchange occurs between the electron and nuclei: The total energy of the molecular system is conserved.

The overall populations $P_1(t) = \int |\chi_1(R,t)|^2 \mathrm{d}R$ and $P_2(t) = \int |\chi_2(R,t)|^2 \mathrm{d}R$ are shown in Fig. 4 together with the total norm in the grid space enclosed with the absorbing boundaries, $P_{\text{grid}}(t)$. An increase in $P_2(t)$ *at a crossing point* coincides with a decrease in $P_1(t)$. During the next half cycle after a nonadiabatic transition (as the field strength approaches a local maximum), a reduction in the population of $|2\rangle$, $P_2(t)$, is clearly observed, whereas $P_1(t)$ changes very little. According to nonadiabatic transition theory, without ionization, $P_1(t)$ and $P_2(t)$ should be constant between adjacent crossing points. The reduction in $P_2(t)$ just after a crossing, denoted by open circles, is hence due to ionization. This is also confirmed by the correlation in reduction between $P_{\text{grid}}(t)$ and $P_2(t)$, as indicated by the line with arrows at both ends. We hence conclude that the state $|2\rangle$ is the main doorway state to tunnel ionization. Enhancement of ionization in H_2^+ around $R > 2R_e$ is due to the joint effect of the following three factors: (i) nonadiabatic transitions from $|1\rangle$ and $|2\rangle$ occur at large R; (ii) $|2\rangle$ is easier to ionize than is $|1\rangle$; (iii) the ionization probability of $|2\rangle$ has peaks around certain internuclear distances $R > 2R_e$.

The reason that $|2\rangle$ is easier to ionize than is $|1\rangle$ can be explained by comparing the adiabatic energies with the barrier heights for tunnel ionization. In addition to the barrier of $V(z,\rho,R) + z\mathcal{E}(t) + 1/R$ between the two wells (inner barrier), when $|\mathcal{E}(t)| \neq 0$, a barrier with finite width is formed outside the descending well (outer barrier). The barrier heights of $V(z,\rho,R) + z\mathcal{E}(t) + 1/R$ evaluated along the molecular axis are also plotted in Fig. 1. Figure 1 clearly demonstrates that, while E_1 is usually below both of the barrier heights, E_2 can be higher than the barrier heights in a range around $R_c \approx 6a_0$. In the intensity region above the bold solid line in Fig. 3, E_2 is higher than the heights of both the barriers; above the bold dotted line, E_1 is higher than the outer barrier height. While the electron goes over or through only the outer barrier in the ionization process from $|1\rangle$, the electron must go over or through both the inner and outer barriers for ionization from $|2\rangle$ [If there is a period in which the energy of the adiabatic state is higher than the barrier(s) for ionization, "overbarrier" ionization outmeasures "underbarrier" tunnel ionization. In this paper, "tunnel ionization" refers to both types of ionization]. Figures 2a, 2a′, and 3 clearly show that the $|2\rangle$ component that is nonadiabatically created from $|1\rangle$ is easier to ionize than is $|1\rangle$, except at the atomic limit where R is much larger than R_e. Figure 3 also shows that below $f(t) = 0.03E_h/ea_0$ ($I = 3 \times 10^{13}\,\mathrm{W\,cm^{-2}}$) ionization hardly occurs and H_2^+ simply dissociates, experiencing nonadiabatic transitions. Using $\chi_1(R,t)$ and $\chi_2(R,t)$, we have determined critical distances R_c and the critical momenta P_c where ionization to H_2^{2+} dominantly occurs. The distribution in conjugate momentum P is obtained by Fourier-transforming $\chi_1(R,t)$ and $\chi_2(R,t)$ with respect to R. The kinetic energies of dissociative fragments originating from Coulomb explosions $H^+ + H^+$ can be estimated.[43]

In Fig. 5, the rate of ionization from $|2\rangle$ in a DC field, Γ_2, is plotted as a function of R. The field strength is fixed at a constant $\mathcal{E}(t) = 0.0533E_h/ea_0$. We solved the time-dependent Schrödinger equation for H_2^+, with nuclei frozen at various values of R,[45] by using the dual transformation method. The ionization rate is obtained by fitting the norm within the space encircled by the boundary planes to an exponential decay form. The results are essentially the same as those obtained by using complex basis sets.[87] Roughly speaking, Γ_2 is large in a wide range from $R = 5a_0$ to $10a_0$, owing to barrier suppressions favorable for tunnel ionization from $|2\rangle$ (in the region of $R < 10a_0$, the rate of ionization from $|1\rangle$ in a DC field, Γ_1, is one-hundredth as large as Γ_2). Besides, a couple of peaks are observed in the range (Γ_2 also has a peak at $R \approx 0.5a_0$). The maximum ionization rate from $|2\rangle$ is found at $R \approx 9a_0$. For this field strength, at $R \approx 9a_0$, however, E_2 is only a little above the inner barrier, as shown in Fig. 1. The fast ionization is attributed to the following facts: at $R \approx 9a_0$, $|2\rangle$ is resonant with an adiabatic state (originating from states other than $1s\sigma_g$ and $1s\sigma_u$) in the descending well that is higher than $|1\rangle$; the outer barrier is thin and is much lower than E_2. Another peak is also found at $R \approx 6a_0$, but it is lower than that at $R \approx 9a_0$. The rate of ionization from $|2\rangle$ seems to be more sensitive to the outer barrier than to the inner barrier. The ionization rate Γ in an alternating intense field is correlated with Γ_2 (e.g. both have peaks at $R = 6a_0$ and $9a_0$), which also indicates that ionization proceeds via the $|2\rangle$ created from the initial state $1s\sigma_g$. As an example, we also show in Fig. 5 the ionization rates Γ in an alternating intense field under the condition that $\omega = 0.0428E_h/\hbar$ ($\lambda = 1064\,\mathrm{nm}$) and the envelope $f(t)$ has its constant peak value $f_0 = 0.0533E_h/ea_0$ ($I = 10^{14}\,\mathrm{W\,cm^{-2}}$) after a five-cycle linear ramp.[88] The initial state is the ground state $1s\sigma_g$. As clearly demonstrated in Fig. 5, the ionization rate Γ changes as Γ_2 (e.g. both have peaks at $R = 6a_0$ and $9a_0$). The ionization rate Γ increases by more than two orders of magnitude as R increases from its equilibrium value of $R_e \approx 2a_0$ to an intermediate region around $R = 6a_0$.

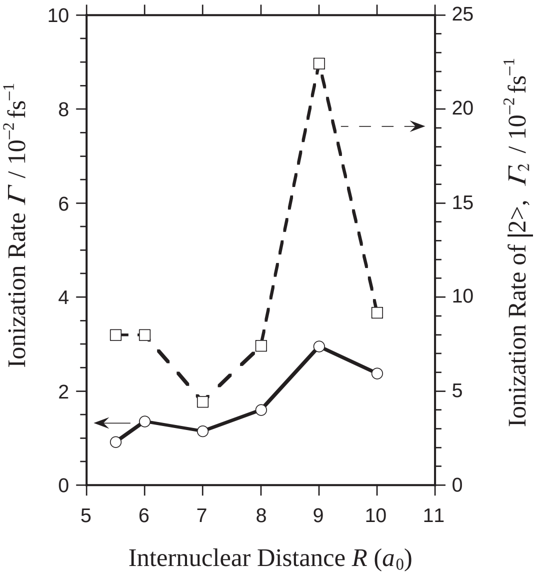

Fig. 5. Ionization rates of H_2^+ as a function of internuclear distance R. The open squares denote ionization rates Γ_2 of the upper adiabatic state $|2\rangle$ at a DC constant field strength $\mathcal{E}(t) = 0.0533E_h/ea_0$ (which corresponds to $I = 10^{14}\,\mathrm{W\,cm^{-2}}$); the open circles denote ionization rates Γ in an alternating intense field of $\lambda = 1064\,\mathrm{nm}$ and $I = 10^{14}\,\mathrm{W\,cm^{-2}}$ under the condition that the initial state is the ground state $1s\sigma_g$ (the field envelope has a five-cycle linear ramp and Γ is defined as the stationary ionization rate after the ramp). The scales for Γ_2 and Γ are marked on the right and left ordinates, respectively.

The above mechanism of ionization is called charge resonance-enhanced ionization[27a] because nonadiabatic transitions occur between the two adiabatic states $|1\rangle$ and $|2\rangle$ arising from a charge resonance pair of $1s\sigma_g$ and $1s\sigma_u$ [See Eq. 11]. The analysis in terms of the populations of the *two* adiabatic states is validated by the fact that, in the high-intensity and low-frequency regime, only these two states are mainly populated before ionization.[41] The bound state components other than $|1\rangle$ and $|2\rangle$ (or the higher B–O bound electronic states other than $1s\sigma_g$ and $1s\sigma_u$) can be as large as 5–10% of the total bound state component. However, all the intermediates other than $|1\rangle$ and $|2\rangle$ (or higher B–O bound electronic states other than $1s\sigma_g$ and $1s\sigma_u$) vanish completely within a quarter cycle due to overbarrier ionization. It is concluded that $|1\rangle$ and $|2\rangle$ (or $1s\sigma_g$ and $1s\sigma_u$) are essential states for describing the electronic dynamics prior to tunnel ionization. The two-state model wave functions $\chi'_1(R,t)$ and $\chi'_2(R,t)$ obtained by solving the coupled Eq. 15 are shown in Figs. 2b and 2b′, respectively. It should be pointed out that the two-state model of Eq. 15 gives nearly the same *nuclear* dynamics as the "exact" projected ones $\chi_1(R,t) = \langle 1|\Phi\rangle$ and $\chi_2(R,t) = \langle 2|\Phi\rangle$, although the population decrease due to ionization cannot be reproduced. This indicates that the nuclear motion in intense fields is determined by the potential surfaces of a small number of time-dependent adiabatic states.

We performed calculations for the two-state model of $H_2{}^+$ on the assumption that in Eq. 16 all the coupling terms other than the dominant direct field-induced term $\langle 1|\partial/\partial t|2\rangle = \partial\Theta/\partial t$ are zero. The wave functions $\chi'_1(R,t)$ and $\chi'_2(R,t)$ obtained by solving the coupled Eq. 15 on this assumption (the field-induced coupling model) are shown in Figs. 2c and 2c′, respectively. As is expected from the discussion in Section **3.2**, no discernible difference was observed between the exact two-state coupling case and the $\langle 1|\partial/\partial t|2\rangle$-coupling case. The dominance of field-induced nonadiabatic coupling is the key to develop a practicable way of estimating the nuclear dynamics of general polyatomic molecules in intense laser fields. The details of a proposed method are given in Section **5**.

The concept of a time-dependent adiabatic state has already proved useful for designing actual experiments. Using the idea of time-dependent adiabatic state, Niikura et al. have designed a scheme to control the vibrational wave packet on the lowest time-dependent adiabatic state of $H_2{}^+$ or $D_2{}^+$.[89] The nature of bond softening of this potential can be temporally controlled by mixing the signal and idler of an optical parametric amplifier. By changing the modulation period of light intensity, they achieved control of the dissociation yield. When the wave packet reached its outer turning point, the Stark-shifted potential allows the molecule to dissociate through bond softening if the laser intensity is high. On the other hand, if the field is weak at this critical time, little dissociation is measured.

Within the framework of the two-state model, the expansion of Eq. 14 in terms of time-dependent adiabatic states is equivalent to

$$|\Psi\rangle = \chi_g(R,t)|g\rangle + \chi_u(R,t)|u\rangle. \tag{21}$$

In the near-infrared regime, however, the time-dependent adiabatic state expansion like Eq. 14 has an advantage over the expansion in terms of field-free states like Eq. 21. For example, in the expansion using time-dependent adiabatic states, only a small number of *low-lying* adiabatic states are required to describe the electronic and nuclear dynamics of a molecule in intense laser fields. This is a crucial advantage in the case of polyatomic molecules. See also Section **5**.

4. Two-Electron Dynamics of H_2 in an Intense Laser Field

The mechanism of ionization of $H_2{}^+$ is called charge resonance-enhanced ionization. In the case of multielectron molecules, however, different mechanisms can be expected; field-induced intramolecular electron transfer between nuclei triggers strong electron–electron correlation. For H_2, localized ionic-bond states H^+H^- and H^-H^+ are expected to be created in an intense field. The formation of localized ionic states should be related to the internuclear distance of H_2. To elucidate possible mechanisms of ionization of H_2, one must answer the question as to how electron correlation dynamics in an intense laser field is affected by the molecular structure. It is expected that the clarified mechanism of enhanced ionization for H_2 would serve as a prototype of ionization of multielectron molecules in intense fields.

In this section, we present the results of an investigation of the two-electron wave packet dynamics of H_2 in an intense linearly polarized field. H_2 has six electronic degrees of freedom for two electrons. The position of the *j*th electron is designated by cylindrical coordinates (ρ_j, z_j, and φ_j). The z-axis is set parallel to the molecular axis, with the origin of the z-axis located at the midpoint between the two nuclei separated by an internuclear distance R. Here, we assume that the molecular axis is parallel to the polarization direction of a linearly polarized laser electric field $\mathcal{E}(t)$ (parallel polarization condition).[10] Then, the two-electron wave function can be represented by five coordinates: z_1, z_2, ρ_1, ρ_2, and $\phi = \varphi_1 - \varphi_2$.

We applied the dual transformation method to H_2.[20,30–32,39] As in the case of $H_2{}^+$, both the original electronic wave function Φ and the Hamiltonian $\hat{H}$ are transformed to Φ^T and $\hat{H}^T$ consistently so that the numerical difficulties arising from the divergence of the Coulomb potentials are overcome. The time integration of the Schrödinger equation $i\partial\Phi^T/\partial t = H^T\Phi^T$ is carried out using the alternating implicit direction (ADI) formula.[78] The numerical procedure has been described in detail in Refs. 20 and 39.

4.1 Electronic Wave Packet Dynamics at Different Internuclear Distances. Although the molecular axis is assumed to be parallel to the polarization direction, the two-electron wave function still has five degrees of freedom. Here, to represent the wave packet, we employ the reduced density $\bar{P}(z_1, z_2)$ obtained by integrating the square of the wave function, $|\Phi(t)|^2$, over the degrees of freedom other than z_1 and z_2 parallel to the polarization direction:[20,39,44]

$$\bar{P}(z_1, z_2) = \int_0^\infty d\rho_1 \int_0^\infty d\rho_2 \times \int_0^{2\pi} d\phi \rho_1 \rho_2 |\Phi(\rho_1, \rho_2, z_1, z_2, \phi)|^2. \tag{22}$$

This representation is useful because the electronic dynamics in H_2 is characterized by electron motion along the polarization direction z. The covalent bond configurations (H•H) around $z_1 = -z_2 = \pm R/2$ and the ionic-bond configurations (H^+H^- and H^-H^+) around $z_1 = z_2 = \pm R/2$ can be distinguished by using Eq. 22. As an example, $\bar{P}(z_1, z_2)$ for the exact ground state $X^1\Sigma_g^+$ at $R = 4a_0$ is drawn in Fig. 6a. The reduced density map clearly demonstrates that the covalent components around $z_1 = -z_2 = \pm R/2$ are dominant in the ground state at $R = 4a_0$. The localized ionic components $|H^+H^-\rangle$ and $|H^-H^+\rangle$ contained are both 19%, where the electronic states of $|H^+H^-\rangle$ and $|H^-H^+\rangle$ are defined as H^- ions of which the centers are located at $z_1 = z_2 = \pm R/2$. In the calculation of the H^- state, electron–electron repulsion is exactly taken into account.

The field $\mathcal{E}(t)$ that the H_2 interacts with is assumed to be

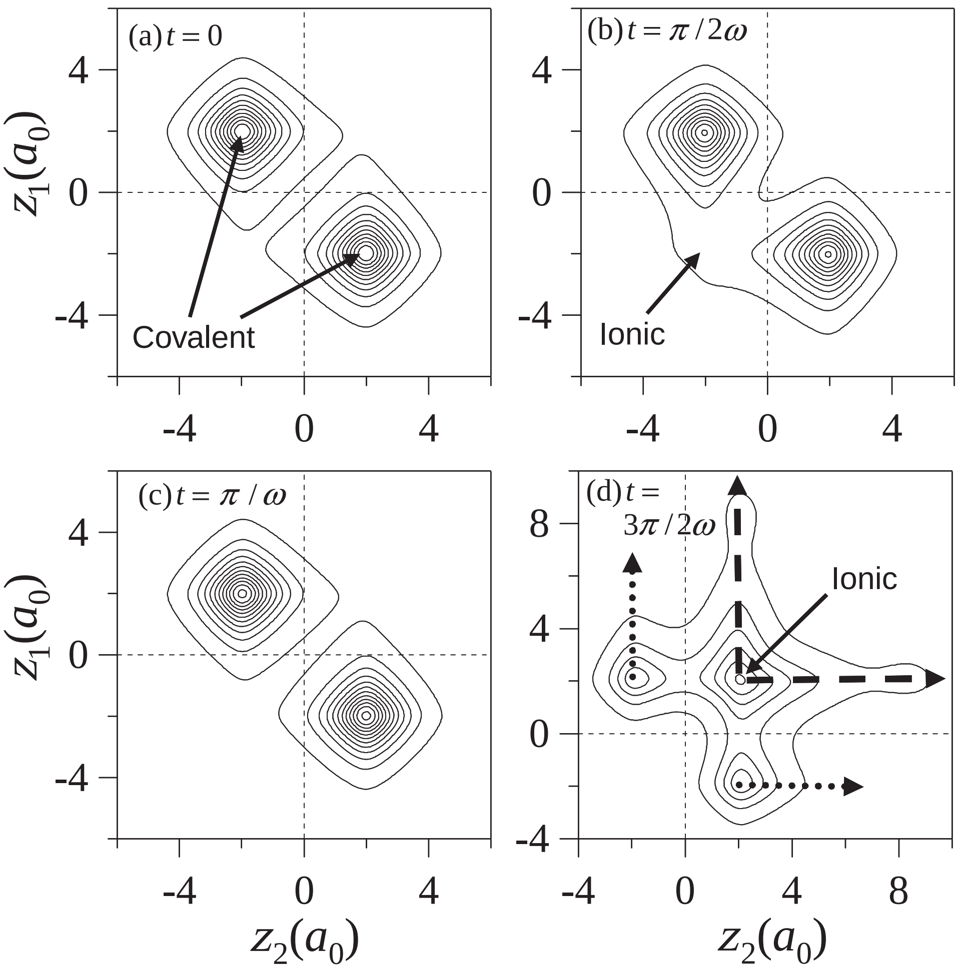

Fig. 6. Electronic wave packet dynamics of H_2 in an intense 760 nm-laser field ($\omega = 0.06E_h/\hbar$). The internuclear distance is fixed at $R = 4a_0$. The reduced density $\bar{P}(z_1, z_2)$ defined by Eq. 22 is drawn at quarter cycle intervals: (a) $t = 0$; (b) $t = \pi/2\omega = 0.63$ fs; (c) $t = \pi/\omega = 1.27$ fs; (d) $t = 3\pi/2\omega = 1.90$ fs. The contour lines in the four panels are plotted at the same intervals. The field strength is $\mathcal{E}(t) = 0.03E_h/ea_0$ at $t = \pi/2\omega$ and $\mathcal{E}(t) = -0.09E_h/ea_0$ at $t = 3\pi/2\omega$. The initial state shown in (a) is the ground state X characterized by the covalent-bond component around $z_1 = -z_2 = \pm R/2$. The ionic-bond component H^-H^+ around $z_1 = z_2 = -R/2$ (at the left nucleus) increases as the field approaches the first local maximum at $t = \pi/2\omega$, as shown in (b). The wave packet at $\mathcal{E}(t = \pi/\omega) = 0$ in (c) is nearly identical to the initial one in (a). In (d), the density around the ionic configuration ($z_1 = z_2 = R/2$) becomes very high because of the stronger field strength at $t = 3\pi/2\omega$. As indicated by the broken line in (d), an electron is ejected from the localized ionic configuration. The direct ionization current from the covalent configurations denoted by the dotted line in (d) is relatively small.

$f(t)\sin\omega t$, where ω is the frequency, and the pulse envelope $f(t)$ is linearly ramped with time t so that $f(t)$ attains its maximum f_0 after one cycle. The field parameters used are as follows: $f_0 = 0.12E_h/ea_0$ (intensity $I = 5.04 \times 10^{14}$ W cm^{-2}) and $\omega = 0.06E_h/\hbar$ ($\lambda = 760$ nm). The instantaneous field strength is $\mathcal{E}(t) = 0.03E_h/ea_0$ at $t = \pi/2\omega$ (which corresponds to $I = 3.15 \times 10^{13}$ W cm^{-2}); $\mathcal{E}(t) = -0.09E_h/ea_0$ at $t = 3\pi/2\omega$ ($I = 2.84 \times 10^{14}$ W cm^{-2}).

We have calculated the wave packet dynamics at different values of R. The initial state at $t = 0$ is the ground state $X^1\Sigma_g^+$.

4.1.1 $R = 4a_0$: Shown in Fig. 6 are snapshots of $\bar{P}(z_1, z_2)$ for $R = 4a_0$ taken at the following four moments: (a) $t = 0$; (b) $t = \pi/2\omega = 26.2\hbar/E_h = 0.634$ fs ($\hbar/E_h = 0.0242$ fs); (c) $t = \pi/\omega$; (d) $t = 3\pi/2\omega$. In a low-frequency intense field, an ionic component is created around the descending potential well, where the electrostatic potential for each electron, i.e., the dipole interaction energy $z_1\mathcal{E}(t)$ or $z_2\mathcal{E}(t)$, is negative. For instance, the left well where z_1 and $z_2 \approx -R/2$ is the descending well when $\mathcal{E}(t) > 0$. As the field approaches $t = \pi/2\omega$, the ionic component created around the left nucleus ($z_1 = z_2 = -R/2$) increases to $|\langle\Phi|H^-H^+\rangle|^2 = 0.31$ from 0.19 at $t = 0$. Note that $\mathcal{E}(t = \pi/2\omega) > 0$. The corresponding reduced density map is shown in Fig. 6b. The laser field forces the two electrons to stay near a nucleus for almost one half cycle. When the field returns to zero at $t = \pi/\omega$, the packet shown in Fig. 6c is almost identical to the initial one shown in Fig. 6a, indicating that the response to the field is nearly adiabatic.

Until $t = \pi/\omega$, no ionization current is observed on the scale of the contour line intervals. A quarter cycle later, at $t = 3\pi/2\omega$, as shown in Fig. 6d, the population of the ionic component around $z_1 = z_2 = R/2$ becomes as large as $|\langle\Phi|H^-H^+\rangle|^2 = 0.54$ because of the stronger field $\mathcal{E}(t = 3\pi/2\omega) = -0.09E_h/$

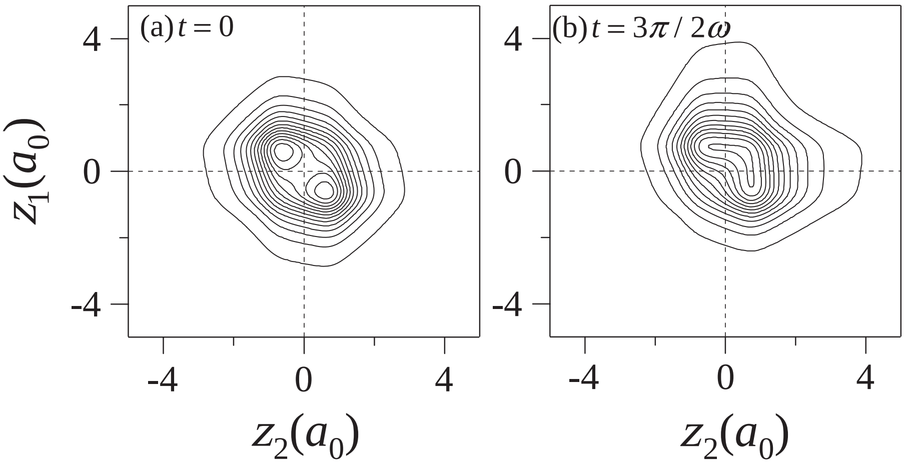

Fig. 7. Snapshots of the reduced density of H_2 at $R = 1.6a_0$: (a) $t = 0$, (b) $t = 3\pi/2\omega$. The applied pulse is the same as that used in Fig. 6. Despite the intense field strength at $t = 3\pi/2\omega$, the ionization current is very small.

ea_0. From 3D analysis of the spatial configuration of the two electrons, we have confirmed that the ionic component created in the descending well is the H^- ion at the nucleus where the dipole interaction energy is negative. In the case of $R = 4a_0$, the population of a localized ionic component is maximized around the time when the absolute value of the field strength takes a local maximum; then, the population of the counter-localized ionic component is minimized. This means that the response of the bound state component to the field is still adiabatic. The increase in a localized ionic component is caused by the loss of the counter-localized ionic component through an intermediate covalent configuration.

As indicated by the broken line in Fig. 6d, an electron is ejected from the localized ionic structure $|H^+H^-\rangle$. If the distance between the two nuclei is so long that the Coulomb interaction between H^+ and H^- is negligible, the ionization potential of the localized ionic structure is considered to be as low as $I_p(H^-) = 0.75$ eV. The localized ionic structure is hence unstable and is regarded as a doorway state to ionization. The direct ionization route from a covalent structure is denoted by a dotted line in Fig. 6d, but the current along the dotted line is relatively small. At $R = 4a_0$, the rate of ionization from a *pure* ionic state is at least five-times greater than that from a *pure* covalent state (deduced from the ionizing flux).

4.1.2 $R = 1.6a_0$: The reduced densities at $t = 0$ and $3\pi/2\omega$ for $R = 1.6a_0$ ($\approx R_e = 1.4a_0$) are shown in Figs. 7a and 7b. Despite the intense field strength at $t = 3\pi/2\omega$, the ionization current is very small. This is consistent with the ionization rates of the lowest adiabatic state in static fields calculated by Saenz.[90] He has reported that the ionization rate in a *static* field of $\mathcal{E} = 0.08E_h/ea_0$ increases from $R = 1.6a_0$ to $4a_0$ by a factor of 40.

For $R = 1.6a_0$, $|\langle\Phi|H^+H^-\rangle|^2$ is as large as 0.74 at $t = 3\pi/2\omega$, while $|\langle\Phi|H^+H^-\rangle|^2 = 0.58$ at $t = 0$. As R decreases, the population of H^+H^- (or H^-H^+) becomes larger; however, the rate of ionization from a pure ionic state H^+H^- or H^-H^+ decreases owing to the more attractive force of the distant nucleus exerted on the electron pair. At $R = 1.6a_0$, $|\langle\Phi|H^+H^-\rangle|^2$ is large, but the electron cloud shrinks in comparison with the pure H^+H^- or H^-H^+. We also note that the increase in $|\langle\Phi|H^+H^-\rangle|^2$ from $t = 0$ to $t = 3\pi/2\omega$ is only 0.16 for $R = 1.6a_0$, while it is 0.35 for $R = 4a_0$. This suggests that the unstable part of the existing H^+H^- is smaller for $R = 1.6a_0$ than for $R = 4a_0$.

4.1.3 $R = 6a_0$ and $8a_0$: Snapshots of the reduced density for $R = 6a_0$ are shown in Fig. 8. The initial reduced density for $R = 6a_0$ shown in Fig. 8a indicates that the ground electronic state at large R is a state dominated by covalent character. For $R = 6a_0$, $|\langle\Phi|H^+H^-\rangle|^2$ at $t = 0$ is as small as 0.016; for $R = 8a_0$, it further reduces to 6×10^{-4}. The reduced density at $t = 3\pi/2\omega = 1.90$ fs for $R = 6a_0$ is shown in Fig. 8b. The population of H^+H^- in an intense field becomes smaller as R increases. Around $t = 3\pi/2\omega$, $|\langle\Phi|H^+H^-\rangle|^2$ is at most 0.06 for $R = 6a_0$ and is very small, less than 0.004, for $R = 8a_0$. The decrease in the H^+H^- population is unfavorable for tunnel ionization.

In addition to the populations of H^+H^- and H^-H^+, there exists yet another factor that determines the ionization rate. The ratios of the ionization probability at $t = 2\pi/\omega$ to the unstable component of H^+H^- around $t = 3\pi/2\omega$ ($= |\langle\Phi(t = 3\pi/2\omega)|H^+H^-\rangle|^2 - |\langle\Phi(t = 0)|H^+H^-\rangle|^2$) are 1, 6, 20, and 140 for $R = 1.6a_0$, $4a_0$, $6a_0$, and $8a_0$, respectively; the ratio of the ionization probability to the unstable component of H^+H^- (or H^-H^+) increases as R increases. One of the reasons for this tendency is that the created H^+H^- becomes more unstable as R increases: The attractive force that the distant proton H^+ exerts on the electrons in H^- becomes weaker. We have confirmed that ionization from the created ionic state occurs rapidly. A large part of the ionic component decays to Volkov states; that is, for $R \geq 6a_0$, the created H^+H^- ionizes completely within a half optical cycle ($\approx$1.27 fs), as shown in Fig. 8c. This is again consistent with Saenz's result[90] that the lifetime of a pure H^+H^- in a static field with $\mathcal{E} = 0.06E_h/ea_0$ is shorter than 0.5 fs for $R \geq 6a_0$ (Since the ionic and covalent states have no overlap at large R, each state can be assigned to an adiabatic state in a static field.). For $R \geq 6a_0$, $|\langle\Phi|H^+H^-\rangle|^2$ reaches the maximum at about $t = 20\hbar/E_h$ before the field reaches the local maximum at $t = 3\pi/2\omega$, which reflects the rapid ionization of the created H^+H^- within a half optical cycle.

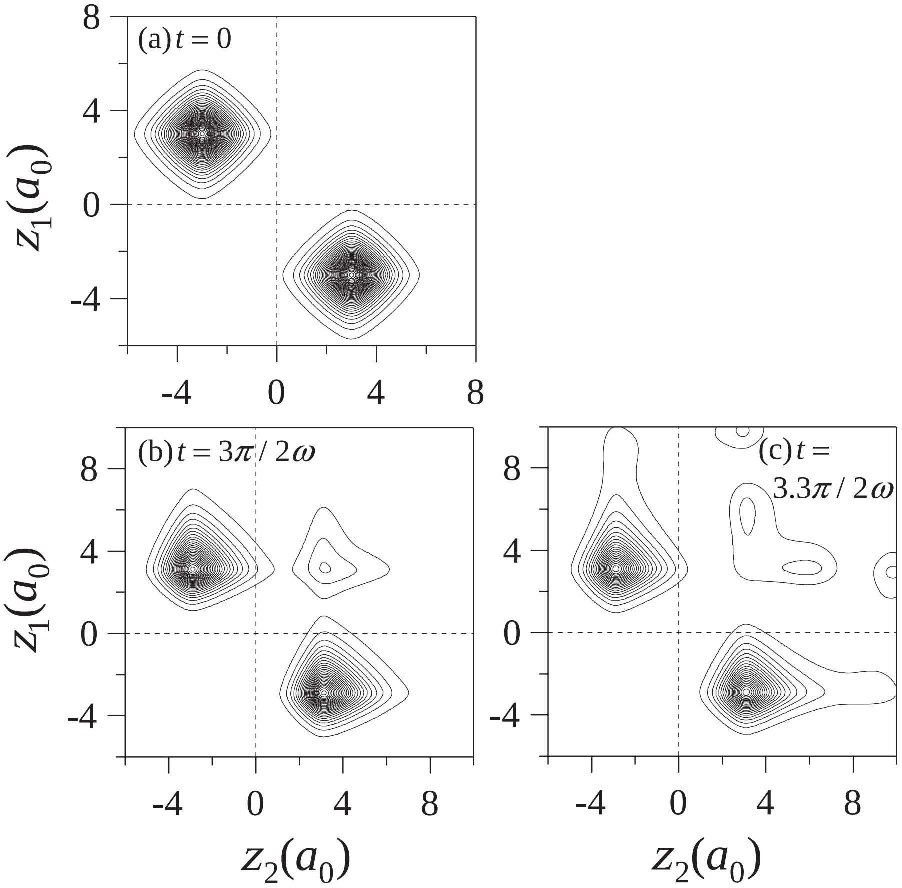

Fig. 8. Snapshots of the reduced density of H_2 at $R = 6a_0$: (a) $t = 0$, (b) $t = 3\pi/2\omega$, (c) $t = 3.3\pi/2\omega$. The applied pulse is the same as that used in Fig. 6. The drastic change from (b) to (c) indicates rapid ionization from the created ionic state around $z_1 = z_2 = R/2$. The contour intervals in Fig. 8 are one-third of those in Fig. 6 or 7.

Another reason why the ratio of the ionization rate to the population $|\langle\Phi|\mathrm{H}^+\mathrm{H}^-\rangle|^2$ increases as R increases is the significant ionization from the covalent state at large R. Figures 8b and 8c show that the ionizing currents from the ionic and covalent configurations for $R = 6a_0$ are of the same order of magnitude. As mentioned previously, the ionization rate of a “pure” covalent state is small. For $R = 6a_0$, the ionization rate of a “pure” covalent state in a static field with $\mathcal{E} = 0.06E_\mathrm{h}/ea_0$ is about one-fourth as large as that of an “pure” ionic state (for $\mathcal{E} = 0.08E_\mathrm{h}/ea_0$, one-tenth).[90] On the other hand, as shown in Fig. 8, the remaining covalent component is much larger than the created ionic component $|\langle\Phi|\mathrm{H}^+\mathrm{H}^-\rangle|^2$ (which is at most only 0.06 around $t = 3\pi/2\omega$). Therefore, for $R = 6a_0$, as well as the ionization of the created localized ionic component, the direct ionization from the dominant covalent component significantly contributes to the total ionization probability.

For $R = 8a_0$, as shown in Fig. 9, the creation of an ionic state is greatly suppressed in comparison with the cases of smaller internuclear distances. As mentioned previously, $|\langle\Phi|\mathrm{H}^+\mathrm{H}^-\rangle|^2$ around $t = 3\pi/2\omega$ is less than 0.004. Moreover, the ionization rate of an ionic state reaches a ceiling at large R ($\geq 6a_0$), where the attractive force exerted by the distant nuclei becomes negligible. The ionization rate from a covalent state is also almost independent of R if the field is strong enough to lower the ionization barrier of an H atom to the initial energy $-I_\mathrm{p}(\mathrm{H})$. In this case, the ionization processes of two nearly isolated H atoms are triggered by field-dominated one-electron motion and are independent of each other. The minimum field strength required for barrier suppression ionization of H is given by $I_\mathrm{p}^2(\mathrm{H})/4 \approx 0.063E_\mathrm{h}/ea_0$. This is consistent with the result that the ionization rate of the covalent state is almost independent of R ($\geq 6a_0$) in a static field of $\mathcal{E} \geq 0.08E_\mathrm{h}/ea_0$.[90] Hence, if the field strength is beyond the barrier suppression strength of H, the ionization rate of the covalent state, as well as that of the ionic state, is almost independent of R: The main ionization route at large R ($>8a_0$) is a direct one from the dominant covalent component.

If the intensity is below a threshold value, for instance, if $\mathcal{E}(t) < 0.04E_\mathrm{h}/ea_0$ at $R = 8a_0$, such creation of an ionic state is inhibited: The dependence of the ionization rate on R is governed by the ionization rate of the covalent state. In a static field of $\mathcal{E} < 0.04E_\mathrm{h}/ea_0$, as R increases from $6a_0$, the ionization rate of the covalent state decreases up to $R \approx 10a_0$.[90] This implies that in the case of a weak field the polarization enhanced by two-electron correlation participates in field-induced ionization from the covalent state. As R increases, this type of polarization diminishes; therefore, in the case of a weak field, the ionization rate of the covalent state decreases with increase in R up to a certain large internuclear distance.

In conclusion, the main doorway state to ionization is the localized ionic state $\mathrm{H}^-\mathrm{H}^+$ or $\mathrm{H}^+\mathrm{H}^-$. As R increases, while the population of $\mathrm{H}^-\mathrm{H}^+$ decreases, a pure ionic state $\mathrm{H}^-\mathrm{H}^+$

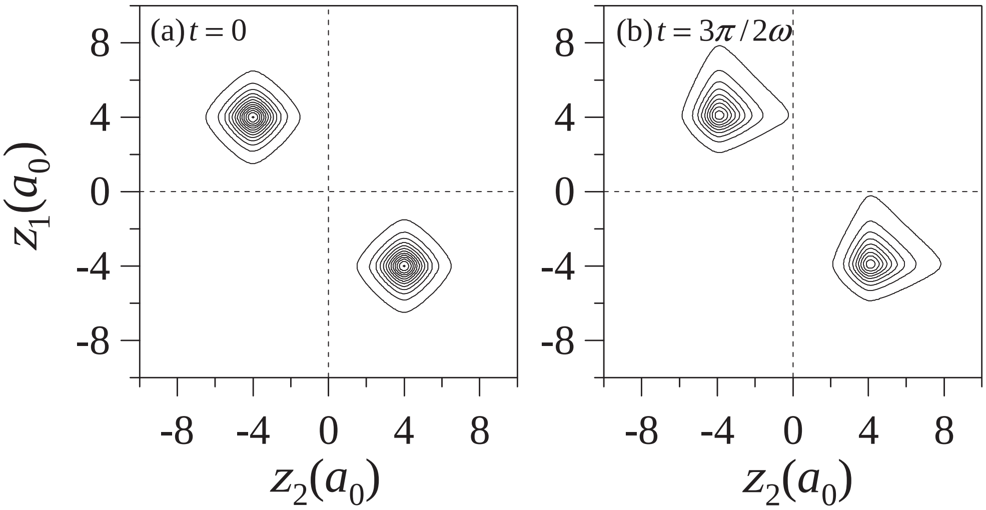

Fig. 9. Reduced density of H_2 at $R = 8a_0$: (a) $t = 0$ and (b) $t = 3\pi/2\omega$. The applied pulse is the same as that used in Fig. 6. The contour intervals are the same as those in Fig. 6 or 7.

becomes more unstable in a field because of the weaker attractive force of the distant H^+. As a result, ionization is enhanced in the critical range from $R = 4a_0$ to $R = 6a_0$.

We have also investigated the intramolecular electronic dynamics that governs the ionization process by analyzing the populations of field-following adiabatic states defined as eigenfunctions of the instantaneous electronic Hamiltonian. In a high-intensity and low-frequency regime, only a limited number of adiabatic states participate in the intramolecular electronic dynamics, i.e., dynamics of bound electrons. The effective instantaneous Hamiltonian for H_2 is constructed from three main electronic states: X, $B^1\Sigma_u^+$, and EF[91] (At large R, the last two electronic states are replaced with the ungerade and gerade ionic states.). By solving the time-dependent Schrödinger equation for the 3×3 effective Hamiltonian, we have found that the difference in electronic and ionization dynamics between the small R case and the large R case originates in the character of the level crossing of the lowest two adiabatic states.

As the field strength increases, the lowering second lowest adiabatic state $|2\rangle$ comes closer to the lowest adiabatic state $|1\rangle$ starting from the X state. The transition period in which a nonadiabatic transition between $|1\rangle$ and $|2\rangle$ is completed is much smaller than the quarter optical cycle $\pi/2\omega$. Thus, a nonadiabatic transition is localized around the time t_c when the field strength $\mathcal{E}(t)$ reaches the value required for a crossing, $\mathcal{E}(t_c)$. In the case of $R \leq 4a_0$, the energy gap at the avoided crossing between $|1\rangle$ and $|2\rangle$ is as large as that at zero field strength. As a result, the probabilities of nonadiabatic transitions to upper adiabatic states are small. When $|\mathcal{E}(t)|$ is larger than $|\mathcal{E}(t_c)|$, $|1\rangle$ is ionic, while $|2\rangle$ is covalent. Therefore, ionization occurs from state $|1\rangle$ characterized by a localized ionic state H^+H^- or H^-H^+ directly to Volkov states. In the case of large R ($>4a_0$), nonadiabatic transitions occur from $|1\rangle$ to $|2\rangle$ when these two states cross each other. For $R > 6a_0$, ionization proceeds mainly through state $|2\rangle$, which is a covalent character-dominated state when $|\mathcal{E}(t)| > |\mathcal{E}(t_c)|$. The three-state problem can be reduced to a two-state problem by prediagonalizing the 2×2 matrix constructed in terms of the upper two states B and EF. On the basis of the two-state model, an analytical expression of the field strength required for the crossing of $|1\rangle$ and $|2\rangle$ is derived; moreover, the probability of a nonadiabatic transition between $|1\rangle$ and $|2\rangle$ is expressed by the Landau–Zener formula. The results based on these simple formulas agree with those in the three-state treatment.

4.2 Two-Electron Dynamics of a Triplet State. Early measurements indicated that intense laser ionization rates (and ATI spectra) of diatomics are nearly equal to those of atoms with similar electron binding energies. In recent works, however, the ionization yield of O_2 has been found to be greatly suppressed, relative to Xe, an atom with nearly the same ionization potential as O_2.[92] Faisal et al.[93] attributed the suppression effect to the *one-electron character* of the highest occupied MOs of O_2; the antibonding orbitals cause a destructive interference between the two subwaves of the ionizing electron emerging from the two atomic centers.

We discuss here a *two-electron character*, namely, the role of exchange symmetry in ionization of H_2. The singlet cases discussed above are compared with triplet cases where the initial state is the lowest triplet state $b^3\Sigma_u^+$. Since the spin–orbit coupling is negligible, the wave function in the triplet case is spatially antisymmetric with respect to exchange of the two electrons. The same laser pulse as used in Figs. 6–9 is applied to the $b^3\Sigma_u^+$ state at $R = 4a_0$. Figure 10 shows the reduced density for the triplet case at $t = 3\pi/2\omega$. In contrast with the singlet case, an ionic component, expected to be unstable, is unlikely to be created owing to the Pauli exclusion principle. For the triplet case, electron transfer from the ascending well toward the descending well is suppressed. The ionization rate is reduced to about one third from the $X^1\Sigma_g^+$ case to the $b^3\Sigma_u^+$ case. Considering that the energy of the $b^3\Sigma_u^+$ state is even higher than that of the $X^1\Sigma_g^+$ state by $0.023E_h$ at $R = 4a_0$, we conclude that the inhibition of ionic-state formation due to the Pauli principle is responsible for the reduction in the ionization rate. This again indicates that the formation of an ionic state plays a dominant role in intense field-induced ionization of H_2. At least for ionization of two-electron diatomics, electron-spin multiplicity should be taken into account.

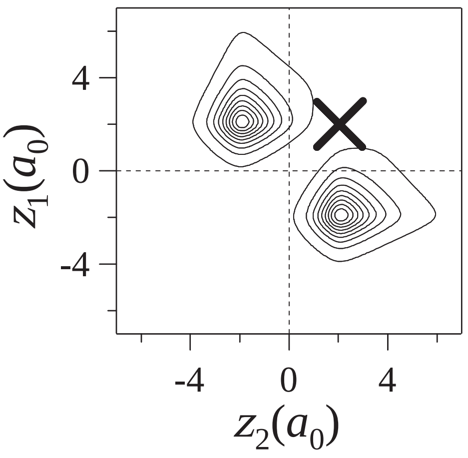

Fig. 10. Reduced density for a triplet case of H_2 at $t = 3\pi/2\omega = 1.90\,\mathrm{fs}$. The applied pulse is the same as that used in Fig. 6. The initial state is the $b^3\Sigma_u^+$ state, and the internuclear distance is fixed at $R = 4a_0$. The symbol × denotes an unoccupied ionic configuration site. Creation of an ionic component due to electron transfer from well to well is suppressed in comparison with the singlet case in Fig. 6: The ionization rate in the $b^3\Sigma_u^+$ case is reduced to about one third of that in the $X^1\Sigma_g^+$ case.

5. Description of Dynamics of Polyatomic Molecules in Intense Laser Fields by Time-Dependent Adiabatic States

The description of molecular dynamics in terms of time-dependent adiabatic states developed in Sections **3** and **4** is applicable to *polyatomic* molecules in intense laser fields. We here present an outline of a time-dependent adiabatic state approach[48] and provide a recipe of procedures for calculating the nuclear wave packet dynamics of arbitrary polyatomic molecules.

There is a well-known approach to treat dynamics in intense fields, namely, the Floquet (dressed state) method targeted for long-time pulses with a constant envelope.[94] In the Floquet method, a molecule-field state is given by a product of a photon state and an adiabatic state in a zero field denoted by $|N-\ell\rangle$ and $|\Phi_j\rangle$, respectively. Here, N is the number of photons before the interaction and ℓ is the number of photons absorbed by the molecule; the corresponding *diabatic* field-dressed potential is given by $\hbar\omega(N-\ell)+E_j(\{R\})$. The *adiabatic* field-dressed states can be obtained by diagonalizing the R-fixed Hamiltonian including the molecule-field interactions among diabatic field-dressed states. This approach is especially useful for estimating the momenta of fragment ions and is now applicable to short pulses with a time-varying envelope.[95] From a practical point of view, however, the range of its application is rather limited to simple diatomic molecules such as $H_2{}^+$.[95,96] In this approach, it is necessary to calculate all of the field-free adiabatic states involved in the process under consideration (including *high-lying* states) and, moreover, the field-free states obtained are then dressed with photon number states. The number of photons absorbed or emitted, ℓ, can be much larger than one. Application of the Floquet approach to polyatomic molecules is therefore a very laborious process. On the other hand, the present time-dependent adiabatic state approach has the advantage that only a small number of *low-lying* adiabatic states that can be efficiently calculated by MO methods are required to describe the electronic and nuclear dynamics of a molecule in intense laser fields. It should be pointed out that many field-free excited states are involved even in the lowest adiabatic state $|1\rangle$.

5.1 Construction of the Instantaneous Electronic Hamiltonian.

To obtain the time-dependent adiabatic potential surfaces of a polyatomic molecule, we must construct the instantaneous electronic Hamiltonian $H_{\mathrm{el}}(t)$. Taking a polyatomic molecule of N_{e} electrons and N_{n} nuclei as an example, we demonstrate the way of constructing $H_{\mathrm{el}}(t)$. The Cartesian coordinates of the jth electron are denoted by $\vec{r}_{\mathrm{e},j} = (x_{\mathrm{e},j}, y_{\mathrm{e},j}, z_{\mathrm{e},j})$ and those of the jth nucleus are denoted by $\vec{r}_{\mathrm{n},j} = (x_{\mathrm{n},j}, y_{\mathrm{n},j}, z_{\mathrm{n},j})$. The charge of jth nucleus is denoted by e_j. The temporal oscillation of the applied laser electric field is given by $\vec{e}_\varepsilon\mathcal{E}(t)$, where $\vec{e}_\varepsilon$ is the polarization vector of the field. In a long-wavelength case, the interaction with the field can be expressed by the dipole interaction

$$\begin{aligned}
&-\left[-e\sum_j^{N_{\mathrm{e}}}\vec{r}_{\mathrm{e},j}+\sum_j^{N_{\mathrm{n}}}e_j\vec{r}_{\mathrm{n},j}\right]\cdot\vec{e}_\varepsilon\mathcal{E}(t)\\
&\quad=-\left[-e\sum_j^{N_{\mathrm{e}}}(\vec{r}_{\mathrm{e},j}-\vec{r}_{\mathrm{c}})+\sum_j^{N_{\mathrm{n}}}e_j(\vec{r}_{\mathrm{n},j}-\vec{r}_{\mathrm{c}})\right]\\
&\qquad\cdot\vec{e}_\varepsilon\mathcal{E}(t)-Q\vec{r}_{\mathrm{c}}\cdot\vec{e}_\varepsilon\mathcal{E}(t)\\
&\qquad\equiv-\vec{\mu}_{\mathrm{int}}\cdot\vec{e}_\varepsilon\mathcal{E}(t)-Q\vec{r}_{\mathrm{c}}\cdot\vec{e}_\varepsilon\mathcal{E}(t),
\end{aligned}\tag{23}$$

where $\vec{r}_{\mathrm{c}}$ denotes the center of mass of the molecule, and Q is the total charge of the molecule (for instance, $Q=+2$ for a dication). The vectors $\vec{r}_{\mathrm{e},j}-\vec{r}_{\mathrm{c}}$ or $\vec{r}_{\mathrm{n},j}-\vec{r}_{\mathrm{c}}$ in the dipole moment $\vec{\mu}_{\mathrm{int}}$ can be expressed in terms of appropriate relative coordinates. In the dipole approximation, therefore, the center of mass of the molecule can be separated from the internal degrees of freedom.[18] The center of mass of the molecule moves in a field potential $-Q\vec{r}_{\mathrm{c}}\cdot\vec{e}_\varepsilon\mathcal{E}(t)$ as a particle with the total mass and total charge $+Q$ of the whole molecule; the term $-Q\vec{r}_{\mathrm{c}}\cdot\vec{e}_\varepsilon\mathcal{E}(t)$ should not be included in the Hamiltonian for the internal degrees of freedom.

In the following derivation of internal Hamiltonians and MO calculations, the center of mass, $\vec{r}_{\mathrm{c}}$, is assumed to be equal to the center of mass of the nuclei, $\vec{r}_{\mathrm{n}}$, because the difference is negligible in the present problem. Thus, the coordinates of the jth electron are given by the relative coordinates $\vec{r}_{\mathrm{e},j}-\vec{r}_{\mathrm{n}}$; the nuclear coordinates measured from $\vec{r}_{\mathrm{n}}$ can be expressed in terms of internal (vibrational) coordinates and molecular rotation:

$$\vec{\mu}'_{\mathrm{int}}=-e\sum_j^{N_{\mathrm{e}}}(\vec{r}_{\mathrm{e},j}-\vec{r}_{\mathrm{n}})+\sum_j^{N_{\mathrm{n}}}e_j(\vec{r}_{\mathrm{n},j}-\vec{r}_{\mathrm{n}}),\tag{24}$$

where $\{R\}$ denotes a set of vibrational coordinates and rotational angles of the molecule. We hence can define the instantaneous electronic Hamiltonian $H_{\mathrm{el}}(\{R\},t)=H_{\mathrm{el}}(t)$ by adding $-\vec{\mu}'_{\mathrm{int}}\cdot\vec{e}_\varepsilon\mathcal{E}(t)$ to the field-free adiabatic electronic Hamiltonian $H^0_{\mathrm{el}}(\{R\})$ as

$$H_{\mathrm{el}}(\{R\},t)=H^0_{\mathrm{el}}(\{R\})-\vec{\mu}'_{\mathrm{int}}\cdot\vec{e}_\varepsilon\mathcal{E}(t).\tag{25}$$

All the coordinates must be measured from the center of the nuclei, $\vec{r}_{\mathrm{n}}$, for $Q\neq 0$.

5.2 Calculation of Time-Dependent Adiabatic Potentials. In diagonalization of $H_{\mathrm{el}}(\{R\},t)$, both $\{R\}$ and t are treated as adiabatic parameters as in the case of $H_2{}^+$:

$$H_{\mathrm{el}}(\{R\},t)\psi(\{R\},t) = E(\{R\},t)\psi(\{R\},t). \tag{26}$$

The eigenvalues $E(\{R\},t)$ are time-dependent adiabatic potentials for nuclear motion. The eigenvalue problems of Eq. 26 for the neutral molecule and its cations at various internuclear distances and instantaneous field strengths can be solved by using MO methods such as the multiconfiguration self-consistent-field (MCSCF) method.[97] The dependence of $E(\{R\},t)$ on t originates from $\mathcal{E}(t)$. It is therefore only necessary to solve eigenvalue problems at various static field strengths between the minimum and maximum of $\mathcal{E}(t)$. The values of $E(\{R\},t)$ at arbitrary interpolation points of R and t can be obtained by using spline techniques or by functional fitting.

5.3 Calculation of Field-Induced Nonadiabatic Coupling Elements. In a high-intensity regime, field-following adiabatic potential surfaces can cross each other in energy (avoided level crossing), resulting in the occurrence of nonadiabatic transitions between adiabatic states.[19,39–45,82,90,98] The field-induced nonadiabatic coupling between two time-dependent adiabatic states $\psi_{\mathrm{a}}(t)$ and $\psi_{\mathrm{b}}(t)$, $\langle\psi_{\mathrm{a}}(t)|\partial/\partial t|\psi_{\mathrm{b}}(t)\rangle$, is expressed as

$$\langle\psi_{\mathrm{a}}(t)|\partial/\partial t|\psi_{\mathrm{b}}(t)\rangle = \mu_{\mathrm{ab}}(t)[\partial\mathcal{E}(t)/\partial t]/[E_{\mathrm{a}}(t) - E_{\mathrm{b}}(t)], \tag{27}$$

where $E_{\mathrm{a}}(t)$ and $E_{\mathrm{b}}(t)$ are adiabatic energies of $\psi_{\mathrm{a}}(t)$ and $\psi_{\mathrm{b}}(t)$, and $\mu_{\mathrm{ab}}(t) = \langle\psi_{\mathrm{a}}(t)|\mu'_{\mathrm{int}}\cdot\vec{e}_{\mathcal{E}}|\psi_{\mathrm{b}}(t)\rangle$ is the polarization direction component of the electronic transition dipole moment (Needless to say, these quantities are also functions of $\{R\}$). Equation 27 can be easily obtained by differentiating $H_{\mathrm{el}}(t)\psi_{\mathrm{a}}(t) = E_{\mathrm{a}}(t)\psi_{\mathrm{a}}(t)$ or $H_{\mathrm{el}}(t)\psi_{\mathrm{b}}(t) = E_{\mathrm{b}}(t)\psi_{\mathrm{b}}(t)$ with respect to time t. Calculation of transition dipole moments such as $\mu_{\mathrm{ab}}(t)$ at a static field strength is routinely implemented in MO package programs.

5.4 Construction of the Coupled Equations for Nuclear Dynamics. According to the results of $H_2{}^+$, we assume for general polyatomic molecules that field-induced nonadiabatic transitions are the dominant ones. Field-induced nonadiabatic transitions occur when the field-induced coupling $\langle\psi_{\mathrm{a}}(t)|\partial/\partial t|\psi_{\mathrm{b}}(t)\rangle$ becomes as large as the energy gap $|E_{\mathrm{a}}(t) - E_{\mathrm{b}}(t)|$ (The field-induced nonadaiabatic transition probability based on the Landau–Zener formula[82,98] is given by $P_{\mathrm{ab}} = e^{-2\pi\delta}$, where δ is the ratio $|[E_{\mathrm{a}}(t) - E_{\mathrm{b}}(t)]/8\langle\psi_{\mathrm{a}}(t)|\partial/\partial t|\psi_{\mathrm{b}}(t)\rangle|$ evaluated at the avoided crossing). For molecules more complex than $H_2{}^+$, employing field-induced terms $\langle\psi_{\mathrm{a}}(t)|\partial/\partial t|\psi_{\mathrm{b}}(t)\rangle$ as the dominant nonadiabatic coupling term (all the derivatives with R are ignored), we solve the coupled equations for time-dependent adiabatic states as in Eq. 15. Construction of the coupled equations for an arbitrary number of adiabatic states $\{|j\rangle\}$ is thus straightforward. The diagonal elements are, in addition to the kinetic energy operator for vibrational modes, the energies of time-dependent adiabatic states involved, $\{E_j(t)\}$; the off-diagonal elements are the field-induced nonadiabatic couplings among them, $\{\langle i|\partial/\partial t|j\rangle\}$. The coupled equations for an arbitrary pulse shape can be solved numerically.

5.5 Switching to Cation Stages. In an intense laser field, a neutral molecule ionizes to a monocation stage, and then to multiply charged cations. Quantum chemical calculations of field following adiabatic states are required for each stage, i.e., the neutral molecule, monocation, dication, etc. Besides, we need to know when an ionization process occurs during the interaction with the applied pulse. It is necessary to establish a criterion as to when one switches, e.g., from the neutral to the monocation stage. To be theoretically consistent with the present time-dependent adiabatic state approach, one must calculate the ionization probability of a time-dependent adiabatic state or an electronic wave packet of a linear combination of time-dependent adiabatic states. However, this challenging task is still difficult to perform. In the present study, to switch to other cation stages, we employ a criterion based on appearance intensities at which cations are experimentally detected. As mentioned in Section **4**,[20,39] ionization of H_2 proceeds via a formation of a localized ionic state H^+H^- (or H^-H^+). On the basis of this fact, we have also proposed the simple electrostatic view that each atom in a molecule is charged by field-induced electron transfer and that ionization proceeds via the most unstable (most-negatively or least-positively charged) atomic site.[39–45] From this simple electrostatic consideration based on the characteristic features of electronic dynamics of molecule, we have also derived a semiempirical formula for the estimate of the light intensity required for ionization of a molecule (which is expressed as a function of the ionization potentials of constituent atoms and the positions of nuclei). The formula can be used as an alternative criterion for switching, as shown in Refs. 48 and 66.

6. Characteristic Features of Nuclear Dynamics of CO_2 in Near-Infrared Intense Fields

We have investigated the dynamics of structural deformations of CO_2 and its cations in a near-infrared intense laser field on the basis of the time-dependent adiabatic state approach. The adiabatic potential surfaces $E(\{R\},t)$ and wave functions $\psi(\{R\},t)$ of CO_2 and its cations are calculated by using the full-optimized reaction space MCSCF method[97] with the 6-311G(d) basis set[99] (unless otherwise noted). The MCSCF active space contains all of the valence orbitals and valence electrons. For a nonzero field case, the MOs and the expansion coefficients of the configuration state functions are optimized by incorporating the dipole interaction $-\mu'_{\mathrm{int}}\mathcal{E}(t)$ into the Hamiltonian of the MCSCF method. All ab initio MO calculations are performed using the GAMESS suite of program codes.[100]

6.1 Derivation of Vibrational Hamiltonians of CO_2. As shown in Fig. 11, the three atoms O, C, and O of CO_2 are designated by 1, C, and 2, respectively. The Cartesian coordinates of the C atom are denoted by $(x_{\mathrm{c}}, y_{\mathrm{c}}, z_{\mathrm{c}})$, and those of the jth O atom are denoted by (x_j, y_j, z_j). We denote the mass of a C atom by m_{C} and that of an O atom by m_{O}. After separating the center of mass from the total nuclear system, we obtain the kinetic energy for the internal nuclear degrees of freedom as follows:

$$\hat{T} = \sum_{\ell=x,y,z}\left\{-\frac{\hbar^2}{2\mu}\left(\frac{\partial^2}{\partial r_{1\ell}{}^2} + \frac{\partial^2}{\partial r_{2\ell}{}^2}\right) + \frac{\hbar^2}{m_{\mathrm{C}}}\frac{\partial^2}{\partial r_{1\ell}\partial r_{2\ell}}\right\}, \tag{28}$$

where the reduced mass μ is given by $\mu = m_{\mathrm{C}}m_{\mathrm{O}}/(m_{\mathrm{C}} + m_{\mathrm{O}})$

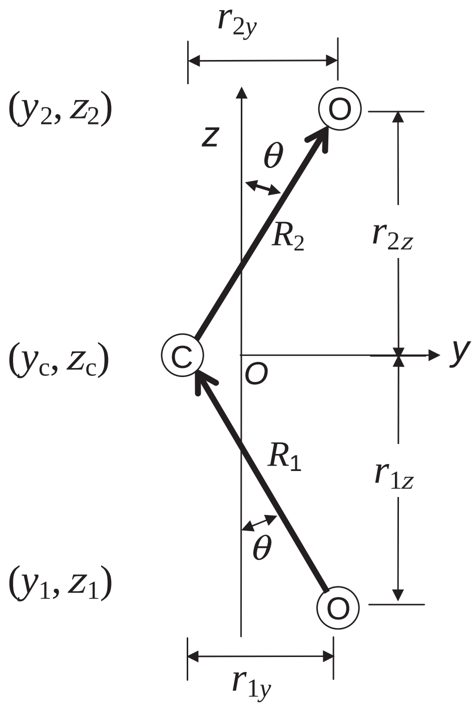

Fig. 11. Coordinates of a triatomic molecule CO_2 on the y–z plane. The Cartesian coordinates of the C atom are denoted by (y_C, z_C), and those of the jth O atom are denoted by (y_j, z_j). The relative coordinates $\{r_{1y}, r_{2y}, r_{1z}, r_{2z}\}$ are defined as $r_{1y} = y_C - y_1$, $r_{2y} = y_2 - y_C$, $r_{1z} = z_C - z_1$, and $r_{2z} = z_2 - z_C$; R_1 and R_2 denote the lengths of the two C–O bonds. The angle between the z-axis and the C–O bond direction is denoted by θ.

and the relative coordinates $\{r_{1x}, r_{2x}, r_{1y}, r_{2y}, r_{1z}, r_{2z}\}$ are defined as $r_{1z} = x_C - x_1, r_{2z} = x_2 - x_C, \ldots$, as shown in Fig. 11.

In the following, although a linearly polarized intense laser field can align molecules,[10] we assume that the molecule does not rotate during the interaction with a laser pulse. The rotational motion of a molecule cannot follow the rapid optical oscillation of a near-infrared field $\mathcal{E}(t)$ but can follow the change in a slowly varying electric field envelope $f(t)$. The effective potential $\bar{V}(\chi)$ for molecular rotation of a linear molecule is then given by averaging the instantaneous potential over one optical cycle $2\pi/\omega$:[10a,101]

$$\bar{V}(\chi) = -(\alpha_{zz} - \alpha_{yy})(\cos\chi)^2 f^2(t)/4, \tag{29}$$

where χ is the angle between the molecular axis and the polarization direction of the field $\mathcal{E}(t)$, and α_{zz} and α_{yy} ($=\alpha_{xx}$) are the molecular axis component and the perpendicular component of the polarizability, respectively. For the experimentally determined value $\alpha_{zz} - \alpha_{yy} = 13.8a_0^3$ of CO_2,[102] the potential depth is about 0.15 eV ($\approx$1200 cm^{-1}) at $I \approx 3 \times 10^{13}$ W cm^{-2}. Above this intensity, the appearance of $CO_2{}^+$ is experimentally confirmed.[103] The depth of $\approx$1200 cm^{-1} is sufficiently large to align CO_2 at room temperature. However, to achieve a high degree of alignment in the polarization direction by adiabatic following of the molecular rotation to the pulse envelope $f(t)$, the pulse length must be longer than the time scale of rotational motion, i.e., $2\pi/2B \approx 40$ ps, where B ($\approx$0.39 cm^{-1}) is the rotational constant of CO_2.[70b,104] Since the length of the pulse used in the experiment ($\approx$100 fs) is much shorter than $2\pi/2B$, alignment motion is negligible.

Without rotation, the degrees of freedom of a CO_2 molecule are reduced to 4 vibrational modes, namely, two bond stretching modes and two degenerate modes for bond angle bending. In this paper, we consider only two degrees of freedom and employ two effective vibrational Hamiltonians that are suitable for describing the nuclear dynamics of CO_2 in intense fields.[48] The first one is constructed from the two bond-stretching modes of CO_2 in the case of linear geometry, and the second one is constructed from the symmetric bond stretching and bond angle bending modes.

6.1.1 One-Dimensional Space (Linear Geometry Case): First, we assume that the molecule is linear and is aligned parallel to the polarization direction z: $r_{1x} = r_{2x} = r_{1y} = r_{2y} = 0$ (No bending is taken into account). In this case, r_{1z} and r_{2z} can be replaced with the O–C bond length R_1 and C–O bond length R_2, respectively. From the z component in Eq. 28, we obtain the vibrational kinetic energy in the case of linear geometry:[105]

$$\hat{T}_z = -\frac{\hbar^2}{2\mu}\left(\frac{\partial^2}{\partial {R_1}^2} + \frac{\partial^2}{\partial {R_2}^2}\right) + \frac{\hbar^2}{m_C}\frac{\partial^2}{\partial R_1 \partial R_2}. \tag{30}$$

The symmetric and antisymmetric stretching modes are represented by

$$R_s = (R_1 + R_2)/2, \tag{31a}$$

and

$$R_a = R_1 - R_2, \tag{31b}$$

respectively. The total vibrational Hamiltonian $\hat{H}_z$ consists of the vibrational kinetic energy operator T_z for the two bond-stretching coordinates R_1 and R_2 and an adiabatic potential energy $E_z(R_1, R_2, t)$ in a laser field $\mathcal{E}(t)$ obtained from Eq. 26. Calculation of the time evolution of the vibrational wave packet is carried out by using the split-operator technique[85,106,107] for a small time increment Δt.

6.1.2 Two-Dimensional Space: We have also treated a case in which the molecule is placed on the y–z plane; i.e., $r_{1x} = r_{2x} = 0$. Neglecting antisymmetric stretching and molecular rotation, we obtained the kinetic energy operator for the symmetric stretching $R \equiv R_s$ and bending mode θ:

$$\begin{aligned}\hat{T}_{s-b} = &-\frac{\hbar^2 M}{4m_O m_C}\left(\sin^2\theta\frac{\partial^2}{\partial R^2} - \frac{\sin 2\theta}{R^2}\frac{\partial}{\partial\theta} + \frac{\sin 2\theta}{R}\frac{\partial^2}{\partial R \partial\theta}\right.\\ &\left. + \frac{\cos^2\theta}{R}\frac{\partial}{\partial R} + \frac{\cos^2\theta}{R^2}\frac{\partial^2}{\partial\theta^2}\right)\\ &- \frac{\hbar^2}{4m_O}\left(\cos^2\theta\frac{\partial^2}{\partial R^2} + \frac{\sin 2\theta}{R^2}\frac{\partial}{\partial\theta} - \frac{\sin 2\theta}{R}\frac{\partial^2}{\partial R \partial\theta}\right.\\ &\left. + \frac{\sin^2\theta}{R}\frac{\partial}{\partial R} + \frac{\sin^2\theta}{R^2}\frac{\partial^2}{\partial\theta^2}\right),\end{aligned} \tag{32}$$

where $\theta = \theta_1 = \theta_2$ is the angle between the x axis and a C–O bond axis, as shown in Fig. 11. The bond bending angle in the conventional definition corresponds to $\pi - 2\theta$. In this two-dimensional model, the O–O axis is parallel to the polarization direction of $\mathcal{E}(t)$ (z axis) and the adiabatic energy is symmetric with respect to the sign of $\mathcal{E}(t)$. Since the kinetic energy operator contains product forms such as those of θ and $\partial/\partial\theta$, we used the Lanczos method[107,108] for wave packet propagation, which can be used for any form of the Hamiltonian operator.

6.2 Results of CO_2 Dynamics. In an intense field, cations created are successively ionized at large internuclear distances (due to enhanced ionization), and the resultant multiply-charged cations undergo Coulomb explosions (due to repulsion among positively charged atomic sites).[9–14,24] On the basis of distribution patterns in a covariance map of fragment ions,[109] Cornaggia studied the geometrical structures of CO_2 cations that are about to Coulomb-explode and suggested the existence of a large amplitude bending motion.[110] The structures of created cations can now be precisely determined by measuring the momentum vector distributions with mass-resolved momentum imaging[111] and coincidence momentum imaging.[112] By using these momentum imaging techniques, Hishikawa et al. investigated the geometrical structure of exploding $CO_2{}^{3+}$ in a 1.1-PW cm^{-2}, 100-fs pulse ($\lambda = 795$ nm) and found that the C–O bond length is stretched to about 1.7 Å and that the mean amplitude of bending is large (the mean bending angle from linear geometry being $\approx 20°$).[24] However, the structural deformation stage, i.e., the stage in which the structural change that leads to the identified structures of exploding cations is induced, has not been experimentally determined yet. In the following, we present the results of investigations of the molecular dynamics of CO_2 and its cations in a near-infrared intense laser field to explain the observed structure of exploding $CO_2{}^{3+}$.

6.2.1 Neutral CO_2 and $CO_2{}^+$: The equilibrium structure of the ground electronic state of neutral CO_2 in a zero field is linear and the equilibrium internuclear distance for a C–O bond, R_e, is 1.16 Å (The calculated value obtained by the present MCSCF approach is 1.17 Å). We discuss the nuclear motion of neutral CO_2 in a field. For $\omega_{\rm elec} \gg \omega$, where $\omega_{\rm elec}$ represents the characteristic frequency for electronic transitions, the present approach has an advantage because the vibrational motion is mainly determined by the lowest adiabatic state.

We have calculated the potential surface of the lowest adiabatic state of CO_2 as a function of the two C–O bond distances R_1 and R_2 (and the bond angle 2θ). Bond stretching can be classified into two types: symmetric two-bond stretching, in which $R_1 = R_2$, and one-bond stretching, in which one C–O bond is longer than the other (e.g., $R_1 > R_2 \approx R_e$). The field-free potential of the lowest state of CO_2 in the case of linear geometry, $E_{z,1}(R_1, R_2, \mathcal{E} = 0)$, is shown in Fig. 12a. In an intense field, as shown by the slope along R_1 in Fig. 12b, the adiabatic potential $E_{z,1}(R_1, R_2, t)$ is greatly distorted; the dissociation energy for a C–O bond is $\approx$7 eV in a zero field and is reduced to 4 eV at a moment of $\mathcal{E}(t) = 0.1E_h/ea_0$. However, structural deformation such as one-bond stretching does not occur even at $f(t) \approx 0.1E_h/ea_0$ as explained below.

The key is the fact that when the sign of the field is reversed, the dissociation energy for the C–O bond under consideration (for R_1) increases, as shown in Fig. 12c. A time-dependent adiabatic potential surface $E_z(R_1, R_2, t)$ can be fitted to the following conventional form:

$$\begin{aligned} &E_z(R_1, R_2, t) \\ &\quad = V_x(R_1, R_2, \mathcal{E} = 0) - \mu(R_1, R_2)\mathcal{E}(t) - \frac{1}{2}\alpha(R_1, R_2)\mathcal{E}^2(t) \\ &\quad - \frac{1}{3}\beta(R_1, R_2)\mathcal{E}^3(t) - \frac{1}{4}\gamma(R_1, R_2)\mathcal{E}^4(t) + \ldots, \end{aligned} \tag{33}$$

where $E_z(R_1, R_2, \mathcal{E} = 0)$ is the potential surface in a zero field. Since $-\mu(R_1, R_2)$ in the second term $-\mu(R_1, R_2)\mathcal{E}(t)$ is more or less proportional to the antisymmetric coordinate R_a, the barrier for one of the one-bond dissociation (two-body breakup) channels O + CO and OC + O is greatly reduced when $|\mathcal{E}(t)|$ is large, as mentioned above. It should, however, be noted that the following inequality in temporal or energy scale holds:

$$\omega_{\rm elec} > \omega > \omega_{\rm vib} > \dot{f}(t)/f(t) \approx 1/T_{\rm p}, \tag{34}$$

where $\omega_{\rm vib}$ is a characteristic vibrational frequency and $T_{\rm p}$ is the pulse length. The experimental condition $\omega \gg \omega_{\rm vib}$ means that the change in $\mathcal{E}(t)$ is too fast for the vibrational motion to follow the change in $\mathcal{E}(t)$ adiabatically. Moreover, $\omega \gg \dot{f}(t)/f(t)$ means that $f(t)$ does not change in one optical cycle $2\pi/\omega$ (which is much shorter than $T_{\rm p}$). The nuclear dynamics is thus expected to be governed by the effective potential given by replacing $\mathcal{E}^j(t)$ in $E_x(R_1, R_2, t)$ with the average $(\omega/2\pi)\int_{t-\pi/\omega}^{t+\pi/\omega} \mathcal{E}^j(t'){\rm d}t'$ over one optical cycle (where $j = 1, 2, \ldots$):[40]

$$\begin{aligned} \bar{E}_z(R_1, R_2, t) &= E_z(R_1, R_2, \mathcal{E} = 0) \\ &\quad - \frac{1}{4}\alpha(R_1, R_2)f^2(t) - \frac{3}{32}\gamma(R_1, R_2)f^4(t) + \ldots. \end{aligned} \tag{35}$$

The actual dynamics is thus governed by the pulse envelope $f(t)$. The cycle-averaged potential $\bar{E}_z(R_1, R_2, t)$ at $f(t) = 0.1E_h/ea_0$ is shown in Fig. 12d. Since the odd order terms of $\mathcal{E}(t)$ in $\bar{E}_z(R_1, R_2, t)$, such as the dipole interaction term, disappear, the barrier for the one-bond dissociation in $\bar{E}_z(R_1, R_2, t)$ is as high as the field-free value in Fig. 12a.

The dissociation energy in $\bar{E}_z(R_1, R_2, t)$ for the symmetric stretching mode is reduced from 15.5 to 13.5 eV as $f(t)$ increases from 0 to $f(t) = 0.1E_h/ea_0$: α in the leading perturbation term in $\bar{E}_z(R_1, R_2, t)$ has a ridge along the line $R_1 = R_2$. However, this reduction is not large enough to induce symmetric bond stretching. Besides, a comparison between Figs. 12a and 12d shows that the equilibrium geometry in $\bar{E}_z(R_1, R_2, t)$ is, up to $f(t) \approx 0.1E_h/ea_0$, almost equal to that in a zero field. Since $\omega_{\rm vib} > \dot{f}(t)/f(t)$, the υth vibrational state in a zero field is adiabatically transferred to the υth state of $\bar{E}_z(R_1, R_2, t)$. Therefore, little bond stretching occurs, and the width of the wave function does not increase much. Bending motion is not induced for $f(t) \leq 0.1E_h/ea_0$, either: At a fixed internuclear distance, the curvature of the potential along θ increases as $|\mathcal{E}(t)|$ increases. The appearance intensity of $CO_2{}^+$, i.e., the minimum intensity at which $CO_2{}^+$ is experimentally detected, is $I \approx 3 \times 10^{13}$ W cm^{-2} [$f(t) \approx 0.03E_h/ea_0$].[113] This value is much smaller than $f(t) = 0.1E_h/ea_0$.

We thus conclude that CO_2 maintains its stable linear structure around $R_e \approx 1.17$ Å even at field strengths $f(t) \approx 0.1E_h/ea_0$ beyond the appearance intensity of $CO_2{}^+$. In the case of small R, the energy difference between the first excited and ground electronic states ($\approx$9 eV) is much larger than ω ($\approx$1.6 eV): Only the lowest adiabatic state is populated, as we have assumed. In the $CO_2{}^+$ stage, ionization occurs before the field intensity becomes high enough to deform the molecule, as in the neutral case.

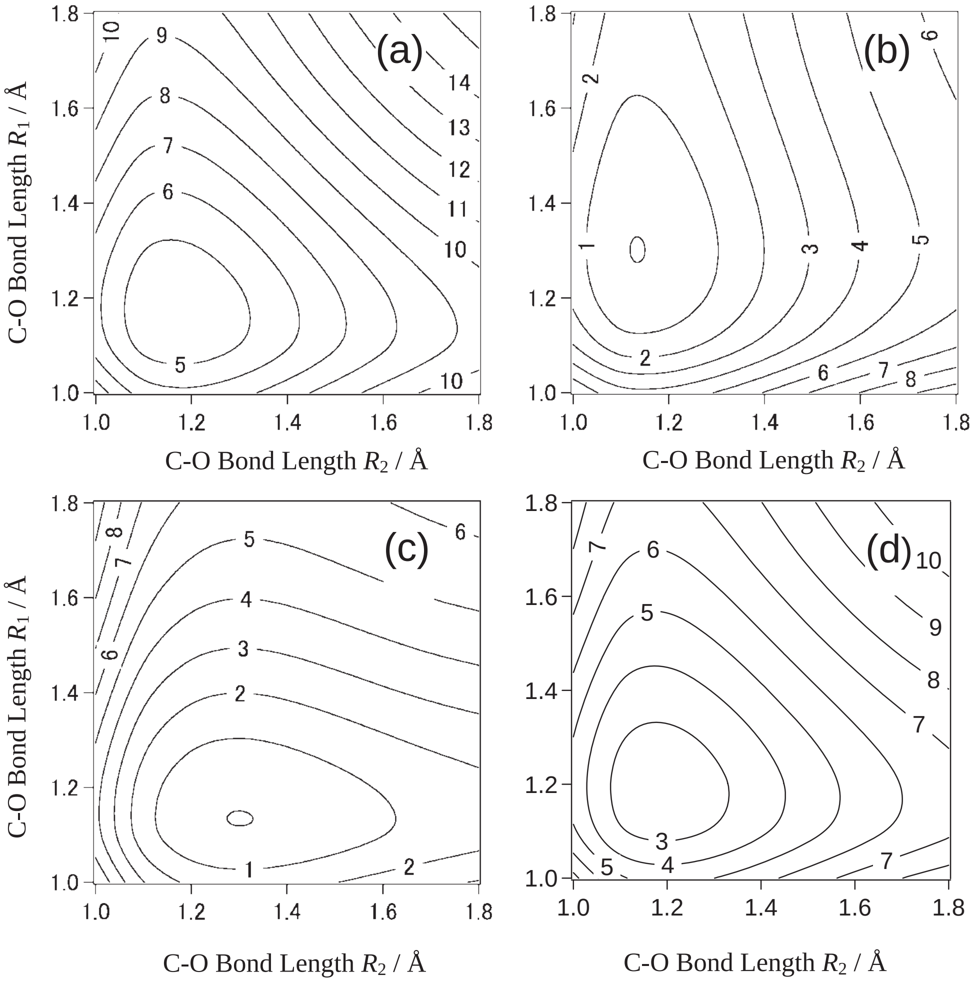

Fig. 12. Potential surfaces of the lowest adiabatic state of CO_2 as a function of the two C–O bond distances R_1 and R_2. The contour lines are plotted at intervals of 1 eV. The field-free potential of the lowest state is shown in (a). The adiabatic potentials $E_z(R_1, R_2, t)$ at $\mathcal{E}(t) = \pm(1/10)E_h/ea_0$ are shown in (b) and (c), respectively. While the dissociation energy for a C–O bond is $\approx$7 eV in a zero field, it is greatly reduced, for instance, to 4 eV at a moment of $\mathcal{E}(t) = (1/10)E_h/ea_0$ as shown in (b). However, structural deformation such as one-bond stretching hardly occurs even at $f(t) \approx 0.1E_h/ea_0$. The nuclear dynamics is in fact governed by an effective potential, i.e., the average of $E_z(R_1, R_2, t)$ over one optical cycle. The cycle-averaged potential at $f(t) = 0.1E_h/ea_0$ is shown in (d). Panels (a)–(c) are reproduced from Ref. 48.

6.2.2 $CO_2{}^{2+}$ Molecule: In the stage of $CO_2{}^{2+}$, consideration must be given to at least the lowest three adiabatic states of $CO_2{}^{2+}$, the ground triplet state adiabatically connected with the $^3B_1$ state ($^3\Sigma_g^-$ in the case of linear geometry) in a zero field and the nearly degenerate lowest singlet states connected with $^1A_1$ and $^1B_1$ in a zero field ($^1\Delta_g$ in the case of linear geometry). The energy difference between $^1A_1$ and $^3B_1$ in a zero field is as small as $\approx$1.5 eV ($\approx$one photon energy) near the equilibrium geometry of $R_e \approx 1.2$ Å. When $CO_2{}^+$ is ionized, the light intensity can already reach a region higher than $I \approx 5 \times 10^{13}$ W cm^{-2}.[113] Therefore, there is a possibility that the higher states $^1A_1$ and $^1B_1$ are also populated to some extent. However, the dynamical behaviors of nuclei for the three states will be nearly alike, because the potential surfaces of the lowest three adiabatic states have nearly the same shape over a wide range of field strengths.[47]

Since Coulomb explosions of $O^+ + C^+ + O^+$ are experimentally observed at high intensity $I \geq 3 \times 10^{14}$ W cm^{-2} [113] (the appearance intensity of triply charged species), the small differences in the ionization potential between the lowest three adiabatic states of $CO_2{}^{2+}$ will make only a small difference in the ionization rate. Therefore, the electronic and nuclear dynamics in the $CO_2{}^{2+}$ stage are expected to be nearly the same irrespective of which state is prepared among the lowest three adiabatic states. As will be shown below, structural deformation of $CO_2{}^{2+}$ can occur before most of $CO_2{}^{2+}$ are ionized (the saturation intensity for ionization of $CO_2{}^{2+}$, $I \geq 10^{15}$ W cm^{-2}, is much higher than the appearance intensity of triply charged species).

6.2.2.1 Simultaneous Two-Bond Stretching; The nuclear dynamics of $CO_2{}^{2+}$ in the linear geometry case is examined as a representative case of field-induced structural deformation. We present the results of calculation of the nuclear wave packet dynamics in the lowest adiabatic state potential $E_{z,1}(R_1, R_2, t)$. The dissociation energy in a zero field is $\approx$11 eV in the case of symmetric two-bond stretching ($\approx$5 eV smaller than that of CO_2) and ca. 1 eV in the case of one-bond stretching. From the viewpoint of dissociation energy, it is

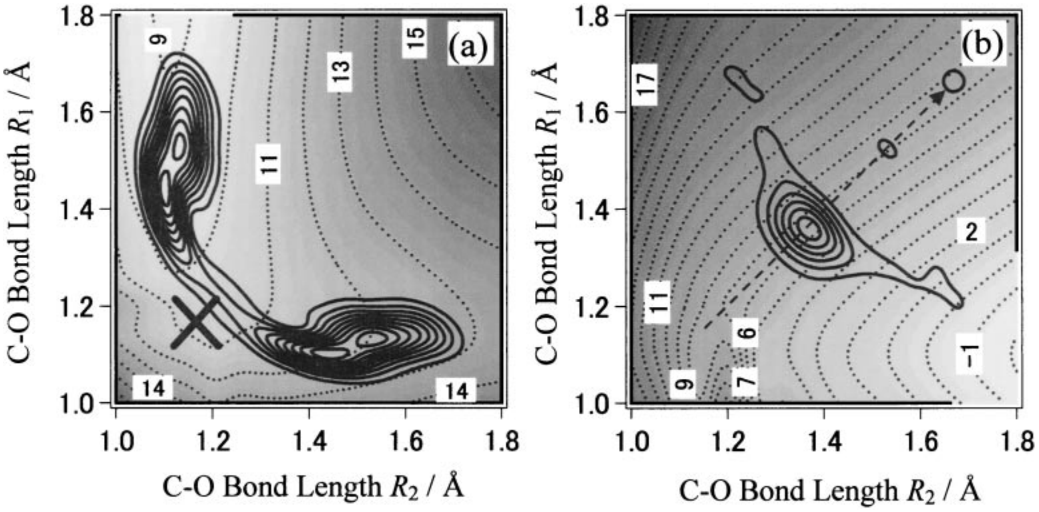

Fig. 13. Nuclear wave packet dynamics on the lowest time-dependent adiabatic potential of CO_2^{2+} in the vertical transition case. The pulse envelope of the applied field is expressed by Eq. 36: peak strength $f_0 = 0.19E_h/ea_0$ (1.3×10^{15} W cm^{-2}), pulse length $T_p = 194$ fs, and wavelength $\lambda = 795$ nm. We here assume the vertical transition case in which the wave function prepared at $t = 0$ in the lowest adiabatic state $|1\rangle$ is that of the ground vibrational state of CO_2. The central position of the initial wave function is marked with a symbol × around $R_1 = R_2 = 1.17$ Å in (a). The square of the nuclear wave functions at $t = 24.7$ fs is denoted by the solid contour lines in (a); the wave packet at $t = 96.9$ fs (solid lines) is shown in (b). The instantaneous adiabatic potentials of $|1\rangle$ at $\mathcal{E}(t = 24.7\,\text{fs}) = -0.029E_h/ea_0$ and $\mathcal{E}(t = 96.9\,\text{fs}) = 0.19E_h/ea_0$ (both are local extremes of the applied field) are shaded on a gray scale in (a) and (b), respectively; the dotted contour lines are plotted at intervals of 1 eV. As shown in (b), although the adiabatic potential can be dissociative at instantaneous moments for one of the two-body breakup channels, one-bond stretching is not greatly enhanced by the field. As denoted by a broken line with an arrow in (b), two-bond symmetric stretching is dominant. Adapted from Ref. 48.

expected that one-bond stretching is predominant. As will be shown below, however, the wave packet dynamics shows that symmetric stretching occurs as well as one-bond stretching.

The applied alternating electric field is assumed to have a near-infrared frequency $\omega = 0.0574E_h/\hbar$ ($\lambda = 795$ nm) and to have a realistic pulse envelope $f(t)$:

$$f(t) = f_0 \sin^2(\pi t/T_p) \quad \text{for } 0 \le t \le T_p, \tag{36}$$

and it is otherwise zero. To reproduce the pulse used in the experiment, we choose the following parameters: peak strength $f_0 = 0.19E_h/ea_0$ (1.3×10^{15} W cm^{-2}) and pulse length $T_p =$ 194 fs.

The geometry of CO_2^{2+} just after ionization of CO_2^+ is expected to be more or less equal to the equilibrium geometry of CO_2. The vibrational wave function of the initially prepared state of CO_2^{2+} can be expressed by the product of the wave function of the ground vibrational state of CO_2 and the ionization rates of CO_2 and CO_2^+ as functions of nuclear coordinates. Since the explicit forms of the ionization rates are unknown, we tested two cases: vertical transition and adiabatic transition. In the vertical transition case, the vibrational state of CO_2^{2+} initially prepared is the ground vibrational state of CO_2. In Fig. 13a, the center of the initial wave function is marked with a symbol × around $R_1 = R_2 = 1.17$ Å. As shown by the wave packet at $t = 24.7$ fs in Fig. 13a, a part of the wave packet propagates first toward the channels for one-bond stretching from the Franck–Condon region. The instantaneous potential at $\mathcal{E}(t = 24.7\,\text{fs}) = -0.029E_h/ea_0$ is denoted by dotted contour lines. Around $t = 45$ fs, the wave packet returns to the vicinity of $R = 1.2$ Å. The initial one-bond stretching is not an effect of the applied field; it originates from the difference in the equilibrium internuclear distance between CO_2^{2+} and CO_2.

We have proposed that the experimentally observed two-body breakup to $CO^+ + O^+$ is due to the one-bond stretching mainly determined by the shape of the field-free adiabatic potential of CO_2^{2+}. To estimate the probability of occurrence of one-bond dissociation, we set a detection window with a width of $R_2 = [0, 1.2]$ Å at $R_1 = 1.7$ Å, and we also set a window of the same width for the other bond. In a zero field, *all* of the dissociation components are detected by the two windows; the probability for one-bond dissociation channels is $P_{\text{one}} \approx 0.14$ (=total dissociation probability in this case). In the presence of the field, the probability detected by these windows is $P_{\text{one}} \approx 0.20$ (Subsequent ionization will cause sequential bond breaking as $OC^+ + O^+ \rightarrow O^+ + C^+ + O^+$[24,112]). The adiabatic potential in a field can be dissociative at instantaneous moments for one of the two-body breakup channels, as shown by the instantaneous potential $E_{z,1}(R_1, R_2, t)$ at $\mathcal{E}(t = 96.9\,\text{fs}) = 0.19E_h/ea_0$ in Fig. 13b. However, considering that the total dissociation probability is ≈0.70, one-bond stretching is not greatly enhanced by the field, as indicated by the wave packet at $t = 96.9$ fs in Fig. 13b. This is due to the disappearance of the odd order terms with $\mathcal{E}(t)$ in the cycle-averaged potential $\bar{E}_{x,1}(R_1, R_2, t)$ of CO_2^{2+}, as in the case of CO_2 [See Eq. 34]. The dynamics of the wave packet in the cycle-averaged potential is practically identical to the "raw" dynamics shown in Fig. 13.

Although the dissociation energy for symmetric stretching is as large as ≈11 eV in a zero field, symmetric two-bond stretching becomes dominant as the field envelope approaches $f(t \approx$

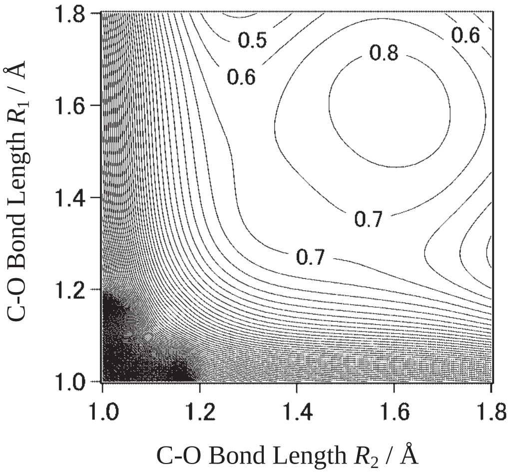

Fig. 14. Cycle-average of the lowest adiabatic potential $E_{z,1}(R_1, R_2, t)$ of CO_2^{2+}. The cycle-averaged potential is obtained by averaging $E_{z,1}(R_1, R_2, t)$ over one optical cycle around $t = 96.9$ fs near the pulse peak [$f(t = 96.9\,\mathrm{fs}) = 0.19E_h/ea_0$]. The intervals between contour lines are 0.1 eV. As the field intensity increases, the stabilization energy due to the induced dipole moment becomes large: as shown in the figure, the steepest descending slope from $R_1 = R_2 = R_e$ is formed along $R_1 = R_2$. The cycle-averaged potential is symmetric with exchange of R_1 and R_2 because of the disappearance of the odd order terms with $\mathcal{E}(t)$. Reproduced from Ref. 48.

50 fs) $= 0.1E_h/ea_0$ ($I \approx 3.5 \times 10^{14}$ W cm^{-2}); the center of the wave packet moves to a region of $R_1 = R_2$ [=1.4 Å at $t = 96.9$ fs, as shown in Fig. 13b]. The appearance of field-induced symmetric two-bond stretching can be explained by the characteristic features of $\bar{E}_{z,1}(R_1, R_2, t)$. The cycle-averaged potential $\bar{E}_{z,1}(R_1, R_2, t)$ at $t = 96.9$ fs is shown in Fig. 14. In CO_2^{2+}, the stabilization energy $-\alpha(R_1, R_2)f(t)^2/4$ due to the induced dipole moment is large around the ridge of $R_1 = R_2$ relative to the field-free dissociation energy for symmetric stretching. Consequently, at high intensities, the steepest descending slope from $R_1 = R_2 = R_e$ is formed along $R_1 = R_2$ in $\bar{E}_{z,1}(R_1, R_2, t)$, as shown in Fig. 14. The dissociation energy for the symmetric coordinate in $\bar{E}_{z,1}(R_1, R_2, t)$ is just 2.2 eV at $f(t) = 0.14E_h/ea_0$; at higher field intensities, the symmetric stretching becomes unbound. The difference between the total dissociation probability and the one-bond dissociation probability P_{one} is regarded as the probability of occurrence of field-induced symmetric two-bond dissociation, P_{sym} ($\approx$0.50).

After bond stretching in CO_2^{2+}, ionization to CO_2^{3+} occurs even at field strengths that do not ionize CO_2^{2+} around R_e (enhanced ionization).[24] As shown in Fig. 15, the potential surface of the field-free lowest adiabatic state ($^2\Pi$ in the case of linear geometry) of CO_2^{3+} has a minimum around $R_1 = R_2 = 1.35$ Å, from which a hill gently ascends to a peak around $R_1 = R_2 = 1.7$ Å with a height of 0.5 eV. In the region of $R_1 = R_2 > 1.7$ Å, the potential of CO_2^{3+} is governed by the Coulomb repulsions of the three positively charged atoms and decreases according to the formula of $5/2R_s$. If ionization to CO_2^{3+} occurs, say, around $R_1 = R_2 = 1.7$ Å, the nuclear wave packet is then at the top of the hill of CO_2^{3+}: The CO_2^{3+} created will undergo Coulomb explosions to $O^+ + C^+ + O^+$.

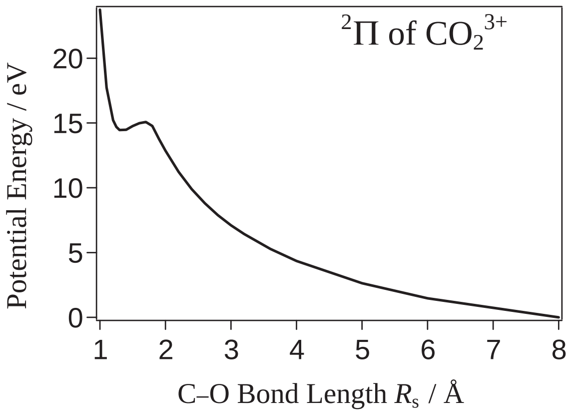

Fig. 15. Potential surface of the field-free lowest adiabatic state $^2\Pi$ of linear CO_2^{3+} as a function of symmetric C–O distance R_s ($=R_1 = R_2$). In the region of $R_s > 1.7$ Å, the potential of CO_2^{3+} is governed by the Coulomb repulsions of the three positively charged atoms $O^+ + C^+ + O^+$ and it decreases according to the Coulomb repulsion formula of $5/(2R_s)$.

In the present case, the applied filed for CO_2^{2+} is turned on at $t = 0$. We confirmed that the final structural deformation theoretically predicted is not sensitive to the choice of the time of switching from CO_2^{+} to CO_2^{2+}. When CO_2^{+} is ionized ($I < 3 \times 10^{14}$ W cm^{-2}), the light intensity is still not high enough to deform the potential of CO_2^{2+}.

We have also tested the adiabatic transition case in which CO_2^{2+} starts from its ground vibrational state. Considering that the ionization probability generally has a peak around an internuclear distance larger than the equilibrium internuclear distance, the peak of the initial vibrational wave function of CO_2^{2+} is presumably expressed by shifting the wave function of the ground vibrational state of CO_2 toward larger internuclear distances. Since the equilibrium internuclear distance of CO_2^{2+} (the calculated value being 1.22 Å) is longer than 1.17 Å of CO_2, the actual situation will be shifted from the vertical transition case toward the adiabatic transition case. Under the condition of the same pulse as that used before, the probability of going through the detection windows for one-bond stretching, P_{one}, is $\approx$0.13. This value is smaller than that in the vertical transition case. In the adiabatic transition case, one-bond stretching is purely field-induced: Initial one-bond stretching as observed in the vertical transition case does not occur. The probability of field-induced two-bond dissociation, P_{sym}, is 0.35. The ratio $P_{\mathrm{sym}}/P_{\mathrm{one}}$ is eventually only a little larger in the adiabatic transition case than in the vertical transition case where one-bond stretching initially occurs.

6.2.2.2 Correlation between Bond Angle Bending and Symmetric Stretching; We now discuss the origin of the experimentally observed bending amplitude, $\langle(2\theta)^2\rangle^{1/2} \approx 20°$, of exploding CO_2^{3+}.[24] In the case where the molecular axis is parallel to the field polarization direction, the energy shift due to the induced dipole is nearly proportional to $-R_s \cos\theta$, because field-induced charge separation occurs between the two O atoms. The induced dipole of the lowest adiabatic state that shifts the energy downward becomes smaller as the mole-

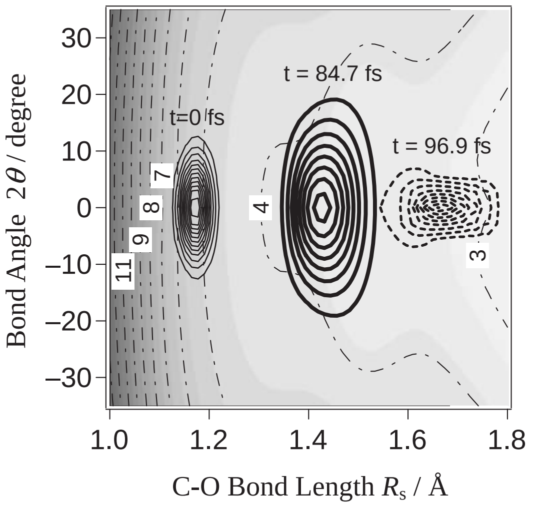

Fig. 16. Bending and stretching dynamics on the lowest time-dependent adiabatic potential of $CO_2{}^{2+}$ in the vertical transition case. The contour map denoted by dotted lines (plotted at intervals in 1 eV) is the cycle-averaged potentials of $|1\rangle$ at $t = 84.7$ fs. Snapshots of the wave packet are taken at $t = 0$ (solid lines), $t = 84.7$ fs (bold solid lines), and $t = 96.9$ fs (broken lines). In the initial stage up to ≈70 fs, the mean amplitude of bending, $\langle (2\theta)^2 \rangle$, is doubled at most (≈12°). However, the curvature of the cycle-averaged potential with θ is large at large R_s: After the wave packet passes a point of ≈1.6 Å, the amplitude of bending motion in $|1\rangle$ decreases. Adapted from Ref. 48.

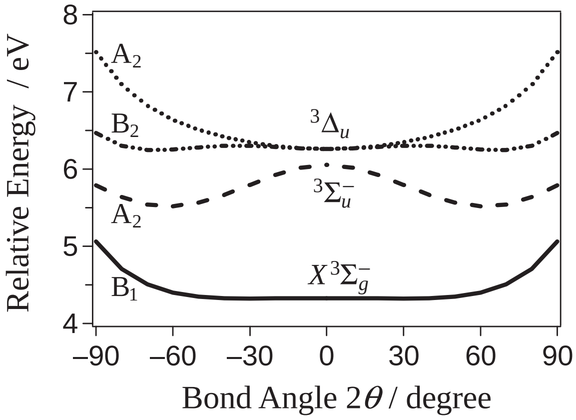

Fig. 17. Potential surfaces of the lowest four field-free triplet states of $CO_2{}^{2+}$ as a function of the bending angle 2θ at C–O distance of $R_s = R_1 = R_2 = 1.6$ Å. The four electronic states at linear geometry are assigned to $X^3\Sigma_g^-$, $^3\Sigma_u^-$, and degenerate $^3\Delta_u$ states in the ascending order of energy; the four states at a bent structure are designated by B$_1$, A$_2$, B$_2$, and A$_2$ of the C_{2v} point group, respectively. The potential of the first excited state $^3\Sigma_u^-$ has a minimum at a bent structure.

cule becomes more bent; as a result, the curvature of the potential with θ is larger in a nonzero field than in a zero field. Therefore, if the internuclear distances are fixed, a large-amplitude bending motion is unlikely to be induced by a field. In the case of a perpendicular spatial configuration, bond stretching does not occur, while bending motion is slightly induced.

To examine how the bending motion is correlated with bond stretching, we used the two-dimensional Hamiltonian constructed from the bending and symmetric stretching modes, Eq. 32. The pulse envelope in Eq. 36 was used. The calculated wave packet dynamics showed the following features.[48] The wave packet propagation on the lowest adiabatic state $|1\rangle$ of $CO_2{}^{2+}$ is shown together with the cycle-averaged potential at $t = 84.7$ fs in Fig. 16. We assumed the vertical transition case. In the initial stage up to ≈70 fs, at periodic intervals of 30–35 fs, the wave packet moves back and forth along the symmetric stretching coordinate R (between $R = 1.2$ and $R = 1.4$ Å) and repeatedly spreads and shrinks in the bond angle direction. The quasiperiodic motion originates from the fact that the potential surface of $CO_2{}^{2+}$ is shallower than that of CO_2. The cycle-averaged potential of $|1\rangle$ is rather flat with respect to the change in the bond angle 2θ for $R < 1.5$ Å. Thus, the bending amplitude 2θ is doubled at most (≈12°) from the initial value of $2\theta \approx 6°$, as shown by the snapshots of the wave packet at $t = 0$ and 84.7 fs in Fig. 16. However, the curvature of the cycle-averaged potential with θ is large at large R due to the field-induced energy $\propto -R_s \cos\theta$: As shown by the wave packet at $t = 96.9$ fs (the peak of the pulse) in Fig. 16, after the wave packet passes a point of ≈1.6 Å, the amplitude of bending motion in $|1\rangle$ decreases. The dynamics in $|1\rangle$ alone is not sufficient to explain the experimentally observed large-amplitude bending.

We have reported that field-induced nonadiabatic transition between the lowest two adiabatic states, $|1\rangle$ and $|2\rangle$, is essential for describing the experimentally observed large-amplitude bending.[48] Shown in Fig. 17 are potential surfaces of the lowest four field-free triplet states of $CO_2{}^{2+}$ as a function of the bending angle 2θ at C–O distance of $R_s = 1.6$ Å (here, the 6-311+G(d) basis set is used). The first excited triplet state in the case of linear geometry is $^3\Sigma_u^-$ at $R_s \approx 1.6$ Å, while it is $^3\Delta_u$ at $R_s \approx 1.2$ Å (at a bent structure of the C_{2v} point group; $^3\Sigma_u^-$ corresponds to A$_2$, and $^3\Delta_u$ splits into B$_2$ and A$_2$). In the region of $R_s > 1.5$ Å, the potential of the first excited state $^3\Sigma_u^-$ has a minimum at a bent structure. The difference in energy between the lowest two adiabatic states in a zero field becomes as small as one photon energy $0.057E_h$ (= 1.55 eV) in the large bond length region ($R_s > 1.6$ Å). The difference also decreases as the bending angle increases because the potential of the second lowest adiabatic state $|2\rangle$ in a zero field has a minimum at a bent structure of $2\theta \approx \pm 60°$, as shown in Fig. 17.

Thus, nonadiabatic transitions take place at internuclear distances R_s larger than ≈1.6 Å (We have estimated the maximum field-induced coupling of $\langle 1|\partial/\partial t|2\rangle$ and calculated the nonadiabatic transition probability by the Landau–Zener formula.[48]). Around $R_s \approx 1.4$–1.7 Å, the cycle-averaged potential of $|2\rangle$ near the peak of the pulse envelope (e.g., at $t \approx 92$ fs) has a minimum at $2\theta \approx \pm 12°$, which reflects the minimum of the potential of the field-free first excited state at $2\theta \approx \pm 60°$. We have shown that the component in $|2\rangle$ nonadiabatically transferred from $|1\rangle$ is therefore split into two parts toward large bending angles.[48] The mean amplitude of bending motion in $|2\rangle$ is as large as the experimental value of ≈20° at $R_s \approx 1.7$ Å (The same conclusion is drawn in the adiabatic transition case). The role of nonadiabatic transitions is crucial for bending, while the average bond distance depends only weakly on whether the wave packet propagates on $|1\rangle$ or $|2\rangle$.

Simultaneous two-bond stretching is induced by an intense field in the lowest time-dependent adiabatic state $|1\rangle$ of CO_2^{2+}, and this two-bond stretching is followed by the occurrence of a large-amplitude bending motion mainly in the second lowest adiabatic state $|2\rangle$ nonadiabatically created from $|1\rangle$ at large C–O distances of $R_s \approx 1.6$ Å by the field. We conclude that the experimentally observed bent structure of an exploding $O^+ + C^+ + O^+$ is the structure of CO_2^{2+} just before the Coulomb explosion. We also propose that the experimentally observed two-body breakup to $CO^+ + O^+$ is due to the one-bond stretching in the CO_2^{2+} stage. For an isovalent molecule with CO_2, namely, CS_2, nonsequential symmetric bond breaking accompanied by a large amplitude bending motion, as well as sequential bond breaking, has experimentally been identified.[112] The experimental data suggest that the bending deformation proceeds as the two C–S bonds stretch.

6.3 Control of Breaking of Two Identical Chemical Bonds. We have shown in a previous section that the fate of chemical bonds of a molecule in a near-infrared intense field is mainly determined by the cycle-averaged potential (in the case where the role of field-induced nonadiabatic couplings is of minor importance). It is therefore possible to control the reaction dynamics in intense fields by modifying the cycle-averaged potential. One of the most commonly used schemes is the combination of ω and 2ω fields:[114]

$$\mathcal{E}(t) = F(t)[\sin \omega t + \eta \sin(2\omega t + \delta)], \tag{37}$$

where δ and η are the relative phase and amplitude between the ω and 2ω fields, respectively, and $F(t)$ is the slowly varying field amplitude. While the average of $\mathcal{E}(t)$ over one period of $2\pi/\omega$, $\langle\mathcal{E}(t)\rangle$, is zero as in the single ω-frequency case, the cycle-average of the higher odd-order term of $\mathcal{E}(t)$ is nonzero except in the case of $\delta = 0$. For example, the leading odd-order term, $\langle\mathcal{E}^3(t)\rangle$, is

$$\begin{aligned}\langle\mathcal{E}^3(t)\rangle &= F^3(t)\langle[\sin \omega t + \eta \sin(2\omega t + \delta)]^3\rangle \\ &= -3\eta(\sin\delta)F^3(t)/4.\end{aligned} \tag{38}$$

To assess the effect of the nonzero cycle average of $\mathcal{E}^3(t)$ judiciously, we set $\langle\mathcal{E}^2(t)\rangle$ equal to that in the single ω-frequency case. By choosing the field amplitude as

$$F(t) = f(t)/\sqrt{1+\eta^2}, \tag{39}$$

we have the same $\langle\mathcal{E}^2(t)\rangle$ as that in the single ω-frequency case: $\langle\mathcal{E}^2(t)\rangle = (1+\eta^2)F^2(t)/2 = f^2(t)/2$. Thus, the difference in dynamics between the single and double frequency cases can be attributed mainly to the nonzero $\langle\mathcal{E}^3(t)\rangle$. The final form of $\langle\mathcal{E}^3(t)\rangle$ becomes

$$\langle\mathcal{E}^3(t)\rangle = -3\eta(\sin\delta)f^3(t)/4(1+\eta^2)^{3/2}. \tag{40}$$

We consider the case in which $\langle\mathcal{E}^3(t)\rangle$ is maximized: $\eta = 1/\sqrt{2}$ and $\delta = \pm\pi/2$. The amplitude $f(t)$ and the fundamental frequency ω are the same as those used in Eq. 36. The pulse of the ω and 2ω fields chosen this way is assumed to be applied to CO_2. In the vertical $CO_2 \rightarrow CO_2^{2+}$ transition case, the dissociation probability for one-bond stretching channels is $P_{\text{one}} \approx 0.60$, while the probability of field-induced two-bond dissociation, P_{sym}, is ≈ 0.40. We assumed that the wave packet propagates in the lowest adiabatic state of CO_2^{2+}. Compared to the single ω-frequency case, P_{one} increases and P_{sym} decreases. More interesting is the asymmetry of the one-bond dissociation channels $O^+ + CO^+$ (R_1 dissociation) and $CO^+ + O^+$ (R_2 dissociation) as shown in Fig. 18 by a snapshot of the wave packet at $t = 67.8$ fs for $\delta = \pi/2$. For $\delta = \pi/2$, the probability for R_1 dissociation is $P_1 \approx 0.48$ and the probability for R_2 dissociation is $P_2 \approx 0.12$. For the choice of the opposite phase, i.e., $\delta = -\pi/2$, P_1 and P_2 are interchanged with each other. As expected from the asymmetric shape of the cycle-averaged potential as shown in Fig. 18 (dotted contour lines), one of the two C–O bonds is selectively dissociated in a two-color field of ω and 2ω.

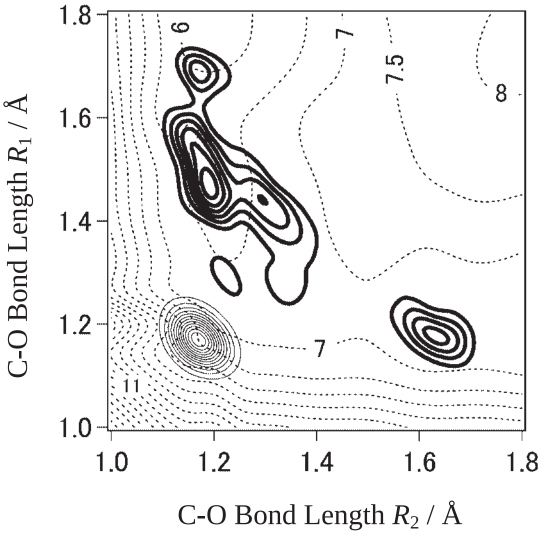

Fig. 18. Dynamics of two C–O bonds (R_1 and R_2) in the lowest adiabatic state of CO_2^{2+} in a $\omega + 2\omega$ field $\mathcal{E}(t) = f(t) \times [\sin \omega t + \eta \sin(2\omega t + \phi)]/\sqrt{1+\eta^2}$. The relative phase and amplitude between the ω and 2ω fields are chosen so that the nonzero cycle average of $\mathcal{E}^3(t)$ is maximized: $\phi = \pi/2$ and $\eta = 1/\sqrt{2}$. We assume that the initial nuclear wave packet at $t = 0$ (solid contour lines) around the equilibrium C–O distance $R_e \approx 1.2$ Å is prepared by the vertical transition from CO_2. The contour map denoted by bold solid lines shows the wave packet at $t = 67.8$ fs. The cycle-averaged potential of the lowest adiabatic state at $t = 67.8$ fs is denoted by dotted contour lines (in units of eV). The combination of the intense ω and 2ω fields induces asymmetric one-bond R_1 stretching. Adapted from Ref. 48.

7. Preferential Bond Cleavage of Ethanol in Intense Laser Fields: Importance of Field-Induced Avoided Crossing

In this section, we report the results of theoretical investigations of experimentally observed preferential cleavage of C–O and C–C bonds of ethanol C_2H_5OH in intense laser fields. In this example, for the first time, we fully evaluate essential field-induced nonadiabatic coupling elements of a polyatomic molecule by MO calculation (see Eq. 26) and solve the corresponding coupled equations for nuclear dynamics. Taking ethanol as an example, we demonstrate that field-induced nonadiabatic coupling plays a decisive role in the fate of a molecule.

Dissociative ionization of ethanol in near-infrared intense laser fields (up to $\approx 4 \times 10^{15}$ W cm^{-2}) was experimentally investigated by Itakura et al.[49] For a transform-limited intense laser pulse as short as 32 fs, fragmentation due to C–C bond cleavage is the major process, although a C–C bond and a C–O bond of neutral ethanol have nearly the same dissociation energy ($\approx$3.4 eV). This C–C bond cleavage occurs in the monocation stage. As the linear chirp rate of the pulse increases (the pulse is lengthened to $\approx$2 ps) while keeping the pulse energy constant, dissociative ionization becomes dominant over the formation of parent ions; moreover, fragment ions originating from C–O bond cleavage (such as $C_2H_5{}^+$) increase relative to those originating from C–C bond cleavage (such as CH_2OH^+).

To investigate dissociation dynamics of neutral ethanol and its cations, we use simple one-dimensional models for quantum mechanical nuclear dynamics and apply the time-dependent adiabatic state approach to the models. We here treat the cleavage of a C–C bond or a C–O bond of ethanol. Ethanol molecules are randomly oriented in a molecular beam; presumably, molecules are not aligned by a pulse as short as 2 ps. We investigate two spatial orientation configurations: (i) The spatial configuration in which the C–C axis (C–O axis) is parallel to the polarization direction of an intense laser field is expected to be the most preferable for C–C bond cleavage among all the configurations, denoted by the C–C ∥ field case; (ii) The case of the C–O axis being to parallel to the polarization direction is the most favorable for C–O bond cleavage, denoted by the C–O ∥ field case. To examine the dynamics of C–C cleavage and that of C–O cleavage, we compare the C–C ∥ field case and the C–O ∥ field case which are the most favorable for C–C bond cleavage and C–O bond cleavage, respectively. Since the bond angle between the C–C axis and C–O axis ($\approx$108°) is not far away from a right angle, the C–C and C–O bonds are nearly independent of each other in the above two configurations of an applied field. For example, the cycle-averaged dissociation energy for the C–O bond decreases only slightly in the C–C ∥ field case. Therefore, in the C–C ∥ field case, only the C–C bond length is quantum mechanically treated as a dynamical variable describing the C–C dissociation; in the C–O ∥ field case, only the C–O bond length is treated as a dynamical variable. We here focus on the experimental evidence that the C–C bond tends to be dissociated more easily than the C–O bond as the pulse length is shortened.

We follow the general procedures of (i) to (v) in Section **5**. The 6-311G(d,p) basis set (which contains a set of polarization functions on each hydrogen atom) is used in the calculation of the adiabatic potential surfaces $E(\{R\}, t)$ and wave functions $\psi(\{R\}, t)$ for ethanol and its cations. First, the molecular orbitals are optimized in the absence of an electric field by the full-optimized reaction space MCSCF method. Using the MOs optimized this way, we then calculate the adiabatic electronic energy by the first-order CI method.[100] When an instantaneous field is applied, the interaction with the field is treated as a part of the configuration interaction in the first-order CI method. In the equilibrium structure of neutral ethanol, the C–C–O–H skeleton is placed on a plane: The neutral ethanol belongs to the point group C_s. The calculated equilibrium distance of the C–C bond is 1.54 Å and that of the C–O bond is 1.43 Å.

It has been reported that a neutral ethanol molecule is ionized to a monocation around $I = 10^{14}$ W cm^{-2}.[115] The calculated cycle-averaged potential surface of neutral ethanol around this light intensity shows no significant deformation leading to C–C or C–O bond stretching. It is presumed that a neutral ethanol molecule is ionized to an ethanol monocation without any significant structural change. We thus search for reaction paths in the monocation stage of $C_2H_5OH^+$ from near the equilibrium structure of neutral ethanol. The structure of $C_2H_5OH^+$ just after ionization is therefore assumed to belong to the point group C_s, as in the equilibrium structure of a neutral ethanol molecule.

For $C_2H_5OH^+$, the calculated equilibrium distance of the C–C bond is 1.52 Å and that of the C–O bond is 1.55 Å. In the C–C ∥ field case, the C–O internuclear distance is nearly constant, while the C–C bond is stretched by a laser field; vice versa in the C–O ∥ field case. In the C–C ∥ field case, we therefore fix the C–O bond distance at the calculated value of its equilibrium distance; in the C–O ∥ field case, the C–C bond distance is fixed at its equilibrium distance. We also fix the C–C–O angle at its calculated equilibrium value of 107.6°. The positions of hydrogen atoms are optimized at different C–C (or C–O) bond lengths so that the field-free ground state energy is minimized. The symmetry of C_s is not broken by a nonzero field because the polarization direction of the applied field is on the symmetry plane both in the C–C ∥ field and C–O ∥ field cases. The ground electronic state of $C_2H_5OH^+$ has A'' symmetry of the point group C_s.

The potentials of the lowest four A''-symmetry time-dependent adiabatic states of $C_2H_5OH^+$ in the C–C ∥ field case are shown in Fig. 19 as a function of the C–C bond distance $R_{\text{C–C}}$: (a) $\mathcal{E}(t) = -0.1E_h/ea_0$, (b) $\mathcal{E}(t) = 0$, and (c) $\mathcal{E}(t) = 0.1E_h/ea_0$. The value of $\mathcal{E}(t)$ is chosen to be positive when the field vector points from the end carbon to the middle carbon atom. Compared to the field-free case shown in Fig. 19b, the potentials become more distorted as the field strength approaches $|\mathcal{E}(t)| = 0.1E_h/ea_0$. At $f(t) = 0.1E_h/ea_0$, the cycle-averaged potential ascends by 0.7 eV as the C–C bond length increases from $R_{\text{C–C}} = 1.55$ Å to 2.2 Å and it descends in the region of $R_{\text{C–C}} > 2.2$ Å; it is not completely dissociative. However, field-induced avoided crossings occur in a range not far away from the equilibrium C–C distance when $\mathcal{E}(t)$ is negative; at $\mathcal{E}(t) = -0.1E_h/ea_0$, there exists a crossing around $R_{\text{C–C}}$ of 2 Å, as shown in Fig. 19a. In the ground electronic state, the CH_2OH group is positively charged. The change in the populations of natural orbitals upon ionization from C_2H_5OH to $C_2H_5OH^+$ indicates that an electron is removed out of a nonbonding electron pair localized near the oxygen atom. For $\mathcal{E}(t) < 0$, the electrostatic energy of the lowest adiabatic state hence increases in the region of $R_{\text{C–C}} < 2$ Å as $|\mathcal{E}(t)|$ increases; on the other hand, the electrostatic energies of $CH_3{}^+$-character excited states descend. This is the reason why field-induced avoided crossings between the CH_2OH^+-dominated ground state and $CH_3{}^+$-dominated excited states occur at relatively small $R_{\text{C–C}}$. For $\mathcal{E}(t) > 0$, as well as CH_2OH^+-dominated excited states, the electrostatic energy of the lowest adiabatic state decreases as $\mathcal{E}(t)$ increases. As a result, for $\mathcal{E}(t) > 0$, field-induced avoided crossings between the lowest adiabatic

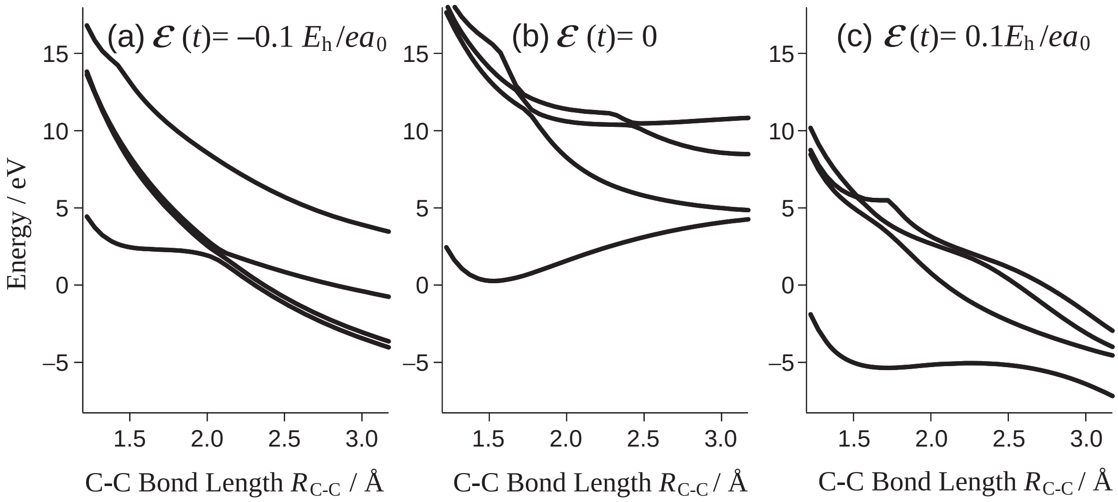

Fig. 19. Adiabatic potentials of lowest four A''-symmetry time-dependent adiabatic states of $C_2H_5OH^+$ in the C–C $\parallel$ field case as a function of the C–C bond length $R_{C\text{–}C}$. The positions of hydrogen atoms are optimized at different C–C bond lengths under the point group C_s so that the field-free ground state energy is minimized. The instantaneous electric field strength in each panel is chosen as follows: (a) $\mathcal{E}(t) = -0.1E_h/ea_0$, (b) $\mathcal{E}(t) = 0$, and (c) $\mathcal{E}(t) = 0.1E_h/ea_0$. The value of $\mathcal{E}(t)$ is chosen to be positive when the field vector points from the end carbon to the middle carbon atom. Field-induced avoided level crossings occur in a range not far away from the equilibrium C–C distance ($\approx$1.5 Å) when $\mathcal{E}(t)$ is negative; the lowest three adiabatic states cross each other around $R_{C\text{–}C} = 2.0$ Å at $\mathcal{E}(t) = -0.1E_h/ea_0$, as shown in (a).

state and higher adiabatic states occur at relatively large $R_{C\text{–}C}$, as shown in Fig. 19c. The crossing nature at a negative field is thus different from that at a positive field. In what follows, we would like to show that nonadiabatic transitions due to field-induced crossing during the period of $\mathcal{E}(t) < 0$ trigger C–C dissociation.

We use the following one-dimensional kinetic energy operator for C–C bond dissociation:

$$\hat{T}_{C\text{–}C} = -\frac{1}{2}\left(\frac{1}{m_{CH_3}} + \frac{1}{m_{CH_2OH}}\right)\frac{\partial^2}{\partial R_{C\text{–}C}^2}, \tag{41}$$

where m_{CH_3} is the mass of the CH_3 group and m_{CH_2OH} is the mass of the CH_2OH group. It may be more rigorous to use the C–C axis component of the difference vector between the center of mass of CH_2OH and that of CH_3, $R_{CH_3\text{–}CH_2OH}$. The use of Eq. 41 is justified by the fact that the difference between $R_{CH_3\text{–}CH_2OH}$ and $R_{C\text{–}C}$ is nearly constant. The coupled equations of motion for the nuclear wave functions $\{\chi_j(R_{C\text{–}C}, t)\}$ associated with time-dependent adiabatic states are constructed in terms of the kinetic energy operator of Eq. 41, time-dependent adiabatic potentials, and field-induced nonadiabatic couplings such as $\langle 1|\partial/\partial t|2\rangle$. The value of the field-induced coupling between two adiabatic states generally peaks at the temporal and spatial point where the two states come closest to each other in energy. We here truncate the coupled equations of motion by restricting the participating time-dependent adiabatic states to the lowest three states.

We solve the coupled equations of motion in the case of near-infrared intense fields. For the pulse envelope, we employed Eq. 36 with the following parameters: peak strength $f_0 = 0.12E_h/ea_0$ (5.0×10^{14} W cm^{-2}) and pulse length $T_p =$ 75 fs; frequency $\omega = 0.0574E_h/\hbar$ ($\lambda = 795$ nm). As an initial state, we use the lowest vibrational state of the field-free ground electronic state of $C_2H_5OH^+$ or that of C_2H_5OH. Since these two initial states lead to nearly the same result, we here present the results in the former case. The equilibrium structure of $C_2H_5OH^+$ is nearly the same as that of C_2H_5OH (for which the calculated equilibrium distance of the C–C bond is 1.54 Å and that of the C–O bond is 1.43 Å).

The field-induced nuclear dynamics for the lowest three adiabatic states, i.e., $\chi_1(R_{C\text{–}C}, t)$, $\chi_2(R_{C\text{–}C}, t)$, and $\chi_3(R_{C\text{–}C}, t)$, are shown in Fig. 20. As was expected, the nuclear wave packet $\chi_1(R_{C\text{–}C}, t)$ ramifies to the upper adiabatic states at $R_{C\text{–}C} \approx$ 1.7 Å owing to field-induced nonadiabatic transitions near the pulse peak. The distance of $R_{C\text{–}C} \approx 1.8$ Å is nearly equal to the location of field-induced avoided crossing at the negative peak value of $\mathcal{E}(t) = -0.12E_h/ea_0$. Dissociation proceeds through transitions to the upper adiabatic states because the cycle-averaged potentials of the upper adiabatic states are dissociative. Field-induced nonadiabatic transitions at $R_{C\text{–}C} \approx 1.7$ Å occur only when $\mathcal{E}(t)$ is negative. In the present case, the total probability of C–C bond cleavage, $P_{C\text{–}C}$, is 0.15. Without the nonadiabatic couplings such as $\langle 1|\partial/\partial t|2\rangle$, the dissociation probability $P_{C\text{–}C}$ is drastically reduced to 1.7×10^{-6}. This fact again indicates the importance of field-induced nonadiabatic transitions occurring in the vicinity of points of field-induced avoided crossings.

In Fig. 21, we also present the potential surfaces of time-dependent adiabatic states in the C–O $\parallel$ field case. We use the effective one-dimensional kinetic energy operator $\hat{T}_{C\text{–}O}$ to calculate wave packet propagation for C–O bond dissociation:

$$\hat{T}_{C\text{–}O} = -\frac{1}{2}\left(\frac{1}{m_{CH_3CH_2}} + \frac{1}{m_{OH}}\right)\frac{\partial^2}{\partial R_{C\text{–}O}^2}. \tag{42}$$

We solve the coupled equations of motion for the same applied field as in the C–C $\parallel$ field case of Fig. 20. The field-induced nuclear dynamics for the lowest three adiabatic states, i.e., $\chi_1(R_{C\text{–}O}, t)$, $\chi_2(R_{C\text{–}O}, t)$, and $\chi_3(R_{C\text{–}O}, t)$, are shown in Fig. 22

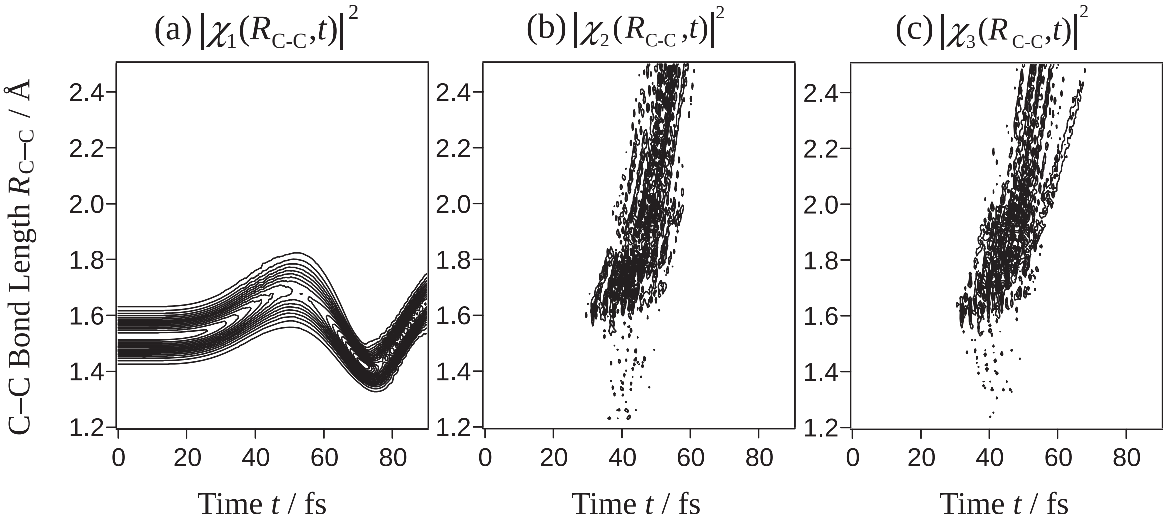

Fig. 20. C–C bond wave packets for the lowest three A''-symmetry adiabatic states $|1\rangle$, $|2\rangle$, and $|3\rangle$ in a near-infrared intense field of $\omega = 0.0574E_h/\hbar$ ($\lambda = 795$ nm): (a) $|\chi_1(R_{\text{C–C}},t)|^2$, (b) $|\chi_2(R_{\text{C–C}},t)|^2$, and (c) $|\chi_3(R_{\text{C–C}},t)|^2$. The pulse envelope has the following parameters: peak strength $f_0 = 0.12E_h/\hbar$ (5.0×10^{14} W cm^{-2}) and pulse length $T_p = 75$ fs. The initial state is the lowest vibrational state of the field-free ground electronic state of $C_2H_5OH^+$. The nuclear wave packet $\chi_1(R_{\text{C–C}},t)$ ramifies to the upper adiabatic states at $R_{\text{C–C}} \approx 1.8$ Å because of field-induced nonadiabatic transitions near the pulse peak. Field-induced nonadiabatic transitions at $R_{\text{C–C}} \approx 1.8$ Å occur only when $\mathcal{E}(t)$ is negative (i.e., when field-induced avoided crossings occur). Once transferred to the upper adiabatic states, dissociation is promoted because the cycle-averaged potentials of the upper adiabatic states are dissociative.

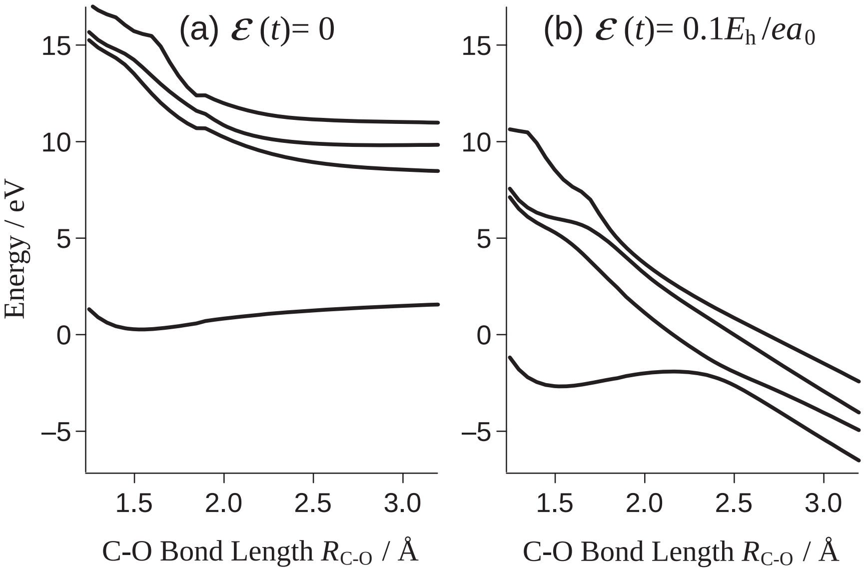

Fig. 21. Adiabatic potentials of lowest four A''-symmetry time-dependent adiabatic states of $C_2H_5OH^+$ in the C–O ∥ field case as a function of the C–O bond length $R_{\text{C–O}}$: (a) $\mathcal{E}(t) = 0$ and (b) $\mathcal{E}(t) = 0.1E_h/ea_0$. The value of $\mathcal{E}(t)$ is chosen to be positive when the field vector points from the middle carbon atom to the oxygen atom. In comparison with the C–C ∥ field case, field-induced avoided crossings occur in a range far away from the equilibrium C–O distance ($\approx$1.5 Å) when $\mathcal{E}(t)$ is positive; the lowest two adiabatic states cross each other around $R_{\text{C–O}} = 2.4$ Å at $\mathcal{E}(t) = 0.1E_h/ea_0$, as shown in (b).

(The lowest three adiabatic states are coupled.). The calculated probability of C–O cleavage, $P_{\text{C–O}}$, is 0.074 ($P_{\text{C–O}}$ decrease to $\approx$0.0018 in the absence of nonadiabatic couplings). Although the packet in the lowest time-dependent adiabatic state $|1\rangle$ reaches a region of large $R_{\text{C–O}} > 1.8$ Å (see Fig. 22a), nonadiabatic transitions to the upper adiabatic states are not so greatly enhanced as in the C–C ∥ field case. Note that the zero-field potential of the lowest adiabatic state with respect to the C–O length $R_{\text{C–O}}$ is, as shown in Fig. 21a, rather flat in comparison with the C–C ∥ field case. For a long pulse such as $T_p = 200$ fs, the dominant dissociation pathway in the C–O ∥ field case is the adiabatic channel through the shallow cycle-averaged potential surface of the lowest adiabatic state $|1\rangle$ and it is not due to field-induced nonadiabatic couplings as in the cases of $T_p < 100$ fs.

As the pulse length becomes shorter, the ratio $P_{\text{C–O}}/P_{\text{C–C}}$

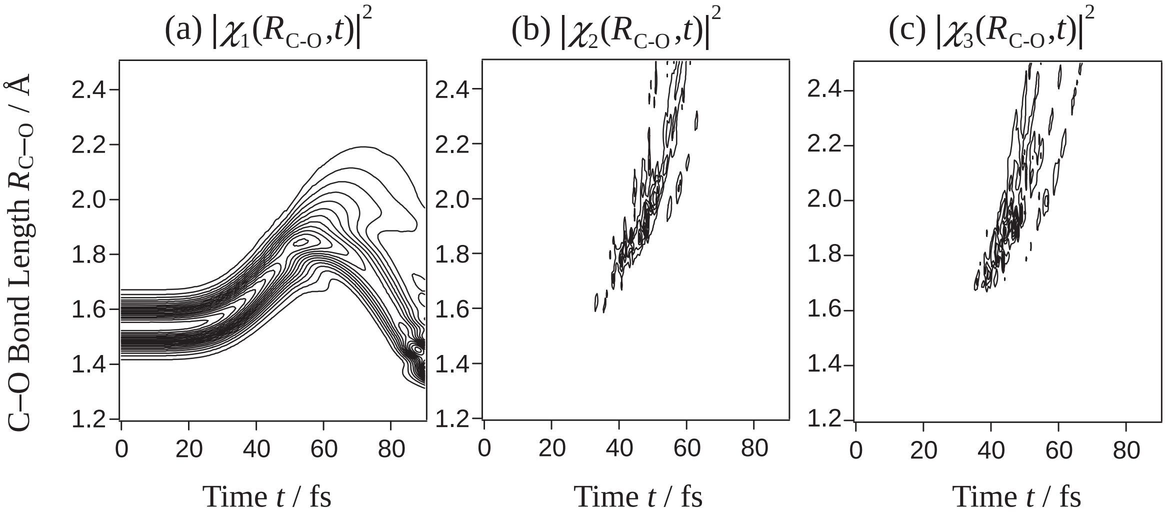

Fig. 22. C–O bond wave packets for the lowest three A''-symmetry adiabatic states $|1\rangle$, $|2\rangle$, and $|3\rangle$ in a near-infrared intense field of $\omega = 0.0574E_h/\hbar$ ($\lambda = 795$ nm): (a) $|\chi_1(R_{\text{C–O}},t)|^2$, (b) $|\chi_2(R_{\text{C–O}},t)|^2$, and (c) $|\chi_3(R_{\text{C–O}},t)|^2$. The applied pulse is the same as in the case of Fig. 20. The initial state is the lowest vibrational state of the field-free ground electronic state of $C_2H_5OH^+$. Although the packet in the lowest time-dependent adiabatic state reaches a region of large $R_{\text{C–O}} > 1.8$ Å (see Fig. 22a), nonadiabatic transitions to the upper adiabatic states are not so greatly enhanced as in the C–C ∥ field case.

becomes smaller; e.g., $P_{\text{C–O}}/P_{\text{C–C}} \approx 0.2$ for the pulse of $T_p = 50$ fs. This tendency is in accordance with the experimental results.[49] In the C–C ∥ field case, nonadiabatic transitions to upper dissociative adiabatic states occur even if the pulse length is as short as 30 fs. On the other hand, in the C–O ∥ field case, the nuclear wave packet needs longer time to reach a critical region for C–O dissociation. As shown in Fig. 21b, the location of field-induced crossing in the C–O ∥ field case is far away from the equilibrium C–O distance in comparison with the C–C ∥ field case. In the C–O ∥ field case, it takes longer time for a wave packet to reach the region of avoided crossing where nonadiabatic transitions to upper dissociative adiabatic states occur. For pulses as short as 50 fs, the C–O dissociation process is essentially adiabatic: Once the pulse has fully decayed, the electronic state is the ground electronic state and hence C–O bond cleavage is unlikely to occur. We have also analyzed the nuclear dynamics on A'-adiabatic states and come to the same conclusion that C–C bond cleavage becomes dominant as the pulse length is shortened.

The calculated dissociation probability is independent of the sign of the linear chirp rate, as observed in the experiment.[49]

8. Concluding Remarks

In this paper, we first reviewed the results of theoretical investigations of electronic and nuclear dynamics of H_2^+ and H_2 in near-infrared intense fields to support a theoretical approach for dealing with dynamics of polyatomic molecules in intense fields, namely, the time-dependent adiabatic state approach. Electronic dynamics and subsequent nuclear dynamics of H_2^+ in a near-infrared, intense laser field are examined with accurate evaluations of the electronic and nuclear wave packet by the dual transformation method we have developed to deal with the dynamics in Coulombic potentials. Using "field-following" time-dependent adiabatic states defined as eigenfunctions of the "instantaneous" electronic Hamiltonian, we clarified the dynamics of the bound electron, ionization processes, Coulomb explosion processes, and nuclear vibration of H_2^+ in an intense laser field ($I > 10^{13}$ W cm^{-2} and $\lambda > 700$ nm). The present analysis of H_2^+ indicates that the electronic and nuclear dynamics of molecules in intense fields can be described by using the potential surfaces of time-dependent adiabatic states and the nonadiabatic coupling elements between those states. By population analysis of time-dependent adiabatic states, the "doorway state" to ionization is identified and the mechanism of enhanced ionization is clarified.

According to the results of accurate evaluation of two-electron dynamics of H_2 in an intense laser field ($I \approx 10^{14}$ W cm^{-2} and $\lambda = 760$ nm), an ionic component characterized by the electronic structure H^+H^- or H^-H^+ is created owing to laser-induced electron transfer from the ascending well to the descending well. Ionization proceeds via a formation of an electron pair localized in the *descending* well, in contrast to the H_2^+ case, where the electron is ejected most easily from the *ascending* well. As R increases, while the population of H^-H^+ decreases, a pure ionic state H^-H^+ becomes more unstable in an intense field, because the attractive force that the distant H^+ exerts on the electrons of H^- is weaker. As a result, ionization is enhanced at the critical range of $R_c = 4a_0$–$6a_0$. It is concluded that H^+H^- and H^-H^+ are the main doorway states to ionization and that these localized ionic states are identified as time-dependent adiabatic states constructed from three essential electronic states, X, B, and EF.[39]

The above description of dynamics in terms of "field-following" time-dependent adiabatic states, i.e., the time-dependent adiabatic state approach of a multichannel framework, is applicable to *polyatomic* molecules in intense laser fields with the help of ab initio MO methods. The time-dependent adiabatic potentials and field-induced nonadiabatic coupling elements calculated by MO methods are used to evaluate the nuclear dynamics until the next ionization process. We have applied the approach to reveal characteristic features of molecular dynamics in intense fields. The results of theoretical investigation of structural deformations of CO_2 and its cations in a near-infrared intense field showed that the experimentally observed structure of CO_2^{3+} ($R_s \approx 1.7$ Å and $2\theta \approx 20°$) just before Coulomb explosions originates from the structural deformation of CO_2^{2+}. It is concluded that the experimentally observed structure deformations occur when the molecular axis is parallel to the polarization direction of the field. In the CO_2 and CO_2^+ stages, ionization occurs before the field intensity becomes high enough to deform the molecule. Although the dissociation energy of CO_2^{2+} in a zero field is $\approx$11 eV in the case of symmetric two-bond stretching and it is $\approx$1 eV in the case of one-bond stretching, simultaneous two-bond stretching occurs in an intense field as well as one-bond stretching. Two-bond stretching is induced by an intense field in the lowest time-dependent adiabatic state $|1\rangle$ of CO_2^{2+}, and this two-bond stretching is followed by the occurrence of a large-amplitude bending motion mainly in the second lowest adiabatic state $|2\rangle$ nonadiabatically created from $|1\rangle$ at large C–O distances of $R_s \approx 1.6$ Å by the field. The occurrence of two-bond stretching in near-infrared fields can be illustrated by using the cycle-averaged potential. We also proposed that the experimentally observed two-body breakup to $CO^+ + O^+$ is due to the one-bond stretching in the CO_2^{2+} stage.

We also applied the time-dependent adiabatic state approach to investigate dissociative ionization of ethanol. We employed two one-dimensional models in which the C–C axis or the C–O axis is parallel to the polarization direction of an applied laser field (denoted by the C–C ∥ field case and the C–O ∥ field case, respectively) to compare the probability of C–C bond cleavage, $P_{C\text{–}C}$, and that of C–O bond cleavage, $P_{C\text{–}O}$. We theoretically revealed that dissociation proceeds in the monocation stage of C_2H_5OH. As the pulse length becomes shorter, the calculated ratio $P_{C\text{–}O}/P_{C\text{–}C}$ becomes smaller: e.g., $P_{C\text{–}O}/P_{C\text{–}C} \approx 0.2$ for a pulse of $T_p = 50$ fs. This tendency is in accordance with the experimental results that the fragmentation to CH_2OH^+ and CH_3 due to C–C bond cleavage is the major fragmentation process for a transform-limited 32-fs pulse in the experiment. In the C–C ∥ field case, nonadiabatic transitions to upper dissociative adiabatic states occur even if the pulse length is as short as 30 fs. On the other hand, the location of field-induced crossing in the C–O ∥ field case is far away from the equilibrium $R_{C\text{–}O}$ distance in comparison with the C–C ∥ field case. In the C–O ∥ field case, it takes a longer time for a wave packet to reach the region of avoided crossing where nonadiabatic transitions to upper dissociative adiabatic states occur. The present example of ethanol is the first accurate assessment of the effect of field-induced nonadiabatic transition in a polyatomic molecule.

The time-dependent adiabatic state approach has the advantage that only a small number of *low-lying* adiabatic states that can be efficiently calculated by MO methods are required to describe the electronic and nuclear dynamics of a molecule in intense laser fields. It should be pointed out that many field-free excited states are involved even in the lowest adiabatic state $|1\rangle$. Practical advantages of the time-dependent adiabatic state approach over the Floquet method (dressed state method)[94] in describing the dynamics of polyatomic molecules have been summarized in Section **5**.

Hankin et al. have investigated ionization of 23 organic molecules caused by their interaction with intense 40 fs, 800 nm pulses.[115] All molecules reach saturated ionization at higher intensities than would be expected for atoms of the same ionization potential. Dependence of the ionization rate on the alignment of the molecule with the laser field is ruled out as the cause of the high saturation intensities. For many organic molecules, saturated ionization occurs at higher intensity than expected. Later, Lezius et al. proposed a mechanism that "nonadiabatic multielectron dynamics" is responsible for higher saturated intensities for organic molecules.[21] They emphasized that the adiabatic assumption fails in the case of a large molecule where the size of the molecule (the spatial extent of delocalized electrons) exceeds the path lengths of field-induced electron motion; i.e., the time scale of electron motion inside the binding potential well is longer than the laser period, driving electron dynamics inside the molecule. This is also emphasized in our results of the field-induced intramolecular electron dynamics in H_2^+ or H_2 at *large* internuclear distances. The popular Keldysh parameter, often used as a diagnostic of tunneling behavior, becomes meaningless when electron dynamics inside the molecule become important. They also suggested that collective multielectron behavior should start to dominate their strong-field response as systems increase further in size. The energy poured into a molecule by a laser field can be shared by the dynamic polarization of all electrons. The existence of various fragmentation pathways in C_{60} as well as high saturation intensities for its ionization[116] support the idea that nonadiabatic multielectron dynamics plays a significant role in ionization, fragmentation, and energetics of a molecule in an intense laser field.

Elucidation of nonadiabatic multielectron dynamics is one of the most important problems we should solve in the next decades. Since the early days of nonperturbative ionization of atoms in intense laser fields, several versions based on the evaluation of the *S*-matrix transition amplitude[117] have been introduced; these are together known as the Keldysh–Faisal–Reiss (KFR) theory.[15,118,119] The KFR theory can be applied to a regime of nonadiabatic ionization as well as the tunneling regime of $\gamma < 1$. However, in the conventional KFR theory, only the leading terms of systematic series expansions for ionization processes have been used. Electron dynamics prior to ionization has not been explicitly taken into account. To clarify ionization processes such as enhanced ionization and to examine the competition between ionization and fragmentation, one must calculate the ionization probability of a time-evolving electronic state as a function of internuclear distances. To that end, we have incorporated the present time-dependent adiabatic state approach (i.e., a wave packet consisting of bound electronic states) into a framework based on *S*-matrix scattering theory.[120] The time-evolution of the wave packet composed of only bound states is determined by the time-dependent Schrödinger equation so that the effects of both Coulomb field and radiation field on the bound electron(s) can be reproduced. This type of time-evolving wave packet can describe intramolecular nonadiabatic multielectron dynamics of a molecule in intense laser fields. By completion of this project, the semi-empirical procedure for switching to cation stages will be replaced by an ab initio treatment, and then the time-dependent adiabatic state approach becomes a truly unified approach to describe electronic and nuclear dynamics of polyatomic molecules in intense laser fields. The role of time-dependent adiabatic states as doorway states to ionization will be fully clarified even in the case of polyatomic molecules. We have also developed a multi-configurational time-dependent Hartree–Fock method to describe multielectron dynamics of a molecule in intense laser fields.[121]

In Section **6.3**, we theoretically demonstrated that one of two C–O bonds could be selectively dissociated by a *nonresonant* two-color field of ω and 2ω. This example proves that the concept of the cycle-averaged potential is also useful for designing schemes to control molecular dynamics, e.g., cleavage of chemical bonds, in intense fields. A foreseeable application of the present time-dependent adiabatic state approach is simulation of the control of more complex processes, such as chemical reactions of polyatomic molecules in intense fields.[22,23,122] The dynamics of CO_2 presented in this paper suggests that control of chemical reactions in intense fields should be carried out in a manner that Coulomb explosions occurring at large internuclear distances are avoided. It is of great importance to examine how a desired reaction product is selectively created by control of field-induced nonadiabatic transitions which are ubiquitous in the case of polyatomic molecules as was shown by an example of C_2H_5OH in Section **7**. Field-induced nonadiabatic coupling designed by optimal control schemes, which is also intended for manipulating nonadiabatic multielectron processes, would become a promising "tool" to steer processes inherent in a molecule such as intramolecular vibrational energy redistribution (IVR) and nonradiative transitions (electronic relaxation due to nuclear motion).

This work was supported in part by Grant-in-Aids for scientific research (Nos. 12640484, 14540463, and 16350001) and a Grant-in-Aid for scientific research on priority areas, "Control of Molecules in Intense Laser Fields" (Area No. 419), from the Ministry of Education, Culture, Sports, Science and Technology, Japan. H. K. wishes to express his gratitude for the cooperation obtained from Professors Y. Fujimura, S. Koseki, N. Shimakura, Y. Ohtsuki, and Dr. I. Kawata. Thanks are due to Professors K. Yamanouchi, A. Hishikawa, F. Kannari, A. D. Bandrauk, T. T. Nguyen-Dang, D. Mathur, S. H. Lin, S. L. Chin, F. H. M. Faisal, A. Becker, J. Manz, Y. Kayanuma, and R. Itakura for their valuable discussions.

References

1 K. Yamanouchi, *Science* **2002**, *295*, 1659.

2 *Laser Control and Manipulation of Molecules*, ed. by A. D. Bandrauk, R. J. Gordon, Y. Fujimura, Oxford, Oxford, **2002**, ACS Symposium Series Vol. 821.

3 M. D. Perry, G. A. Mourou, *Science* **1994**, *64*, 917; G. A. Mourou, C. P. J. Barty, M. D. Perry, *Phys. Today* **1998**, *51*, 22; K. Yamakawa, M. Aoyama, T. Kase, Y. Akahane, H. Takuma, *Opt. Lett.* **1998**, *23*, 1468.

4 S. L. Chin, F. Yergeau, P. Lavigne, *J. Phys. B: At. Mol. Phys.* **1985**, *18*, L213; N. B. Delone, V. P. Krainov, *Multiphoton Processes in Atoms*, Springer, Berlin, **1994**.

5 A. McPherson, G. Gibson, H. Jara, U. Johann, I. A. McIntyre, K. Boyer, C. K. Rhodes, *J. Opt. Soc. Am. B* **1987**, *4*, 595; X. F. Li, A. L'Huillier, M. Ferray, L. A. Lompré, G. Mainfray, *Phys. Rev. A* **1989**, *39*, 5751; E. A. Gibson, A. Paul, N. Wagner, R. Tobey, I. P. Christov, D. T. Attwood, E. Gullikson, A. Aquila, M. M. Murnane, H. C. Kapteyn, *Science* **2003**, *302*, 95; V. Tosa, E. Takahashi, Y. Nabekawa, K. Midorikawa, *Phys. Rev. A* **2003**, *67*, 063817; M. Lewenstein, P. Balcou, M. Y. Ivanov, A. L'Huillier, P. B. Corkum, *Phys. Rev. A* **1994**, *49*, 2117.

6 M. Hentschel, R. Kienberger, C. Spielmann, G. A. Reider, N. Milosevic, T. Brabec, P. Corkum, U. Heinzmanns, M. Dreschers, F. Krausz, *Nature* **2001**, *414*, 509; M. Drescher, M. Hentschel, R. Kienberger, M. Uiberacker, V. Yakovlev, A. Scrinzi, T. Westerwalbesloh, U. Kleineberg, U. Heinzmann, F. Krausz, *Nature* **2002**, *419*, 803; A. Baltuška, T. Udem, M. Uiberacker, M. Hentschel, E. Goulielmakis, C. Gohle, R. Holzwarth, V. S. Yakovlev, A. Scrinzi, T. W. Hansch, F. Krausz, *Nature* **2003**, *421*, 611; T. Sekikawa, A. Kosuge, T. Kanai, S. Watanabe, *Nature* **2004**, *432*, 605.

7 C. Cornaggia, J. Lavancier, D. Normand, J. Morellec, P. Agostini, J. P. Chambaret, A. Antonetti, *Phys. Rev. A* **1991**, *44*, 4499; J. H. Posthumus, K. Codling, L. J. Frasinski, M. R. Thompson, *Laser Phys.* **1997**, *7*, 813.

8 J. P. Nibarger, S. V. Menon, G. N. Gibson, *Phys. Rev. A* **2001**, *63*, 053406.

9 G. N. Gibson, M. Li, C. Guo, J. P. Nibarger, *Phys. Rev. A* **1998**, *58*, 4723.

10 a) B. Friedrich, D. Herschbach, *Phys. Rev. Lett.* **1995**, *74*, 4623. b) H. Sakai, C. P. Safvan, J. J. Larsen, K. M. Hilligsøe, K. Hald, H. Stapelfeldt, *J. Chem. Phys.* **1999**, *110*, 10235. c) J. J. Larsen, H. Sakai, C. P. Safvan, I. Wendt-Larsen, H. Stapelfeldt, *J. Chem. Phys.* **1999**, *111*, 7774. d) M. Schmidt, S. Dobosz, P. Meynadier, P. D'Oliveira, D. Normand, E. Charron, A. Suzor-Weiner, *Phys. Rev. A* **1999**, *60*, 4706.

11 P. Nibarger, M. Li, S. V. Menon, G. N. Gibson, *Phys. Rev. Lett.* **1999**, *83*, 4975.

12 L. Quaglia, C. Cornaggia, *Phys. Rev. Lett.* **2000**, *84*, 4565.

13 J. H. Posthumus, A. J. Giles, M. R. Thompson, K. Codling, *J. Phys. B: At. Mol. Opt. Phys.* **1996**, *29*, 5811; L. J. Frasinski, K. Codling, P. Hatherly, *Phys. Rev. Lett.* **1989**, *58*, 2424; K. Codling, L. J. Frasinski, *J. Phys. B: At. Mol. Opt. Phys.* **1993**, *26*, 783; E. Constant, H. Stapelfelt, P. B. Corkum, *Phys. Rev. Lett.* **1996**, *76*, 4140.

14 C. Cornaggia, J. Lavancier, D. Normand, J. Morellec, H. X. Liu, *Phys. Rev. A* **1990**, *42*, 5464; M. Schmidt, D. Normand, C. Cornaggia, *Phys. Rev. A* **1994**, *50*, 5037.

15 L. V. Keldysh, *Sov. Phys. JETP* **1965**, *20*, 1307.

16 S. August, D. D. Meyerhofer, D. Strickland, S. L. Chin, *J. Opt. Soc. Am. B* **1991**, *8*, 858; F. A. Ilkov, J. E. Decker, S. L. Chin, *J. Phys. B: At., Mol. Opt. Phys.* **1992**, *25*, 4005.

17 M. V. Ammosov, N. B. Delone, V. P. Krainov, *Sov. Phys. JETP* **1986**, *64*, 1191.

18 V. P. Krainov, H. R. Reiss, B. M. Smirnov, *Radiative Processes in Atomic Physics*, Wiley, New York, **1997**.

19 I. Kawata, H. Kono, Y. Fujimura, *J. Chem. Phys.* **1998**, *110*, 11152; I. Kawata, H. Kono, Y. Fujimura, *Chem. Phys. Lett.* **1998**, *289*, 546.

20 K. Harumiya, I. Kawata, H. Kono, Y. Fujimura, *J. Chem. Phys.* **2000**, *113*, 8953.

21 M. Lezius, V. Blanchet, M. Y. Ivanov, A. Stolow, *J. Chem. Phys.* **2002**, *117*, 1575.

22 A. Assion, T. Baumert, M. Bergt, T. Brixner, B. Kiefer, V. Seyfried, M. Strehle, G. Gerber, *Science* **1998**, *282*, 919; T. Brixner, G. Gerber, *Chem. Phys. Phys. Chem.* **2003**, *48*, 418.

23 J. R. Levis, G. M. Menkir, H. Rabitz, *Science* **2001**,

292, 709.

24 A. Hishikawa, A. Iwamae, K. Yamanouchi, *Phys. Rev. Lett.* **1999**, *83*, 1127.

25 M. J. DeWitt, R. J. Levis, *J. Chem. Phys.* **1998**, *108*, 7739.

26 P. B. Corkum, *Phys. Rev. Lett.* **1993**, *71*, 1994.

27 a) T. Zuo, S. Chelkowski, A. D. Bandrauk, *Phys. Rev. A* **1992**, *46*, R5342; T. Zuo, A. D. Bandrauk, *Phys. Rev. A* **1995**, *52*, 2511; A. D. Bandrauk, *Comments At. Mol. Phys. D* **1999**, *1*, 97. b) L. Y. Peng, J. F. McCann, D. Dundas, K. T. Taylor, I. D. Williams, *J. Chem. Phys.* **2004**, *120*, 10046. c) T. Seidemann, M. Y. Ivanov, P. B. Corkum, *Phys. Rev. Lett.* **1995**, *75*, 2819.

28 J. H. Posthumus, A. J. Giles, M. R. Thompson, K. Codling, *J. Phys. B: At. Mol. Opt. Phys.* **1996**, *29*, 5811; K. Codling, L. J. Frasinski, *J. Phys. B: At. Mol. Opt. Phys.* **1993**, *26*, 783.

29 E. Constant, H. Stapelfelt, P. B. Corkum, *Phys. Rev. Lett.* **1996**, *76*, 4140.

30 M. Schmidt, D. Normand, C. Cornaggia, *Phys. Rev. A* **1994**, *50*, 5037.

31 S. Shimizu, J. Kou, S. Kawato, K. Shimizu, S. Sakabe, N. Nakashima, *Chem. Phys. Lett.* **2000**, *317*, 609.

32 H. Harada, S. Shimizu, T. Yatsuhashi, S. Sakabe, Y. Izawa, N. Nakashima, *Chem. Phys. Lett.* **2001**, *342*, 563; H. Harada, M. Tanaka, M. Murakami, S. Shimizu, T. Yatsuhashi, N. Nakashima, S. Sakabe, Y. Izawa, S. Tojo, T. Majima, *J. Phys. Chem. A* **2003**, *107*, 6580.

33 R. Itakura, J. Watanabe, A. Hishikawa, K. Yamanouchi, *J. Chem. Phys.* **2001**, *114*, 5598.

34 L. Robson, K. W. D. Ledingham, A. D. Tasker, P. McKenna, T. McCanny, C. Kosmidis, D. A. Jaroszynski, D. R. Jones, R. C. Issac, S. Jamieson, *Chem. Phys. Lett.* **2002**, *360*, 382.

35 S. C. O'Brien, J. R. Heath, R. F. Curl, R. E. Smalley, *J. Chem. Phys.* **1988**, *88*, 220.

36 M. Boyle, T. Laarmann, I. Shchatsinin, C. P. Schulz, *J. Chem. Phys.* **2005**, *122*, 181103; I. V. Hertel, T. Laarmann, C. P. Schulz, *Advances in Atomic, Molecular, and Optical Physics*, ed. by B. Bederson, H. Walther, Academic Press, **2005**, Vol. 50, p. 219.

37 V. R. Bhardwaj, P. B. Corkum, D. M. Rayner, *Phys. Rev. Lett.* **2004**, *93*, 043001.

38 a) I. Kawata, H. Kono, *J. Chem. Phys.* **1999**, *111*, 9498. b) H. Kono, A. Kita, Y. Ohtsuki, Y. Fujimura, *J. Comput. Phys.* **1997**, *130*, 148.

39 K. Harumiya, H. Kono, Y. Fujimura, I. Kawata, A. D. Bandrauk, *Phys. Rev. A* **2002**, *66*, 043403.

40 H. Kono, S. Koseki, in Ref. 2, p. 267.

41 H. Kono, I. Kawata, *Advances in Multi-Photon Processes and Spectroscopy*, ed. by R. J. Gordon, Y. Fujimura, World Scientific, Singapore, **2001**, Vol. 14, p. 165.

42 H. Kono, K. Harumiya, Y. Fujimura, I. Kawata, *Photonic, Electronic, and Atomic Collisions (XXII ICPEAC)*, ed. by J. Burgdorfer, J. Cohen, S. Datz, C. R. Vane, Rinton, Princeton, **2001**, p. 197.

43 H. Kono, Y. Sato, Y. Fujimura, I. Kawata, *Laser Phys.* **2003**, *13*, 883.

44 I. Kawata, H. Kono, Y. Fujimura, A. D. Bandrauk, *Phys. Rev. A* **2000**, *62*, 031401; I. Kawata, A. D. Bandrauk, H. Kono, Y. Fujimura, *Laser Phys.* **2001**, *11*, 188.

45 A. D. Bandrauk, H. Kono, *Molecules in Intense Laser Fields: Nonlinear Multi-Photon Spectroscopy and Near-Femtosecond to Sub-Femtosecond (Attosecond) Dynamics, Advances in Multi-Photon Processes and Spectroscopy*, ed. by S. H. Lin, A. A. Villaeys, Y. Fujimura, World Scientific, Singapore, **2003**, Vol. 15, p. 147.

46 D. M. Volkov, *Z. Phys.* **1935**, *94*, 250; M. H. Mittleman, *Theory of Laser-Atom Interactions*, 2nd ed., Plenum, New York, **1993**.

47 H. Kono, S. Koseki, M. Shiota, Y. Fujimura, *J. Phys. Chem. A* **2001**, *105*, 5627.

48 Y. Sato, H. Kono, S. Koseki, Y. Fujimura, *J. Am. Chem. Soc.* **2003**, *125*, 8020.

49 R. Itakura, K. Yamanouchi, T. Tanabe, T. Okamoto, F. Kannari, *J. Chem. Phys.* **2003**, *119*, 4179.

50 S. H. Lin, Y. Fujimura, H. J. Neusser, E. W. Schlag, *Multiphoton Spectroscopy of Molecules*, Academic Press, London, **1984**.

51 W. Becker, F. Grasbon, R. Kopold, D. B. Milošević, G. G. Paulus, H. Walther, *Atomic, Molecular, and Optical Physics*, ed. by B. Bederson, H. Walther, Elsevier Science, U.S.A., **2002**, Vol. 48, p. 45.

52 P. Kruit, J. Kimman, H. G. Muller, M. J. van der Wiel, *Phys. Rev. A* **1983**, *28*, 248; L. A. Lompre, A. L'Huillier, G. Mainfray, C. Manus, *J. Opt. Soc. Am. B* **1985**, *2*, 1906.

53 R. R. Freeman, P. H. Bucksbaum, H. Milchberg, S. Darack, D. Schumacher, M. E. Geusic, *Phys. Rev. Lett.* **1987**, *59*, 1092.

54 J. H. Eberly, J. Javanainen, K. Rzążewski, *Phys. Rep.* **1991**, *204*, 331; M. Lewenstein, K. C. Kulander, K. J. Schafer, P. B. Bucksbaum, *Phys. Rev. A* **1995**, *51*, 1495.

55 N. B. Baranova, H. R. Reiss, B. Y. Zel'dovich, *Phys. Rev. A* **1993**, *48*, 1497.

56 A. M. Perelomov, V. S. Popov, M. V. Terent'ev, *Sov. Phys. JETP* **1966**, *23*, 924.

57 a) M. Lein, N. Hay, R. Velotta, J. P. Marangos, P. L. Knight, *Phys. Rev. Lett.* **2002**, *88*, 183903. b) J. Itatani, J. Levesque, D. Zeidler, H. Niikura, H. Pépin, J. C. Kieffer, P. B. Corkum, D. M. Villeneuve, *Nature* **2004**, *432*, 867. c) T. Kanai, S. Minemoto, H. Sakai, *Nature* **2005**, *435*, 470.

58 M. Dörr, D. Feldmann, R. M. Potvliege, H. Rottke, R. Shakeshaft, K. H. Welge, B. Wolff-Rottke, *J. Phys. B: At. Mol. Opt. Phys.* **1992**, *25*, L275.

59 P. Agostini, J. Kupersztych, L. A. Lompre, G. Petite, F. Yergeau, *Phys. Rev. A* **1987**, *36*, 4111.

60 E. Mevel, P. Breger, R. Trainham, G. Petite, P. Agostini, A. Migus, J. P. Chambaret, A. Antonetti, *Phys. Rev. Lett.* **1993**, *70*, 406.

61 E. W. Schlag, H. J. Neusser, *Acc. Chem. Res.* **1983**, *16*, 355.

62 H. J. Neusser, *Int. J. Mass Spectrom. Ion Processes* **1987**, *79*, 141.

63 U. Boesl, R. Weinkauf, E. W. Schlag, *Int. J. Mass Spectrom. Ion Processes* **1992**, *112*, 121.

64 W. J. Chesnavich, M. T. Bowers, *Gas Phase Ion Chemistry*, ed. by M. T. Bowers, Academic, New York, **1979**, Vol. 1, p. 119; J. Silberstein, N. Ohmichi, R. D. Levine, *J. Phys. Chem.* **1985**, *89*, 5606; J. Silberstein, R. D. Levine, *J. Am. Chem. Soc.* **1985**, *107*, 8283.

65 D. Mathur, *Phys. Rep.* **2004**, *391*, 1.

66 H. Kono, Y. Sato, N. Tanaka, T. Kato, K. Nakai, S. Koseki, Y. Fujimura, *Chem. Phys.* **2004**, *304*, 203.

67 See, for example, R. E. Moss, *Phys. Rev. A* **1998**, *58*, 4447; D. M. Bishop, B. Lam, *Mol. Phys.* **1988**, *65*, 679.

68 See, for H_2: W. Kołos, L. Wolniewicz, *J. Chem. Phys.* **1967**, *46*, 1426.

69 J. H. Posthumus, J. Plumridge, L. J. Frasinski, K. Codling,

A. J. Langley, P. F. Tady, *J. Phys. B: At. Mol. Opt. Phys.* **1998**, *31*, L985.

70 a) C. Ellert, P. B. Corkum, *Phys. Rev. A* **1999**, *59*, R3170. b) S. Banerjee, G. R. Kumar, D. Mathur, *Phys. Rev. A* **1999**, *60*, R3369.

71 M. Plummer, J. F. McCann, *J. Phys. B: At. Mol. Opt. Phys.* **1997**, *30*, L401.

72 S. Voss, A. S. Alnaser, X.-M. Tong, C. Maharjan, P. Ranitovic, B. Ulrich, B. Shan, Z. Chang, C. D. Lin, C. L. Cocke, *J. Phys. B: At. Mol. Opt. Phys.* **2004**, *37*, 4239; A. S. Alnaser, S. Voss, X.-M. Tong, C. M. Maharjan, P. Ranitovic, B. Ulrich, T. Osipov, B. Shan, Z. Chang, C. L. Cocke, *Phys. Rev. Lett.* **2004**, *93*, 113003.

73 A. Jaroń-Becker, A. Becker, F. H. M. Faisal, *Phys. Rev. A* **2004**, *69*, 023410.

74 T. Otobe, K. Yabana, J.-I. Iwata, *Phys. Rev. A* **2004**, *69*, 053404.

75 X. X. Zhou, X. M. Tong, Z. X. Zhao, C. D. Lin, *Phys. Rev. A* **2005**, *71*, 061801(R).

76 K. Mishima, K. Nagaya, M. Hayashi, S. H. Lin, *J. Chem. Phys.* **2005**, *122*, 104312.

77 J. R. Hiskes, *Phys. Rev.* **1961**, *122*, 1207.

78 W. H. Press, S. A. Teukolsky, W. T. Vetterling, B. P. Flannery, *Numerical Recipes in Fortran*, 2nd ed., Cambridge, New York, **1992**, Chap. 19; A. R. Mitchell, *Computational Methods in Partial Differential Equations*, Wiley, New York, **1969**; N. N. Yanenko, *The Method of Fractional Steps*, Springer, New York, **1971**.

79 R. S. Mulliken, *Phys. Rev.* **1939**, *7*, 20.

80 M. Thachuk, M. Y. Ivanov, D. M. Wardlaw, *J. Chem. Phys.* **1995**, *105*, 4094; *J. Chem. Phys.* **1998**, *109*, 5747.

81 Y. Kayanuma, *J. Phys. Soc. Jpn.* **1984**, *53*, 108; K. Mullen, E. Ben-Jacob, Y. Gefen, Z. Schuss, *Phys. Rev. Lett.* **1989**, *62*, 2543.

82 C. Zener, *Proc. R. Soc. London* **1932**, *696*, A137; C. Zhu, Y. Teranishi, H. Nakamura, *Adv. Chem. Phys.* **2001**, *117*, 127, and references therein.

83 A. Zavriyev, P. H. Bucksbaum, J. Squier, F. Saline, *Phys. Rev. Lett.* **1993**, *70*, 1077; T. D. G. Walsh, F. A. Ilkov, S. L. Chin, F. Chateauneuf, T. T. Nguyen-Dang, S. Chelkowski, A. D. Bandrauk, O. Atabek, *Phys. Rev. A* **1998**, *58*, 3922; M. Lein, T. Kreibich, E. K. U. Gross, V. Engel, *Phys. Rev. A* **2002**, *65*, 033403.

84 A. Saenz, *Phys. Rev. A* **2002**, *66*, 063408; X. Urbain, B. Fabre, E. M. Staicu-Casagrande, N. de Ruette, V. M. Andrianarijaona, J. Jureta, J. H. Posthumus, A. Saenz, E. Baldit, C. Cornaggia, *Phys. Rev. Lett.* **2004**, *92*, 163004; K. Mishima, K. Nagaya, M. Hayashi, S. H. Lin, *Phys. Rev. A* **2004**, *70*, 063414.

85 M. D. Feit, J. A. Fleck, Jr., A. Steiger, *J. Comput. Phys.* **1982**, *47*, 412; M. D. Feit, J. A. Fleck, Jr., *J. Chem. Phys.* **1983**, *78*, 301; M. R. Hermann, J. A. Fleck, Jr., *Phys. Rev. A* **1988**, *38*, 6000.

86 H. Kono, *Chem. Phys. Lett.* **1993**, *214*, 137.

87 Z. Mulyukov, M. Pont, R. Shakeshaft, *Phys. Rev. A* **1996**, *54*, 4299; M. Plummer, J. F. McCann, *J. Phys. B: At. Mol. Opt. Phys.* **1996**, *29*, 4625.

88 The results of ionization rates of H_2^+ at fixed internuclear distances have been presented in Refs. 27a and 27b. See also Ref. 45 and L. Y. Peng, D. Dundas, J. F. McCann, K. T. Taylor, I. D. Williams, *J. Phys. B: At. Mol. Opt. Phys.* **2003**, *36*, L295.

89 H. Niikura, P. Corkum, D. M. Villeneuve, *Phys. Rev. Lett.* **2003**, *90*, 203601; H. Niikura, D. M. Villeneuve, P. B. Corkum, *Phys. Rev. Lett.* **2004**, *92*, 133002.

90 A. Saenz, *Phys. Rev. A* **2000**, *61*, 051402; A. Saenz, *J. Phys. B: At. Mol. Opt. Phys.* **2000**, *33*, 3519.

91 W. Kołos, L. Wolniewicz, *J. Chem. Phys.* **1965**, *43*, 2429; **1966**, *45*, 509; L. Wolniewicz, *J. Chem. Phys.* **1969**, *51*, 5002; L. Wolniewicz, K. Dressler, *J. Chem. Phys.* **1985**, *82*, 3292.

92 M. J. DeWitt, E. Wells, R. R. Jones, *Phys. Rev. A* **2002**, *66*, 013409; C. Guo, M. Li, J. P. Nibarger, G. N. Gibson, *Phys. Rev. A* **1998**, *58*, R4271; A. Talebpour, S. Larochelle, S. L. Chin, *J. Phys. B: At. Mol. Opt. Phys.* **1998**, *31*, L49.

93 J. Muth-Böhm, A. Becker, F. H. M. Faisal, *Phys. Rev. Lett.* **2000**, *85*, 2280.

94 J. H. Shirley, *Phys. Rev.* **1965**, *138*, B979; S.-I. Chu, *Adv. At. Mol. Phys.* **1985**, *21*, 197; F. H. M. Faisal, *Theory of Multiphoton Processes*, Plenum Press, New York, **1987**.

95 M. Sugawara, M. Kato, Y. Fujimura, *Chem. Phys. Lett.* **1991**, *184*, 203; H. C. Day, B. Piraux, R. M. Potvliege, *Phys. Rev. A* **2000**, *61*, 031402.

96 H. G. Muller, P. H. Backsbaum, D. W. Schumacher, A. Zavriyev, *J. Phys. B: At. Mol. Opt. Phys.* **1990**, *23*, 2761.

97 K. Ruedenberg, M. W. Schmidt, M. M. Dombek, S. T. Elbert, *Chem. Phys.* **1982**, *71*, 41; **1982**, *71*, 51; **1982**, *71*, 65; M. W. Schmidt, M. S. Gordon, *Annu. Rev. Phys. Chem.* **1998**, *49*, 233.

98 Y. Kayanuma, *Phys. Rev. A* **1994**, *50*, 843.

99 R. Krishnan, J. S. Binkley, R. Seeger, J. A. Pople, *J. Chem. Phys.* **1980**, *72*, 650.

100 M. W. Schmidt, K. K. Baldridge, J. A. Boatz, S. T. Elbert, M. S. Gordon, J. H. Jensen, S. Koseki, N. Matsunaga, K. A. Nguyen, S. Su, T. L. Windus, M. Dupuis, J. A. Montgomery, Jr., *J. Comput. Chem.* **1993**, *14*, 1347.

101 A. J. Keller, *THEOCHEM* **1999**, *493*, 103.

102 M. A. Spackman, *J. Phys. Chem.* **1989**, *93*, 7594.

103 C. Cornaggia, P. Hering, *Phys. Rev. A* **2000**, *62*, 023403.

104 J. Origoso, M. Rodriguez, M. Gupta, B. Friedrich, *J. Chem. Phys.* **1999**, *110*, 3870; D. Mathur, S. Banerjee, G. Ravindra Kumar, in Ref. 2, p. 336.

105 K. F. Freed, J. R. Lombardi, *J. Chem. Phys.* **1966**, *45*, 591.

106 H. Kono, S. H. Lin, *J. Chem. Phys.* **1986**, *84*, 1071; A. D. Bandrauk, H. Shen, *J. Chem. Phys.* **1993**, *99*, 1185.

107 N. Balakrishnan, C. Kalyanaraman, N. Sathyamurthy, *Phys. Rep.* **1997**, *280*, 79.

108 T. J. Park, J. C. Light, *J. Chem. Phys.* **1986**, *85*, 5870; C. Leforestier, R. Bisseling, C. Cerjan, M. Feit, R. Friesner, A. Guldberg, A. D. Hammerich, G. Julicard, W. Karrlein, H. D. Meyer, N. Lipkin, O. Roncero, R. Kosloff, *J. Comput. Phys.* **1991**, *94*, 59.

109 L. J. Frasinski, K. Codling, P. A. Hatherly, *Science* **1989**, *246*, 1029; D. A. Card, E. S. Wisniewski, D. E. Folmer, A. W. Castleman, Jr., *Int. J. Mass Spectrom.* **2003**, *223–224*, 355.

110 C. Cornaggia, *Phys. Rev. A* **1993**, *54*, R2555.

111 A. Iwamae, K. Hishikawa, K. Yamanouchi, *J. Phys. B: At. Mol. Opt. Phys.* **2000**, *33*, 223.

112 H. Hasegawa, K. Hishikawa, K. Yamanouchi, *Chem. Phys. Lett.* **2001**, *349*, 57; A. Hishikawa, H. Hasegawa, K. Yamanouchi, *Chem. Phys. Lett.* **2002**, *361*, 245.

113 A. Hishikawa, K. Yamanouchi, private communication.

114 E. Charron, A. Giusti-Suzor, F. H. Mies, *Phys. Rev. A* **1994**, *49*, R641; T. Kanai, H. Sakai, *J. Chem. Phys.* **2001**, *115*, 5492; N. B. Baranova, H. R. Reiss, B. Y. Zel'dovich, *Phys. Rev. A* **1993**, *48*, 1497; A. Sheehy, B. Walker, L. F. Di Mauro, *Phys. Rev. Lett.* **1995**, *74*, 4799; A. D. Bandrauk, J. Levesque,

S. Chelkowski, in Ref. 2, p. 221.
115 S. M. Hankin, D. M. Villeneuve, P. B. Corkum, D. M. Rayner, *Phys. Rev. Lett.* **2000**, *84*, 5082.
116 V. R. Bhardwaj, P. B. Corkum, D. M. Rayner, *Phys. Rev. Lett.* **2003**, *91*, 203004.
117 W. Becker, F. Grasbon, R. Kopold, D. B. Milošević, G. G. Paulus, H. Walther, *Adv. At., Mol., Opt. Phys.* **2002**, *48*, 35.
118 F. H. M. Faisal, *J. Phys. B: At. Mol. Phys.* **1973**, *6*, L89; A. Becker, F. H. M. Faisal, *J. Phys. B: At. Mol. Opt. Phys.* **2005**, *38*, R1; A. Becker, F. H. M. Faisal, *Phys. Rev. Lett.* **2000**, *84*, 3546.
119 H. R. Reiss, *Phys. Rev. A* **1980**, *22*, 1786; *Prog. Quantum Electron.* **1992**, *16*, 1.
120 M. Kanno, T. Kato, H. Kono, Y. Fujimura, F. H. M. Faisal, *Phys. Rev. A* **2005**, *72*, 033418.
121 T. Kato, H. Kono, *Chem. Phys. Lett.* **2004**, *392*, 533.
122 Y. Ohtsuki, M. Sugawara, H. Kono, Y. Fujimura, *Bull. Chem. Soc. Jpn.* **2001**, *74*, 1167.

Award recipient

Hirohiko Kono was born in Osaka in 1953. He was graduated from Tohoku University in 1976 with a B.S. degree in chemistry. He received his Ph.D. degree in chemistry from Tohoku University in 1981. Then, he joined the research group directed by Professor S. H. Lin at Arizona State University as a postdoctoral fellow. In 1985, he became Research Associate at the Faculty of Engineering, Yamagata University. In 1991, he became Associate Professor of the College of General Education of Tohoku University. Since 1993, he has been Associate Professor of the Department of Chemistry, Tohoku University. He was an Adjunction Associate Professor at the National Institute for Fusion Science from 2003 to 2004. His current research fields are theoretical studies of the dynamics of molecules and biological systems in laser fields.

Katsunori Nakai was born in Gunma in 1977. He received his B.S. degree from Tohoku University in 2000. In 2005, he received his Ph.D. degree from the same university under the direction of Professors Hirohiko Kono and Yuichi Fujimura. His research interests are studies on the electronic structure of nano-sized compounds in the presence of an electric field.

Tsuyoshi Kato was born in 1967 in Chiba, Japan. He received his doctor degree (1996) from Tohoku University under the supervision of Prof. Yuichi Fujimura. Then, he joined the group of Prof. S. H. Lin at the Institute of Atomic and Molecular Sciences (Taipei) as a postdoctoral researcher. For the three years following October of 1996, he was a domestic research fellow of JST at the group of Dr. S. Kobayashi at the Institute of Advanced Industrial Science and Technology. Afterwards, he joined the group of Prof. H. Nakanishi at the Institute of Multidisciplinary Research for Advanced Materials as a research associate (1999). He was a research fellow in the group of Prof. Y. Tanimura at the Institute for Molecular Science (2000–2002). Since October of 2002, he has been a research fellow of Tohoku University working with Prof. Hirohiko Kono. His current research interests focus on the establishment of a time-dependent multi-configuration description of many-electron systems to investigate the electronic dynamics in an intense laser field.